Title
Development of Dinuclear Metal Complexes for Catalytic Transformations in Artificial Photosynthesis

Author
Davenport, Timothy Charles

Publication Date
2012

Peer reviewed|Thesis/dissertation

Development of Dinuclear Metal Complexes for Catalytic Transformations in Artificial Photosynthesis

by

Timothy Charles Davenport

A dissertation submitted in partial satisfaction of the
requirements for the degree of
Doctor of Philosophy

in

Chemistry

in the

Graduate Division

of the

University of California, Berkeley

Committee in charge:
Professor T. Don Tilley, Chair
Professor Christopher J. Chang
Professor Alexis T. Bell

Fall 2012

Abstract

Development of Dinuclear Metal Complexes for Catalytic Transformations in Artificial Photosynthesis

by
Timothy Charles Davenport
Doctor of Philosophy in Chemistry
University of California, Berkeley
Professor T. Don Tilley, Chair

The storage of solar energy in chemical bonds has attracted much interest as a "clean" alternative to petroleum-based fuels. In such systems, a current major challenge is the development of high efficiency catalysts for the oxidation of water to dioxygen and the reduction of carbon dioxide to carbon-based fuels. This dissertation examines novel dinucleating ligands for the formation of dinuclear first-row transition metal complexes and studies their potential for catalytic applications.

In Chapter 1, a dinuclear cobalt molecular structural analog of a proposed Co-Pi active site was synthesized from the novel dinucleating ligand 2,7-bis(fluoro-di(2-pyridyl)methyl)-1,8-naphthyridine (DPFN) as $[Co_2(\mu\text{-}OH)_2(OH_2)_2(DPFN)][NO_3]_4$. The structure features a bis(μ-OH) dinuclear cobalt "diamond-shaped" core with a terminal aqua ligand on each cobalt center in a *syn* configuration analogous to a dinuclear unit of a cobalt oxide surface site. The compound was found to be ineffective for electrocatalytic water oxidation activity. The low catalytic activity of the complex may result from the substitution of terminal aqua ligands for phosphate in KP_i electrochemical solutions. Reaction of the complex with potassium phosphate forms the κ^2,κ^2-phosphate-bridged tetranuclear cobalt complex $[\{Co_2(\mu\text{-}OH)_2(DPFN)\}_2(\kappa^2,\kappa^2\text{-}PO_4)][NO_3]_5$. It is suspected that formation of similar phosphate complexes under electrochemical conditions is responsible for the low catalytic activity of $[Co_2(\mu\text{-}OH)_2(OH_2)_2(DPFN)][NO_3]_4$.

A series of dinuclear and tetranuclear first-row transition metal complexes, $[Co_2(\mu\text{-}Cl)_2Cl(CH_3OH)(DPFN)]_2[CoCl_4]\cdot 8H_2O$, $[Ni_2(\mu\text{-}Cl)_2Cl(CH_3OH)(DPFN)][Cl]\cdot 4H_2O$, $[Cu_4(\mu\text{-}Cl)_6(DPFN)_2][Cl]_2\cdot 6H_2O$, and $[Cu_2(\mu\text{-}OH)_2(NO_3)(OH_2)(DPFN)]\cdot 2H_2O$, were synthesized with DPFN and compared to $[Co_2(DPFN)(\mu\text{-}OH)_2(OH_2)_2][NO_3]_4$ in Chapter 2. The dinuclear and tetranuclear complexes possess pseudo-octahedral geometries about the metal centers and contain chloro, hydroxo, and aqua bridging ligands forming a "diamond" shape. The metal-metal distance between the two metal centers varies from 2.7826(5) to 3.2410(11) Å. High-spin metal centers are formed with 2+ oxidation state metal centers, in contrast to the low-spin diamagnetic Co(III) complex. The complexes are characterized by electronic spectroscopy, electrochemical and potentiometric titration methods.

In Chapter 3, the ligand 2,7-bis(di(2-pyridyl)ethyl)-1,8-naphthyridine (DPEN) promotes the formation of a rare $\mu\text{-}\eta^1\text{:}\eta^1$ acetonitrile-bridged dicopper(I) complex, $[(DPEN)Cu_2(\mu\text{-}NCMe)][PF_6]_2$. The acetonitrile has unusually short Cu–N bond distances for an acetonitrile-bridged complex of 2.004(3) and 1.979(3) Å. Infrared spectroscopy and computational studies indicate that the acetonitrile is involved in a primarily 3-center 2-electron bond that is stabilized by a cuprophilic interaction. The labile acetonitrile of the acetonitrile complex can be substituted with xylyl isocyanide and carbon monoxide. These complexes may lead to the development of catalysts for the reduction of carbon dioxide to fuels.

Chapter 4 investigates the interactions of molecular water oxidation complexes with inorganic frameworks for eventual use in photoactive materials. The "ruthenium blue dimer" was incorporated into the mesoporous silica material SBA15. Base treatment of SBA15 was found to greatly increase loading of the complex onto the surface. The identity of the adsorbed species was determined to be the ruthenium dimer cation electrostatically adsorbed onto the surface using diffuse reflectance UV-Vis spectroscopy, diffuse reflectance infrared spectroscopy, Raman scattering. The activity of the adsorbed dimer towards water oxidation was explored using aqueous $(NH_4)_2Ce(NO_3)_6$ as a sacrificial oxidant.

For Steven

Table of Contents

List of Figures

Chapter 1

Chapter 2

Chapter 3

Chapter 4

List of Schemes

List of Tables

Acknowledgements

It is hard to believe that my time in graduate school is finally coming to an end. This has been a very large part of my life, and there are many people to thank for helping me get to this point. First, I would like to thank my family, who have been with me through my entire journey. To my parents, who have always believed in me and supported me in every decision. Also, to my brothers Chris and Jon, for both being wonderful older siblings. To my grandparents, both living and departed, for the unconditional love, support, and faith in everything. And to all my aunts, uncles, and cousins, who have filled my life with laughter. To my other family, Keith, Valerie and Madison, who have filled Christmas time with joy. Finally, to my wife Amanda, who has shared this graduate school experience and provided essential support in the final push to completion.

This dissertation would not be possible without the guidance of my advisor T. Don Tilley. Don has provided a wonderful environment for me to explore my interests and has taught me to be an independent researcher. Also, I would like to thank Rosemary Tilley, without whom the laboratory would cease to function. For all my questions about graduate school I give a special thank you to Lynn Keithlin.

Many students and postdocs have shared my time at Berkeley. I would like to thank Dan Ruddy and Evan Rumberger who helped me get started in graduate school. I would like to thank all my colleagues in the Tilley lab, who have provided helpful discussions and made the time pass more quickly, particularly Paul Cordeiro and John Curley. Special thanks go to Kevin Ahn, who, more than anyone, understands my experiences at Berkeley. For essential help with experiments, thanks go to Will Vining, Shannon Klaus, Meredith McMurdo, and Gary Chang.

Finally, thanks go to the people at MIT who encouraged me to pursue graduate school. Special thanks go to my undergraduate advisor Bob Griffin, who provided me much helpful advice and great opportunities in the laboratory. Also, I would like thank the people who shared my time in the Bitter lab who prepared me for graduate school, particularly Marvin Bayro and Patrick van der Wel, who provided guidance in my undergraduate projects.

Timothy Charles Davenport

Chapter 1

A Molecular Structural Analog of a Proposed Dinuclear Active Site in Cobalt-Based Water Oxidation Catalysts

Introduction

Increased global concern over future sources of renewable energy has resulted in considerable research on the development of artificial photosynthesis, and its necessary reliance on the challenging half-reaction for water oxidation.[1] To date, research efforts on water oxidation catalysis have generally yielded catalysts that are either inefficient, or based on very expensive components such as Ir or Ru.[2–8] Promising exceptions to this trend are solid-state catalysts based on cobalt, including Co_3O_4 nanoparticles[9] and the amorphous cobalt phosphate system (Co-Pi) which operates under neutral pH conditions.[10] These catalysts are associated with moderately high overpotentials (ca. 0.4 V at 10 mA/cm^2 current density), but the promise of cost-effective catalysts based on cobalt has stimulated considerable research activity in this area.[11] One major research theme seeks to identify the mechanism by which these cobalt catalysts operate, to enable the design of more efficient catalysts. As a model of the Co-Pi system, computational studies on a Co_3O_4 cubane structure indicate that the mechanism may proceed through the coupling of two adjacent Co^{IV}=O moieties to form a peroxo-bridged intermediate in the rate determining step,[12] which is consistent with experimental evidence.[13] However, as is often the case for heterogeneous catalysts, the identification of a detailed mechanism has proven quite challenging.

Further mechanistic insights should result from the synthesis and study of well-defined molecular models for candidate active sites. For this purpose, the proposed dinuclear site shown in Figure 1a was targeted for modeling since it represents the minimal unit active in bond-breaking and bond-making events in recent proposed mechanisms.[13] This dinuclear site contains a pair of essential structural features. First, the dinuclear center contains two adjacent terminal hydroxo ligands. On oxidation, these ligands should be deprotonated to give adjacent terminal oxo ligands which would then couple in the O–O bond forming step. Second, the cobalt centers are bridged by two oxo/hydroxo ligands in a diamond core structure. This bridging structure positions the terminal ligands at a distance appropriate for O–O coupling. In addition, oxo or hydroxo bridging ligands provide strong electronic communication between the cobalt centers, facilitating multi-electron chemistry. To this end, dinucleating ligands based on the 1,8-naphthyridine core were designed to accommodate two octahedral metal centers at a distance optimized for bridging by two oxygen atoms and coordination of two terminal aquo ligands. In this contribution, we describe the synthesis and characterization of this type of dicobalt complex, $[Co_2(\mu\text{-}OH)_2(OH_2)_2(DPFN)][NO_3]_4$ (**1**, Figure 1a).

Within the context of molecular models for cobalt-based molecular water oxidation catalysts, it is notable that few molecular cobalt catalysts have been reported,[14,15] possibly due to the limited stability of such catalysts under the necessarily high oxidizing conditions.[16] Significantly, a mono-cobalt complex related to **1**, $[Co(Py5)(OH_2)][ClO_4]_2$ (Py5 = 2,6-(bis(bis-2-pyridyl)-methoxymethane)pyridine) (Co(Py5)), has been reported to be an electrocatalyst for water oxidation under basic conditions. Intriguingly, the electrochemical evidence suggested that Co(Py5) does not degrade under these conditions, though formation of a small amount of catalytically active Co_3O_4 *in situ* could not be ruled out. Recently, a dinuclear cobalt complex based on the bispyridylpyrazolate ligand was reported to catalyze water oxidation under low pH conditions (pH = 2.1) at 2.0 V *vs.* NHE.[17]

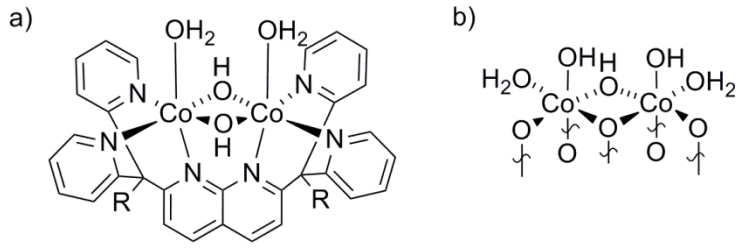

Figure 1. a) Expected binding of Co into a naphthyridine-based ligand. b) Proposed minimal catalytic active site for Co-Pi.

Results and Discussion

The dinucleating ligand used in this work, 2,7-bis(fluoro-di(2-pyridyl)methyl)-1,8-naphthyridine (DPFN), was prepared starting from 2,7-dichloro-1,8-naphthyridine (eq. 1).

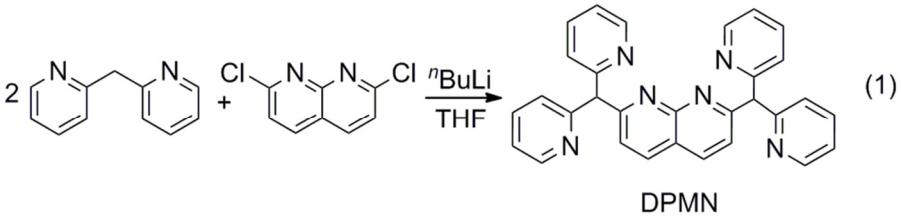

Reaction with lithiated 2,2'-dipyridylmethane afforded the compound 2,7-bis(di(2-pyridyl)methyl)-1,8-naphthyridine (DPMN, 22% yield). The solid-state structure of DPMN is shown in Figure 2. It was found that although DPMN could be used as a dinucleating ligand, the methine C-H bond in DPMN was oxidatively unstable under certain conditions. For this reason, DPMN was converted to DPFN by reaction with two equivalents of SelectFluor (eq. 2, 39% yield).

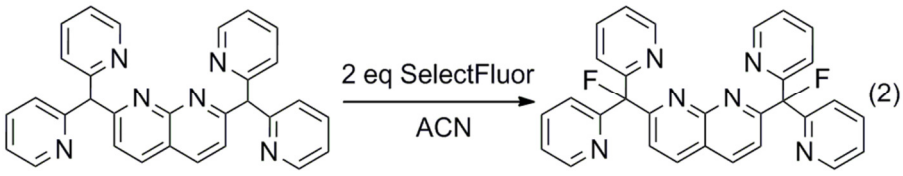

The solid-state structure of DPFN is shown in Figure 3. Reaction of DPFN with two equivalents of $Co(NO_3)_2{\cdot}6H_2O$ in ethanol, quickly followed by addition of excess hydrogen peroxide, resulted in a red precipitate which is dissolved in water and crystallized to afford red crystals of $[Co_2(\mu\text{-}OH)_2(OH_2)_2(DPFN)][NO_3]_4$ (**1**) (eq. 3).

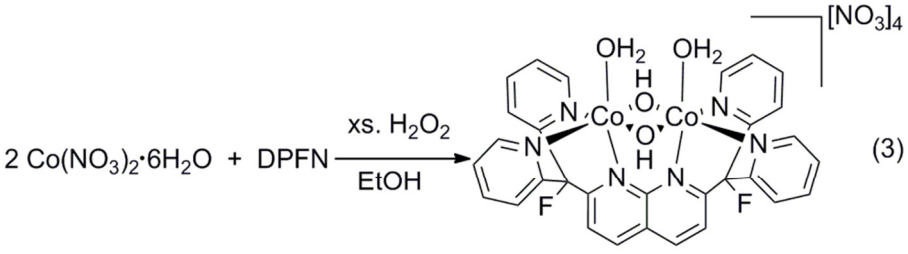

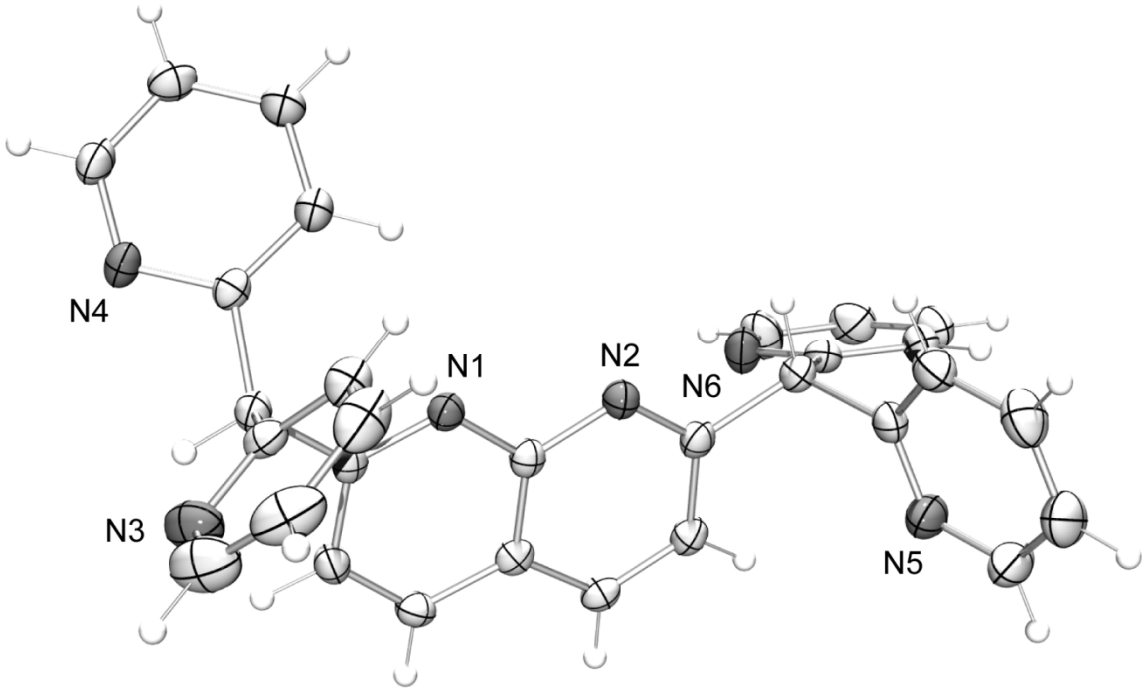

Figure 2. Crystal structure of DPMN.

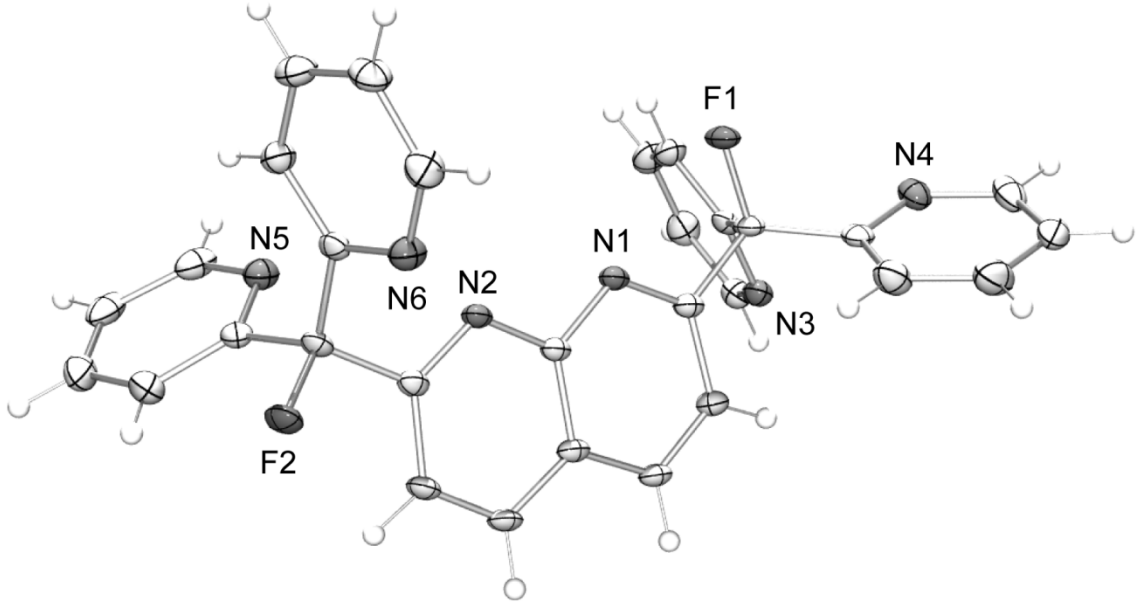

Figure 3. Crystal structure of DPFN.

The solid-state structure of **1** is shown in Figure 4. Each metal center is bound to three nitrogen donors of DPFN in a *facial* manner. Each cobalt centers features an octahedral coordination geometry, and the two octahedrons share an edge *via* bridging of the hydroxide ligands. The coordination spheres of about each cobalt center are completed by a terminal aquo ligand. Metric comparisons of the dinuclear core of **1** with that measured by EXAFS for dinuclear units in the Co-Pi system, give a. Co-(μ-OH) bond length is 1.89(1) Å, which is very close to the Co-O distance of 1.89 Å in Co-Pi. This results in a Co-Co distance of 2.78 Å, very close to the 2.82 Å separation observed in the Co-Pi system.

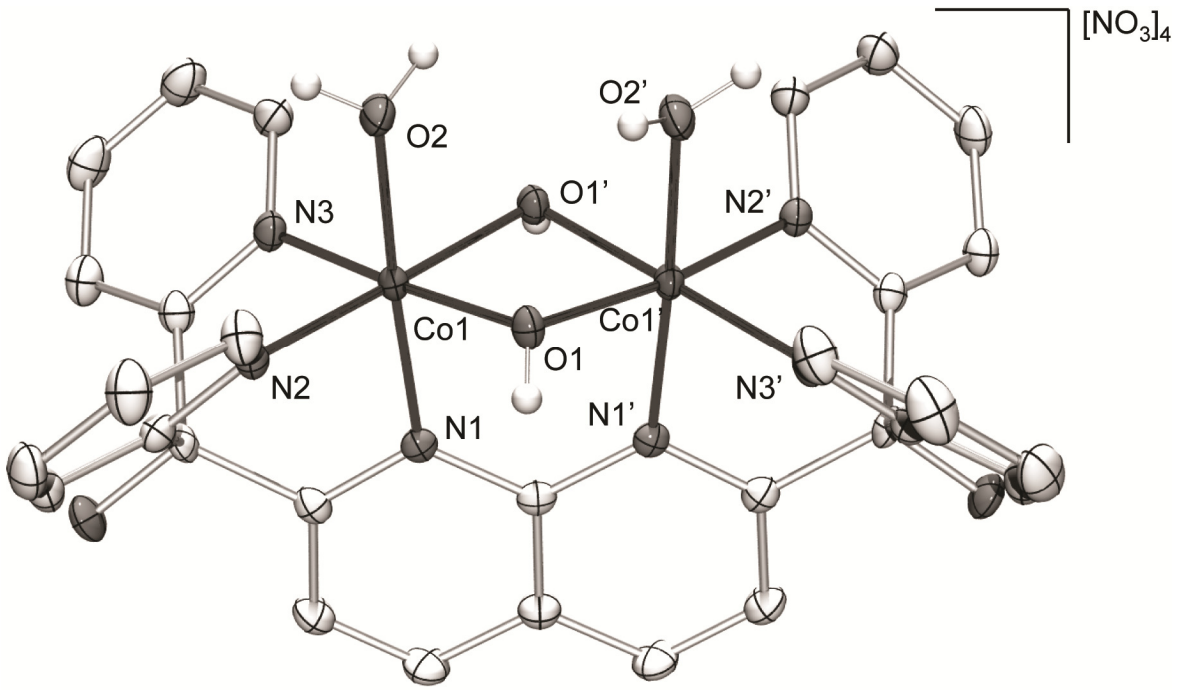

Figure 4. Crystal structure of **1**. DPFN hydrogen atoms and the NO_3^- counterions have been omitted for clarity. Selected bond lengths [Å] and angles [°]: Co1–Co1' 2.7826(5), Co1–O1 1.879(2), Co1–O2 1.908(2), Co1–N1 1.941(2), Co1–N2 1.918(2), Co1–N3 1.9306(2), Co1–O1–Co1' 95.85(7).

The electrochemistry of complex **1** was studied in the context of its facility for water oxidation electrocatalysis. Cyclic voltammetry of **1** in phosphate-buffered solution revealed irreversible both oxidation and reduction events (Figure 5). A Pourbaix diagram was constructed over the pH range 1 – 12 in phosphate-buffered solution using differential pulse voltammetry (DPV) to measure the potentials for redox events (Figure 6). At pH 1.3, **1** exhibits a single irreversible reduction process (**A**) at 0.54 V *vs.* NHE. This reduction process exhibits a pH dependence of −27 mV/dec to pH 2.4. At pH 2.4, the reduction becomes pH independent up to pH 4.7, and then the reduction exhibits a pH dependence of −38 mV/dec to pH 6.7. Above pH 6.7 the reduction exhibits a pH dependence of −63 mV/dec to pH 9.6, after which it is no longer observed.

Below pH 3.8, only the reduction process **A** is observed, however, above pH 3.8 a new irreversible reduction process (**B**) is observed that increases in current as the first process

decreases until it is no longer observed above pH 9.6. This observation indicates that the two reduction processes represent independent species (Figure 7). The reduction process **B** is observed at 0.27 V *vs.* NHE at pH 3.8. **B** exhibits a pH dependence of −29 mV/dec up to pH 4.4, after which the process is pH independent to pH 7.2. At pH 7.2, the process exhibits a pH dependence of −30 mV/dec through pH 12. Analysis of **1** in 0.1 M $NaBF_4$ electrolyte solution in the pH range 3 – 7 indicates that process **A** is present in both $NaBF_4$ solutions and phosphate solutions, while process **B** exists only in phosphate solution. On the basis of this observation, process **A** is attributed to **1**, while process **B** is attributed to a **1**-PO_4 complex of unknown composition.

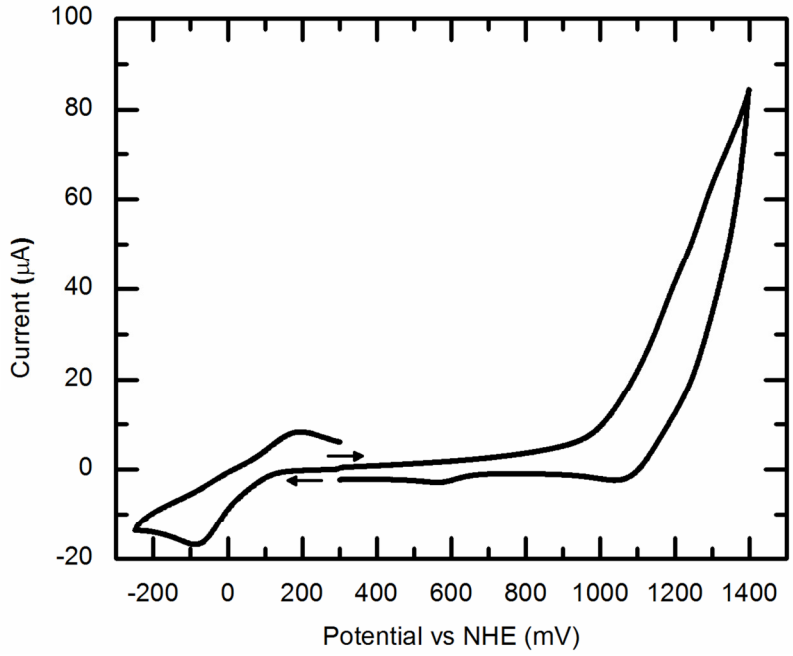

Figure 5. Cyclic voltammogram of 2 mM **1** at pH 9.0 in 0.1 M KP_i aqueous buffer solution. Scanning rate is 100 mV/s and potentials are reported relative to the normal hydrogen electrode.

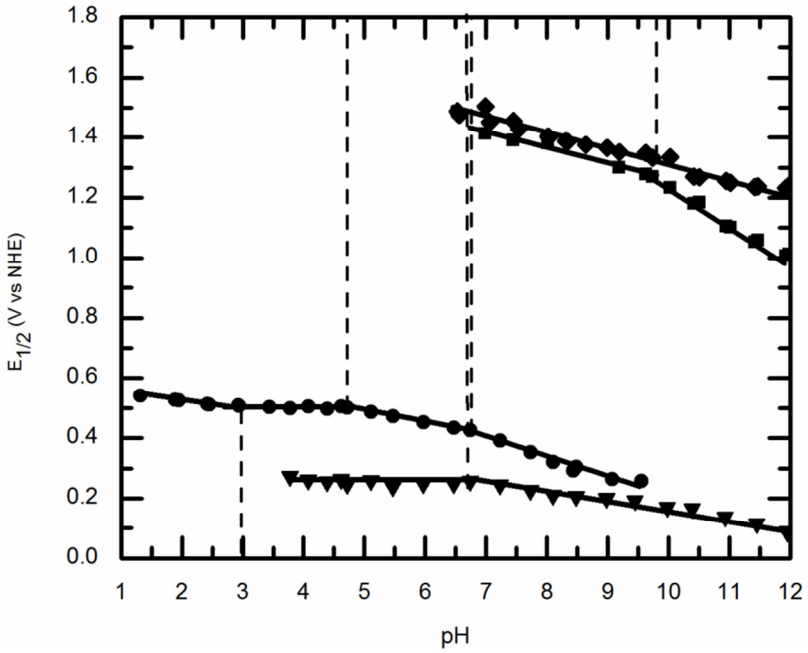

Figure 6. Pourbaix diagram of **1** in phosphate buffer solution from pH 1–12 in the potential window 0–1.8 V *vs.* NHE. Potentials of electrochemical events are determined by differential pulse voltammetry.

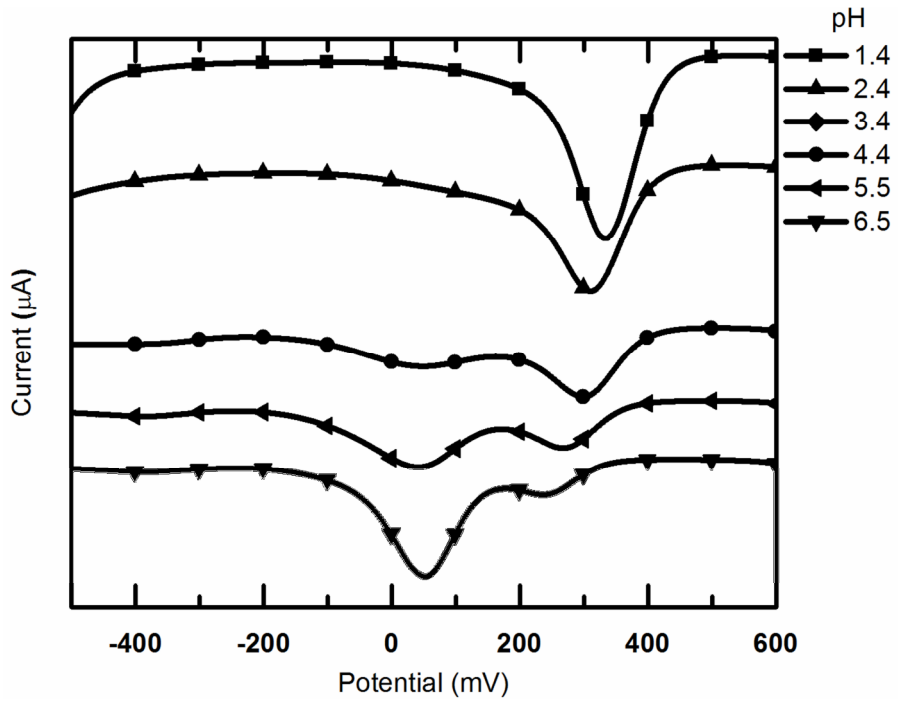

Figure 7. Cathodic differential pulse voltammograms of **1** with variation of pH from 1.4–6.5.

With the above information, the reduction processes can be assigned to the following species (Scheme 1). Below pH 2.4, process **A** is assigned to a 2-e^-, 1-H^+ reduction event consistent with the −27 mV/dec pH dependence, involving the reduction of **1** to $\mathbf{1}^{2-}$+$\mathbf{H}^+$ where the two Co^{III} centers of **1** are reduced to Co^{II}. From pH 2.4 – 4.7 this process becomes pH independent and is assigned to the reduction of **1** to $\mathbf{1}^{2-}$. From pH 4.7 – 6.7, the pH dependence of −38 mV/dec is attributed to a 2-e^-, 1-H^+ process involving the reduction of **1-H**$^+$ to $\mathbf{1}^{2-}$. Above pH 6.7 further deprotonation of **1** to the **1-2H**$^+$ species results in a 2-e^-, 2-H^+ reduction process involving the reduction of **1-2H**$^+$ to $\mathbf{1}^{2-}$ consistent with the −63 mV/dec pH dependence. The presence of the species resulting from deprotonation of **1**, invoked above, was confirmed by a potentiometric titration of **1**. This titration revealed two acid dissociation constants of pK_{a1} = 4.1(1) and pK_{a2} = 5.8(1). For process B, the reductions are also assigned to two $Co^{III} \rightarrow Co^{II}$ events associated with a **1-PO$_4$** species of unknown composition and are thus not represented in Scheme 1. Thus, from pH 3.8 to 4.4, the pH dependence of −29 mV/dec indicates a 2-e^-, 1-H^+ reduction process that takes **1-PO$_4$** to $\mathbf{(1\text{-}PO_4)}^{2-}$+$\mathbf{H}^+$. From pH 4.4 to 7.2, the pH-independent reduction process indicates a 2-e^- event for **1-PO$_4$**, which is converted to $\mathbf{(1\text{-}PO_4)}^{2-}$. Above pH 7.2, the 2-$e^-$, 1-$H^+$ reduction event reduces the **(1-PO$_4$)-H**$^+$ species to $\mathbf{(1\text{-}PO_4)}^{2-}$, consistent with the −30 mV/dec pH dependence.

Scheme 1. Electrochemically coupled species of **1** observed in phosphate buffer.

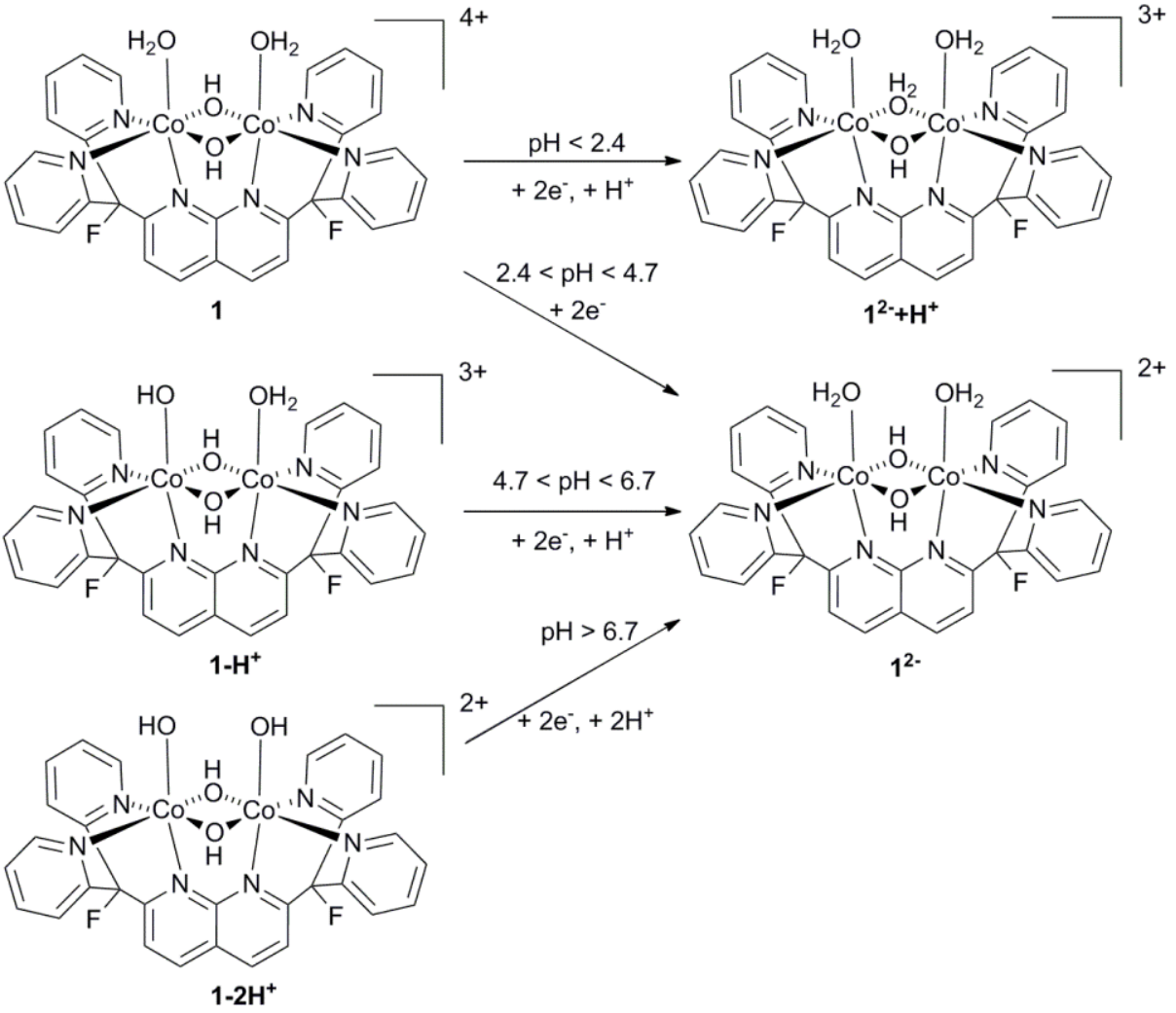

In the anodic direction, no oxidative event is observed below pH 6.5. Above pH 6.5, two overlapping irreversible oxidations are observed at 1.49 V *vs.* NHE (pH 6.5, **C**), and at 1.41 V *vs.* NHE at (pH 7.0, **D**). Process **C** exhibits a pH dependence of −50 mV/dec which is attributed to a 1-e^-, 1-H^+ event which can occur up to pH 12. Up to pH 9.7, process **D** exhibits a pH dependence of −53 mV/dec also attributed to a 1-e^-, 1-H^+ transfer and above pH 9.7 **D** exhibits a pH dependence of −120 mV/dec through pH 12. These processes are assigned to oxidation of one Co^{III} center to Co^{IV}; however, the nature of the species in solution corresponding to processes **C** and **D** are unknown. The relative charge passed by process **C** versus process **D** changes from run to run, indicating that these processes represent independent species in solution. In addition, in 0.1 M $NaBF_4$ electrolyte solution no oxidation processes are observed below pH 10.0, indicating that the processes represent phosphate-bound species.

Complex **1** was evaluated as an electrocatalyst for water oxidation by controlled potential electrolysis (CPE) at pH 9.0 (Figure 8). The catalytic current of 27 μA/cm^2 observed at an overpotential of 0.9 V (1.6 V *vs.* NHE) represents a negligible amount of water oxidation.

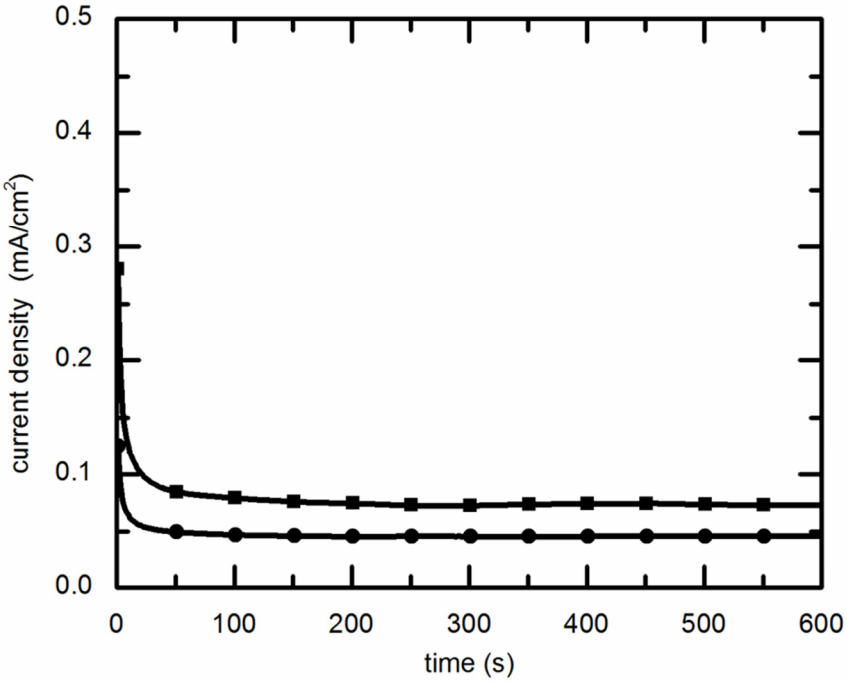

Figure 8. Controlled potential electrolysis of **1** at 1.6 V in phosphate buffer solution at pH 9.0. The electrode was pretreated by holding at 1.6 V for 10 min in phosphate buffer solution at pH 9.0.

Due to the apparent reactivity of **1** with phosphates, an attempt was made to synthesize and characterize phosphate deriviatives of **1**. Reaction of **1** with one equivalent of K_3PO_4 resulted in formation of the phosphate-bridged tetranuclear cobalt complex **2** (Eq. 4). Crystals of sufficient quality for X-ray crystal structure determination were formed by vapor diffusion of acetonitrile into an aqueous solution of **2** (Figure 9). The phosphate-bridged complex **2** represents one possible species formed in phosphate-buffered solutions for electrochemistry. Because the terminal aqua ligands are expected to participate in the mechanism for oxygen evolution,[13] substitution of the aqua ligands for phosphate may inhibit oxygen evolution.

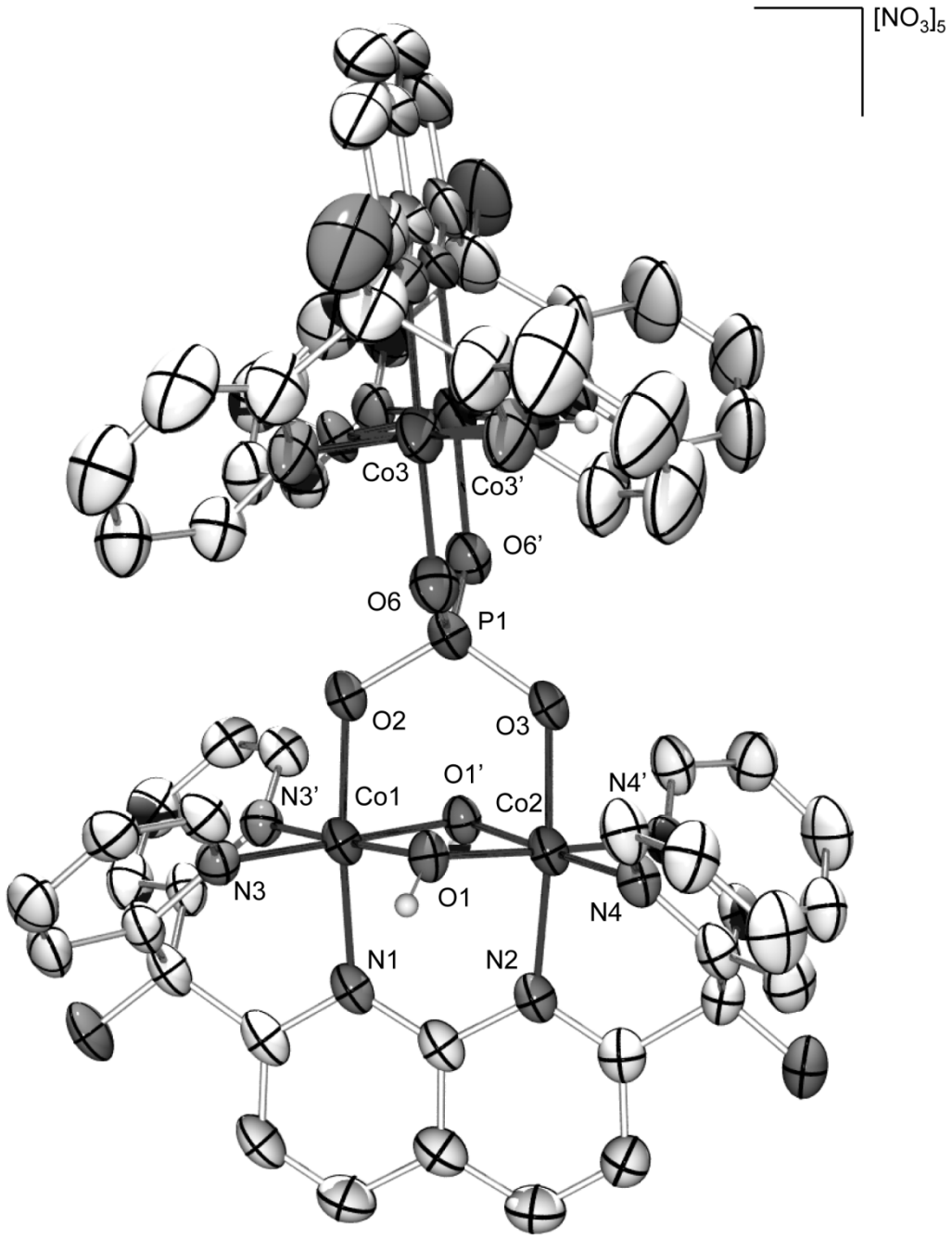

Figure 9. Crystal structure of **2**. DPFN hydrogen atoms and the NO_3^- counterions have been omitted for clarity. Selected bond lengths [Å] and angles [°]: Co1–Co2 2.692(1), Co3–Co3' 2.679(2), Co1–O1 1.867(3), Co2–O1 1.861(3), Co1–N1 1.940(5), Co2–N2 1.939(5), Co1–N3 1.914(3), Co2–N4 1.913(3), Co1–O2 1.904(4), Co2–O3 1.888(4), Co3–O6 1.892(3), Co1–O1–Co2 92.5(1).

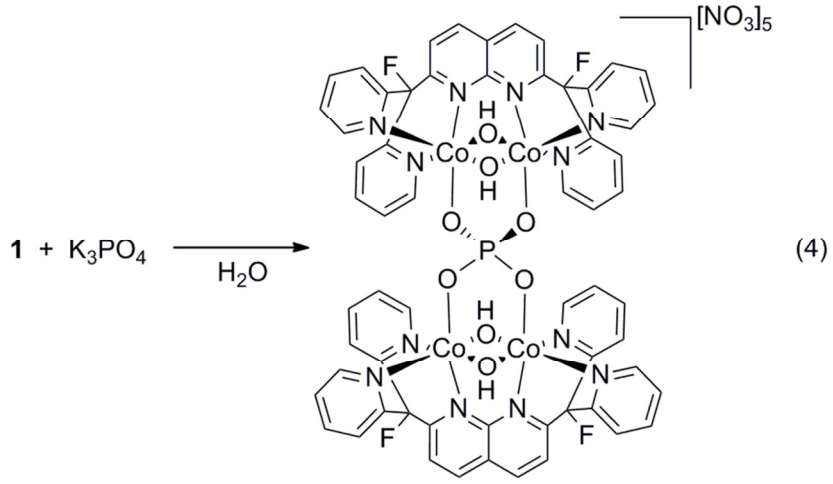

Although complex **1** is not effective as a molecular water oxidation catalyst, further analysis of the complex may inform future attempts to design molecular cobalt catalysts for water oxidation. To this end, the various protonation and oxidation states were analyzed computationally to obtain insights into the observed electrochemistry. The HOMO molecular orbitals of **1** and its deprotonated states are shown in Figure 10. For **1**, the HOMO is a diffuse orbital located on the pyridine rings of the DPFN ligand. Because of this, oxidation of **1** does not result in removal of an electron from the cobalt centers, explaining why no oxidation events are observed for this species by electrochemistry. On the other hand, deprotonation of **1** to give **1-H$^+$** or **1-2H$^+$** results in a HOMO localized on the oxygen atoms, and corresponding to the lone pairs of the terminal hydroxo ligands. Proton-coupled electron transfers involving **1-H$^+$** or **1-2H$^+$** to **1$^+$-2H$^+$** or **1$^+$-3H$^+$**, respectively, thus results in the removal of an electron from an orbital of this type as shown in Figure 11 to give a species formally containing a Co^{IV}=O moiety where significant radical character is present on the oxygen atom. It is apparent from the electrochemical experiments that although a species of this type might form, decomposition of the complex in solution occurs competitively. A further proton-coupled electron transfer involving **1$^+$-2H$^+$** or one electron oxidation of **1$^+$-3H$^+$** results in the formation of an O–O bond (**1^{2+}-3H$^+$,** Figure 12), in a similar fashion to that calculated for Co-Pi.[13] This analysis indicates that future dinuclear cobalt complexes must promote the oxidation of **1$^+$-2H$^+$** or **1$^+$-3H$^+$** over decomposition to be effective water oxidation catalysts.

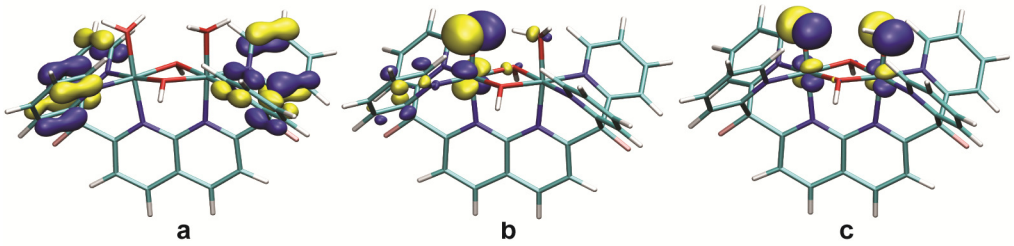

Figure 10. HOMO of a) **1**, b) **1-H$^+$**, and c) **1-H$^+$**.

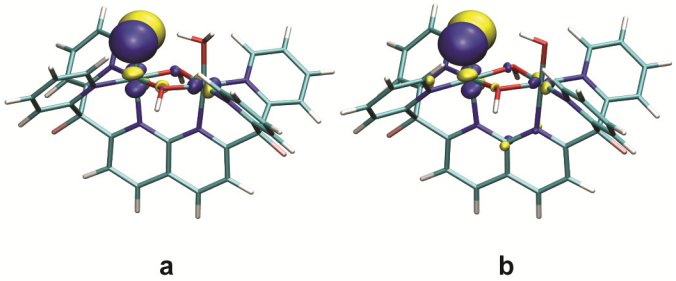

Figure 11. Unoccupied β e^- orbitals. a) SOMO of $\mathbf{1^+}$**-2H**$^+$, b) SOMO+1 of $\mathbf{1^+}$**-3H**$^+$.

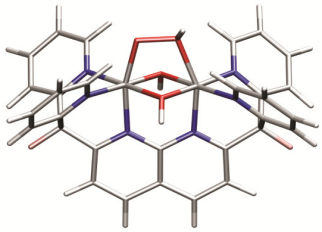

Figure 12. O–O bond formation in $\mathbf{1^{2+}}$**-3H**$^+$.

Conclusion

In light of the computational results, it is possible to speculate about the requirements for an effective dinuclear cobalt molecular water oxidation catalyst. First, deprotonation of cobalt-aquo species is necessary to access oxidizable molecular orbitals relevant to water oxidation. Second, less positive potentials for oxidation are necessary to match oxidation potentials to the thermodynamic potential for water oxidation. This could be accomplished by increasing the Lewis acidity of the cobalt centers by using harder, more electronegative donors in the dinucleating ligand. Future efforts towards the development of molecular Co-Pi analogues will be focused in this direction.

We have developed a structural analog of the minimal dinuclear unit for cobalt-based water oxidation catalysts. While electrochemical results show that the reported complex is not an effective water oxidation catalyst, these studies provide important information regarding the inherent characteristics of such systems.

Experimental

General Considerations. Solvents were purchased from Aldrich at spectroscopic grade. For synthesis purposes, distilled, deionized water was used. Deuterated solvents were purchased from Cambridge Isotope Laboratories and used as received. *n*-Butyllithium, $Co(NO_3)\cdot 6(H_2O)$, and 1-Chloromethyl-4-fluoro-1,4-diazoniabicyclo[2.2.2]octane bis(tetrafluoroborate) (SelectFluor) were purchased from Aldrich and used as received. The reagents 1,1-di-(2-pyridyl)methane and 2,7-dichloro-1,8-naphthyridine were prepared according to literature procedures.[18] NMR spectra were recorded on Bruker AV-600, AVQ-400 and AV-300 spectrometers at room temperature. ^{1}H NMR spectra were referenced to residual protio solvent peaks (δ 7.24 for *d*-chloroform, δ 5.32 for d_2-dichloromethane, δ 4.80 for d_2-water). $^{13}C\{^1H\}$

NMR spectra were referenced to solvent resonances (δ 77.23 for *d*-chloroform, δ 54.00 for d_2-dichloromethane). Elemental analyses were carried out by the College of Chemistry Microanalytical Laboratory at the University of California, Berkeley. UV-Vis spectra were recorded on a Varian-Cary 300 Bio spectrophotometer at 1 nm resolution. Potentiometric titrations were performed using a Thermo Fisher Orion 3-Star pH meter with a Ag/AgCl combination pH electrode. Measurement of acid dissociation constants were not corrected for ionic strength.

Synthesis of 2,7-bis(di(2-pyridyl)methyl)-1,8-naphthyridine (DPMN). *n*-Butyllithium (1.6 M in hexanes, 125 mL, 200 mmol) was added dropwise to a stirred solution of freshly distilled 1,1-di-(2-pyridyl)methane (34.0 g, 200 mmol) in 400 mL of THF at 0° C under a N_2 atmosphere. The red solution was stirred for 30 min. after which 2,7-dichloro-1,8-naphthyridine (17.3 g, 87 mmol) was added. The purple solution formed was stirred for 16 h as the vessel warmed to room temperature. After addition of 50 mL of water, the mixture was filtered. The orange precipitate was dissolved in a 1:1 CH_2Cl_2:H_2O mixture and filtered to remove residual 2,7-dichloro-1,8-naphthyridine. The organic fraction was washed with H_2O (2 x 100 mL) and then dried over $MgSO_4$ and evaporated to dryness. The crude material was crystallized from hot acetonitrile to give light orange crystals of 2,7-bis(1,1-di-(2-pyridyl)methyl)-1,8-naphthyridine (DPMN) (yield: 9.0 g, 19 mmol, 22%). Additional crystallizations from hot ACN (2 times) was performed to prepare light orange X-ray quality crystals. **^{1}H NMR** (d_2-dichloromethane, 600.13 MHz): δ 8.53 (d, J_{HH} = 4.1 Hz, of d, J_{HH} = 1.7 Hz, d, J_{HH} = 0.9 Hz, 4H), 8.10 (d, J_{HH} = 8.4 Hz, 2H), 7.65 (t, J_{HH} = 7.7 Hz, of d, J_{HH} = 1.9 Hz, 4H), 7.60 (d, J_{HH} = 8.4 Hz, 2H), 7.37 (d, J_{HH} = 7.9 Hz, 4H), 7.17 (d, J_{HH} = 7.4 Hz, of d, J_{HH} = 4.9 Hz, of d, J_{HH} = 0.9 Hz, 4H), 6.16 (s, 2H). **^{13}C{^{1}H} NMR** (d_2-dichloromethane, 150.92 MHz): δ 165.6, 161.4, 155.8, 149.9, 137.3, 137.0, 124.9, 123.9, 122.4, 120.7, 65.4). **EA** Anal. Calcd (%) for $C_{30}H_{22}N_6$ (466.55): C, 77.23; H, 4.75; N, 18.01. Found: C, 77.55; H, 4.70; N, 17.85.

Synthesis of 2,7-bis(fluorodi(2-pyridyl)methyl)-1,8-naphthyridine (DPFN). SelectFluor (10.2 g, 29 mmol) was dissolved in 175 mL of ACN. DPMN (6.7 g, 20 mmol) was added and the mixture was refluxed for 16 hrs during which the DPMN dissolved. To the solution was added 75 mL of CH_2Cl_2 and 75 mL of H_2O. The organic phase was washed with H_2O (2 x 50 mL) and then dried over $MgSO_4$ and evaporated to dryness leaving a yellow solid. The product was purified by crystallization from slow cooling of a hot ACN solution as pale yellow crystals (2.8 g, 5.6 mmol, 39%). Further crystallization from hot ACN (2 times) was performed to prepare analytically pure colorless material and X-ray quality crystals. **^{1}H NMR** (d_2-dichloromethane, 300.13 MHz): δ 8.56 (d, J_{HH} = 4.5 Hz, 4H), 8.25 (d, J_{HH} = 8.7 Hz, 2H), 7.82 (d, J_{HH} = 8.4 Hz, 2H), 7.77 (t, J_{HH} = 8.1 Hz, of d, J_{HH} = 1.5 Hz, 4H), 7.58 (d, J_{HH} = 7.8 Hz, 4H), 7.29 (t, J_{HH} = 4.8 Hz, of d, J_{HH} = 1.5 Hz, 4H). **^{13}C{^{1}H} NMR** (d_2-dichloromethane, 100.62 MHz): δ 164.2 (d, $^2J_{CF}$ = 25 Hz), 159.9 (d, $^2J_{CF}$ = 25 Hz), 154.1, 149.3, 137.6, 137.2, 123.8, 123.1 (d, $^3J_{CF}$ = 6 Hz), 122.3 (d, $^3J_{CF}$ = 5 Hz), 121.8, 100.8 (d, $^1J_{CF}$ = 179 Hz)). **^{19}F{^{1}H} NMR** (d_2-dichloromethane, 376.48 MHz): δ −142.1. **EA** Anal. Calcd (%) for $C_{30}H_{20}F_2N_6$ (502.52): C, 71.70; H, 4.01; N, 16.72. Found: C, 71.53; H, 4.15; N, 16.64. **UV/Vis** (acetonitrile, λ [nm] (ε [$M^{-1}\cdot cm^{-1} \div 10^3$])): 214 (82.5 ± 9.0), 255 (17.6 ± 1.8), 259 (17.8 ± 1.8), 308 (9.6 ± 0.97), 315 (10.2 ± 1.0).

Synthesis of $[Co_2(\mu\text{-}OH)_2(OH_2)_2(DPFN)][NO_3]_4$ (1). DPFN (0.3 g, 0.6 mmol) was dissolved with heating in 120 mL of EtOH to which was added a solution of $Co(NO_3)\cdot 6H_2O$ (0.35 g, 1.2 mmol) in 30 mL of EtOH. The resulting orange solution was stirred for 2 min. after which 30% H_2O_2 (600 μL, 5.9 mmol) was added. The solution was filtered after stirring for 30 min. to afford a pink precipitate that was washed with EtOH (2 x 30 mL) followed by Et_2O (2 x 30 mL) and air

dried. The product was dissolved in a minimum amount of hot H_2O (~ 2 mL) and crystallized overnight to afford X-ray quality crystals (0.43 g, 0.080 mmol, 76%). **^{1}H NMR** (d_2-water, 300.13 MHz): δ 9.19 (d, J_{HH} = 8.7 Hz, 2H), 9.10 (d, J_{HH} = 5.1 Hz, 4H), 8.85 (d, J_{HH} = 7.2 Hz, 2H), 8.45 (m, 8H), 7.94 (t, J_{HH} = 5.4 Hz, 4H). **EA** Anal. Calcd (%) for $C_{30}H_{26}Co_2F_2N_{10}O_{16}$ (938.45): C, 38.40; H, 2.79; N, 14.93. Found: C, 38.10; H, 2.85; N, 14.51. **UV/Vis** (water, λ [nm] (ε [$M^{-1}\cdot cm^{-1} \div 10^3$])): 312 (11.8 ± 0.4), 324 (12.4 ± 0.4), 522 (0.30 ± 0.01).

Synthesis of [{Co_2(μ-OH)$_2$(DPFN)}$_2$(κ^2,κ^2-PO_4)][NO_3]$_5$·15 H_2O (2). 1 (0.05 g, 0.05 mmol) was dissolved in 5 mL of water to which was added a solution of K_2HPO_4 (0.009 g, 0.05 mmol) and KOH (0.05 mL of 1M aq. soln) in 5 mL of water. The solution was stirred for 16 hr. after which the solvent was removed under vacuum. The red precipitate was dissolved in 10 mL of EtOH leaving undissolved a white powder. The solution was filtered and the solvent removed under vacuum after which the EtOH step was repeated. The product was dissolved in a minimum amount of water (~ 0.5 mL) and crystallized by vapor diffusion of acetonitrile into the aqueous solution to afford a crude mixture containing X-ray quality crystals of **2** (0.026 g, 0.013 mmol, 52%). **EA** Anal. Calcd (%) for $C_{60}H_{44}Co_4F_4N_{17}O_{38}$ (1984.04): C, 36.32; H, 3.76; N, 12.00. Found: C, 36.91; H, 3.53; N, 11.10.

X-ray Crystallography Details. X-ray diffraction data were collected using Bruker AXS three-circle diffractometers coupled to a CCD detector with graphite-monochromated Mo Kα (λ = 0.71073 Å) or Cu Kα (λ = 1.5478 Å) radiation cooled under a stream of N_2 to 100 K. Raw data were integrated and corrected for Lorentz and polarization effects using Bruker APEX2 v. 2009.1. Absorption corrections were applied using SADABS. The structures were solved by direct methods using SHELXS and refined against F^2 on all data by full-matrix least squares with SHELXL-97. Refinement details for all compounds are detailed below:

DPMN

All non-hydrogen atoms were refined anisotropically; hydrogen atoms were included into the model at their geometrically calculated positions and refined using a riding model.

DPFN

All non-hydrogen atoms were refined anisotropically; hydrogen atoms were included into the model at their geometrically calculated positions and refined using a riding model.

[Co_2(μ-OH)$_2$(OH_2)$_2$(DPFN)][NO_3]$_4$ (**1**)

All non-hydrogen atoms were refined anisotropically; hydrogen atoms were included into the model at their geometrically calculated positions and refined using a riding model except hydrogen atoms of the aquo and hydroxo ligands, which were located from the electron difference map.

[{Co_2(μ-OH)$_2$(DPFN)}$_2$(κ^2,κ^2-PO_4)][NO_3]$_5$·7 H_2O·CH_3CN (**2**)

All non-hydrogen atoms were refined anisotropically; hydrogen atoms were included into the model at their geometrically calculated positions and refined using a riding model except hydrogen atoms of the water solvate molecules and hydroxo ligands, which were located from the electron difference map if possible or excluded when not possible. Two nitrate anions were located on an inversion center or mirror plane and were modeled as disordered over two symmetry-related sites with appropriate structure occupancy factors. One nitrate anion was located on a mirror plane and was modeled as disordered over two symmetry-related sites and

one additional rotated site with a total structure occupancy factor of 1. For the site with the lowest occupancy, one nitrogen-oxygen bond length was restrained to a chemically appropriate value due to disorder. One nitrate anion was disordered over two sites and was modeled with half occupancy of each site. Due to disorder, bond lengths were restrained to chemically appropriate values, one site was restained to be coplanar, and the aniosotropic displacement parameters of the two sites were restrained to be similar. Two water solvate molecules were found to have partial occupancy and were modeled with 0.5 structural occupancy factors. For four water solvate molecule sites, hydrogen atoms could not be located from the electron difference map and were omitted from the model. For other water solvate molecules hydrogen bond lengths and angles were restrained to chemically appropriate values and isotropic displacement parameters were constrained to 1.5 times the isotropic value of the parent oxygen atom. For hydroxyl ligand hydrogen atoms, bond lengths were restrained to chemically appropriate values.

Table 1. Experimental details for the X-ray crystal structures of DPMN, DPFN, **1**, **2**.

	DPMN	DPFN	**1**	**2**
Chemical formula	$C_{30}H_{22}N_6$	$C_{30}H_{20}F_2N_6$	$C_{30}H_{26}Co_2F_2N_{10}O_{16}$	$C_{62}H_{61}Co_4F_4N_{18}O_{30}P$
Formula Mass	466.54	502.52	938.47	1880.96
Crystal system	Triclinic	Monoclinic	Monoclinic	Monoclinic
a/Å	8.072(2)	8.7660(5)	26.800(2)	16.5997(17)
b/Å	12.076(3)	23.8721(16)	10.8131(8)	12.8750(14)
c/Å	12.881(3)	11.4381(7)	12.7351(10)	18.2563(19)
α/°	69.775(4)	90.00	90.00	90.00
β/°	84.874(4)	96.074(4)	106.8370(10)	112.203(2)
γ/°	79.297(4)	90.00	90.00	90.00
Unit cell volume/Å^3	1157.3(5)	2380.1(3)	3532.3(5)	3612.4(7)
Temperature/K	131(2)	100(2)	100(2)	100(2)
Space group	*P*1	*P*2(1)/*c*	*C*2/*c*	*P*2(1)/*m*
No. of formula units per unit cell, *Z*	2	4	4	2
No. of reflections measured	4230	11151	3207	50251
No. of independent reflections	4230	3941	3207	6842
R_{int}	0.0281	0.0302	0.0313	0.0456
Final R_1 values ($I > 2\sigma(I)$)	0.0353	0.0360	0.0245	0.0739
Final $wR(F^2)$ values ($I > 2\sigma(I)$)	0.0820	0.0934	0.0680	0.2159
Final R_1 values (all data)	0.0499	0.0419	0.0256	0.0907
Final $wR(F^2)$ values (all data)	0.0889	0.0976	0.0692	0.2403
Goodness of fit on F^2	1.243	1.041	1.091	1.034

Electrochemistry Details. Electrochemical experiments were recorded with a BASi Epsilon potentiostat using a 3 mm diameter glassy carbon working electrode, a Pt wire counter electrode and a [Ag]/[AgCl] reference electrode (sat. KCl, 0.197 V vs. NHE). The glassy carbon working electrode was polished between runs with an alumina slurry and rinsed with water. Buffer solutions were made using Milli-Q water and a phosphate buffer (0.1 M H_3PO_4, 0.1 M KH_2PO_4, or 0.1 M K_2HPO_4) and the pH was adjusted using aliquots of a 1 M KOH solution with an analyte concentration of 2 mM. The potentials of redox events were measured as the potential at peak current from a differential pulse voltammogram. Controlled potential electrolysis (CPE) experiments were conducted in a pH 9.0 phosphate buffer solution for a period of 10 min at 1.6 V. Due to initial deposition observed from the buffer solution onto the electrode, the electrode was pretreated by CPE for 10 min at 1.6 V in pH 9.0 phosphate buffer solution only before conducting the experiments.

Computational Details. DFT calculations were performed at the Molecular Graphics and Computation Facility of the University of California, Berkeley using the Gaussian 09 suite of *ab initio* programs.[19] Atoms were modeled using the meta generalized gradient approximation functional M06,[20] and all-electron 6-31G** basis sets for all atoms.[21] This functional/basis set combination was compared with combinations of the ωB97xD,[22] TPSS,[23] and B3LYP[24] with the cc-PVDZ (C,H,N,O)[25] / cc-PVTZ[26] (Cu) and STO-3G[27] basis sets as the closest match metrically of the optimized computational structure to the crystal structure of **1**. The DFT structures were optimized as gas phase structures using unrestricted wavefunctions. Protonation and oxidation states different from **1** were created by modification of **1** using Gaussview and optimized. Ground states were confirmed by comparison with optimized higher-spin analogues up to the high-spin limit for two high-spin cobalt centers. The 3D molecular structure figures displayed were drawn using the Gaussview and Adobe Illustrator visualization and manipulation programs. Molecular orbital surfaces were exported from Gaussview as cubefiles, visualized in VMD[28] and rendered with the Pov-Ray raytracer program.

References

(1) Lewis, N. S.; Nocera, D. G. *Proc. Natl. Acad. Sci.* **2006**, *103*, 15729–15735.
(2) Matsumoto, Y.; Sato, E. *Mater. Chem. Phys.* **1986**, *14*, 397–426.
(3) Rüttinger, W.; Dismukes, G. C. *Chem. Rev.* **1997**, *97*, 1–24.
(4) Yagi, M.; Kaneko, M. *Chem. Rev.* **2000**, *101*, 21–36.
(5) Romero, I.; Rodríguez, M.; Sens, C.; Mola, J.; Rao Kollipara, M.; Francàs, L.; Mas-Marza, E.; Escriche, L.; Llobet, A. *Inorg. Chem.* **2008**, *47*, 1824–1834.
(6) Deng, Z.; Tseng, H.-W.; Zong, R.; Wang, D.; Thummel, R. *Inorg. Chem.* **2008**, *47*, 1835–1848.
(7) Sala, X.; Romero, I.; Rodríguez, M.; Escriche, L.; Llobet, A. *Angew. Chem. Int. Ed.* **2009**, *48*, 2842–2852.
(8) Walter, M. G.; Warren, E. L.; McKone, J. R.; Boettcher, S. W.; Mi, Q.; Santori, E. A.; Lewis, N. S. *Chem. Rev.* **2010**, *110*, 6446–6473.
(9) Esswein, A. J.; McMurdo, M. J.; Ross, P. N.; Bell, A. T.; Tilley, T. D. *J. Phys. Chem. C* **2009**, *113*, 15068–15072.
(10) Kanan, M. W.; Nocera, D. G. *Science* **2008**, *321*, 1072–1075.
(11) Artero, V.; Chavarot-Kerlidou, M.; Fontecave, M. *Angew. Chem. Int. Ed.* **2011**, *50*, 7238–7266.

(12) Wang, L.-P.; Van Voorhis, T. *J. Phys. Chem. Lett.* **2011**, *2*, 2200–2204.
(13) Surendranath, Y.; Kanan, M. W.; Nocera, D. G. *J. Am. Chem. Soc.* **2010**, *132*, 16501–16509.
(14) Yin, Q.; Tan, J. M.; Besson, C.; Geletii, Y. V.; Musaev, D. G.; Kuznetsov, A. E.; Luo, Z.; Hardcastle, K. I.; Hill, C. L. *Science* **2010**, *328*, 342–345.
(15) Wasylenko, D. J.; Ganesamoorthy, C.; Borau-Garcia, J.; Berlinguette, C. P. *Chem. Commun.* **2011**, *47*, 4249–4251.
(16) Stracke, J. J.; Finke, R. G. *J. Am. Chem. Soc.* **2011**, *133*, 14872–14875.
(17) Rigsby, M. L.; Mandal, S.; Nam, W.; Spencer, L. C.; Llobet, A.; Stahl, S. S. *Chem. Sci.* **2012**, *3*, 3058.
(18) Newkome, G. R.; Garbis, S. J.; Majestic, V. K.; Fronczek, F. R.; Chiari, G. *J. Org. Chem.* **1981**, *46*, 833–839.
(3) Gaussian 09, Revision C01, Frisch, M. J.; Trucks, G. W.; Schlegel, H. B.; Scuseria, G. E.; Robb, M. A.; Cheeseman, J. R.; Scalmani, G.; Barone, V.; Mennucci, B.; Petersson, G. A.; Nakatsuji, H.; Caricato, M.; Li, X.; Hratchian, H. P.; Izmaylov, A. F.; Bloino, J.; Zheng, G.; Sonnenberg, J. L.; Hada, M.; Ehara, M.; Toyota, K.; Fukuda, R.; Hasegawa, J.; Ishida, M.; Nakajima, T.; Honda, Y.; Kitao, O.; Nakai, H.; Vreven, T.; Montgomery, Jr., J. A.; Peralta, J. E.; Ogliaro, F.; Bearpark, M.; Heyd, J. J.; Brothers, E.; Kudin, K. N.; Staroverov, V. N.; Kobayashi, R.; Normand, J.; Raghavachari, K.; Rendell, A.; Burant, J. C.; Iyengar, S. S.; Tomasi, J.; Cossi, M.; Rega, N.; Millam, N. J.; Klene, M.; Knox, J. E.; Cross, J. B.; Bakken, V.; Adamo, C.; Jaramillo, J.; Gomperts, R.; Stratmann, R. E.; Yazyev, O.; Austin, A. J.; Cammi, R.; Pomelli, C.; Ochterski, J. W.; Martin, R. L.; Morokuma, K.; Zakrzewski, V. G.; Voth, G. A.; Salvador, P.; Dannenberg, J. J.; Dapprich, S.; Daniels, A. D.; Farkas, Ö.; Foresman, J. B.; Ortiz, J. V.; Cioslowski, J.; Fox, D. J. Gaussian, Inc., Wallingford CT 2009.
(20) Zhao, Y.; Truhlar, D. G. *Theor. Chem. Acc.* **2007**, *120*, 215–241.
(21) Hariharan, P. C.; Pople, J. A. *Theor. Chim. Acta* **1973**, *28*, 213–222.
(22) Chai, J.-D.; Head-Gordon, M. *Phys. Chem. Chem. Phys.* **2008**, *10*, 6615–6620.
(23) Tao, J.; Perdew, J. P.; Staroverov, V. N.; Scuseria, G. E. *Phys. Rev. Lett.* **2003**, *91*, 146401.
(24) Becke, A. D. *J. Chem. Phys.* **1993**, *98*, 5648–5652.
(25) Dunning, T. H. *J. Chem. Phys.* **1989**, *90*, 1007–1023.
(26) Kendall, R. A.; Dunning, T. H.; Harrison, R. J. *J. Chem. Phys.* **1992**, *96*, 6796–6806.
(27) Hehre, W. J.; Stewart, R. F.; Pople, J. A. *J. Chem. Phys.* **1969**, *51*, 2657–2664.
(28) Humphrey, W.; Dalke, A.; Schulten, K. *J. Mol. Graphics* **1996**, *14*, 33–38.

Chapter 2

A Series of Dinuclear First-Row Transition Metal Complexes with a Naphthyridine-Based Dinucleating Ligand

Introduction

The study of multinuclear metal complexes is an active area of research since multinuclear metal centers play an important role in various catalytic systems of interest, including metalloenzymes and the active sites of heterogeneous catalysts.[1] In the case of dinuclear systems, many metalloenzymes are known for which interaction of the two metal centers is thought to play a crucial role in the catalytic function of the enzyme including hemerythrin[2], methane monooxygenase[3], ribonucleotide reductase[4], urease[5], purple acid phosphatase[6], catechol oxidase[7], and arginase.[8] Indeed, even enzymes containing multinuclear active sites such as the tetramanganese center in the Oxygen Evolving Complex of Photosystem II are thought to have only two manganese centers that participate in bond-making and bond-breaking events in the catalytic cycle.[9] On this basis, many synthetic water oxidation catalysts have been developed with dinuclear metal centers such as the ruthenium blue dimer, $[(Ru(bpy)_2(OH_2))_2(\mu\text{-}O)][ClO_4]_4$, which generally outperform similar mononuclear catalysts.[10–13] The dinuclear metal complexes are expected to have several advantages over mononuclear complexes including cooperative reactivity of substrates with the neighboring metal centers, the requirement of lower oxidation or reduction potentials to store multiple redox equivalents on the complex, promotion of catalysis via of multielectron processes, and potentially beneficial electronic interactions between the metal centers.[1,14]

Interest in the catalytic capabilities of dinuclear metal complexes has led to the study of specifically designed dinucleating ligands, for which the structure is tailored to a specific purpose.[15,16] Such ligands can be designed with several beneficial properties. The ligand can be rigid, to enforce a fixed coordination environment around the metal centers, in a manner analogous to that provided by polypeptide frameworks in metalloproteins. Such ligands may also be employed to dictate a given metal-metal distance, with controlled electronic interactions between the metal centers.[17] Also, the number and positions of donor atoms can be controlled to achieve a particular coordination geometry, and influence the coordination modes of other ligands.

This report describes the dinucleating properties of a ligand based on the 1,8-naphthyridine core, 2,7-bis(di(2-pyridyl)fluoromethyl)-1,8-naphthyridine (DPFN). The 1,8-naphthyridine core has been described as a "masked carboxylate," capable of emulating the *syn*, *syn* bridging mode of the carboxylate group commonly found in biological systems.[18] In addition, substitution of the naphthyridine group at the 2 and 7 positions easily affords additional chelating sites at geometric positions favorable for coordination to metal centers bound to the naphthyridyl-N position.[19–22] In DPFN, the 2 and 7 positions of the naphthyridine core have been substituted with di(2-pyridyl)fluoromethyl groups (Figure 1). This arrangement gives the resulting compound DPFN with six chelating N sites that favorably bind two metal centers, each with 3 N donors coordinated in a facial manner. In this arrangement, the metal-metal distance is expected to be in the range of 2.3 to 4.0 Å[22] and, for metal centers preferring octahedral coordination environments, two coordination sites between the two metal centers are suitable for bridging ligands. With two such bridging donor atoms, the dinuclear complex adopts a diamond-shaped configuration. Each metal center has an additional open coordination site that may accommodate terminal ligands in a *syn* geometry. This structural feature is of interest in the design of synthetic molecular water oxidation catalysts,[23] as well as other catalysts (e.g., for oxidative dehydrogenation).[24,25] In this report, the dinucleating ability of DPFN is described for

the first-row transition metals from manganese to copper, with chloro, hydroxo, and aqua bridging ligands that give the diamond-shaped core structure.

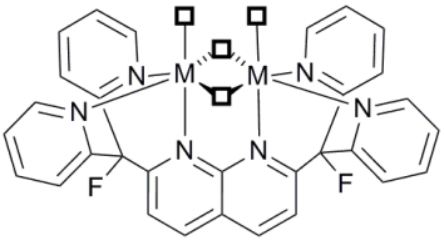

Figure 1. Coordination geometry of DPFN around two octahedral metal centers. Coordination sites for secondary ligands are represented with open squares.

Results

Synthesis of DPFN complexes. The DPFN ligand was prepared as described previously.[26] Metal DPFN complexes of Mn, Fe, Co, Ni, and Cu were prepared with metal chloride and hydrated metal nitrate starting materials, as shown in Scheme 1. Unlike the later transition elements, manganese did not form a dinuclear metal complex with DPFN in methanol or ethanol, regardless of the number of equivalents of manganese starting material used in the reaction. Instead, the complex $[Mn(DPFN)_2][NO_3]_2$ (**1**) preferentially formed in these reaction mixtures. By ESI mass spectrometry, it was shown that the $[Mn(DPFN)_2]^{2+}$ cation was also formed when $Mn(OTf)_2 \cdot 6H_2O$ and $Mn(ClO_4)_2 \cdot 6H_2O$ were used as starting materials.

Scheme 1. Synthesis of complexes **1**-**6**.

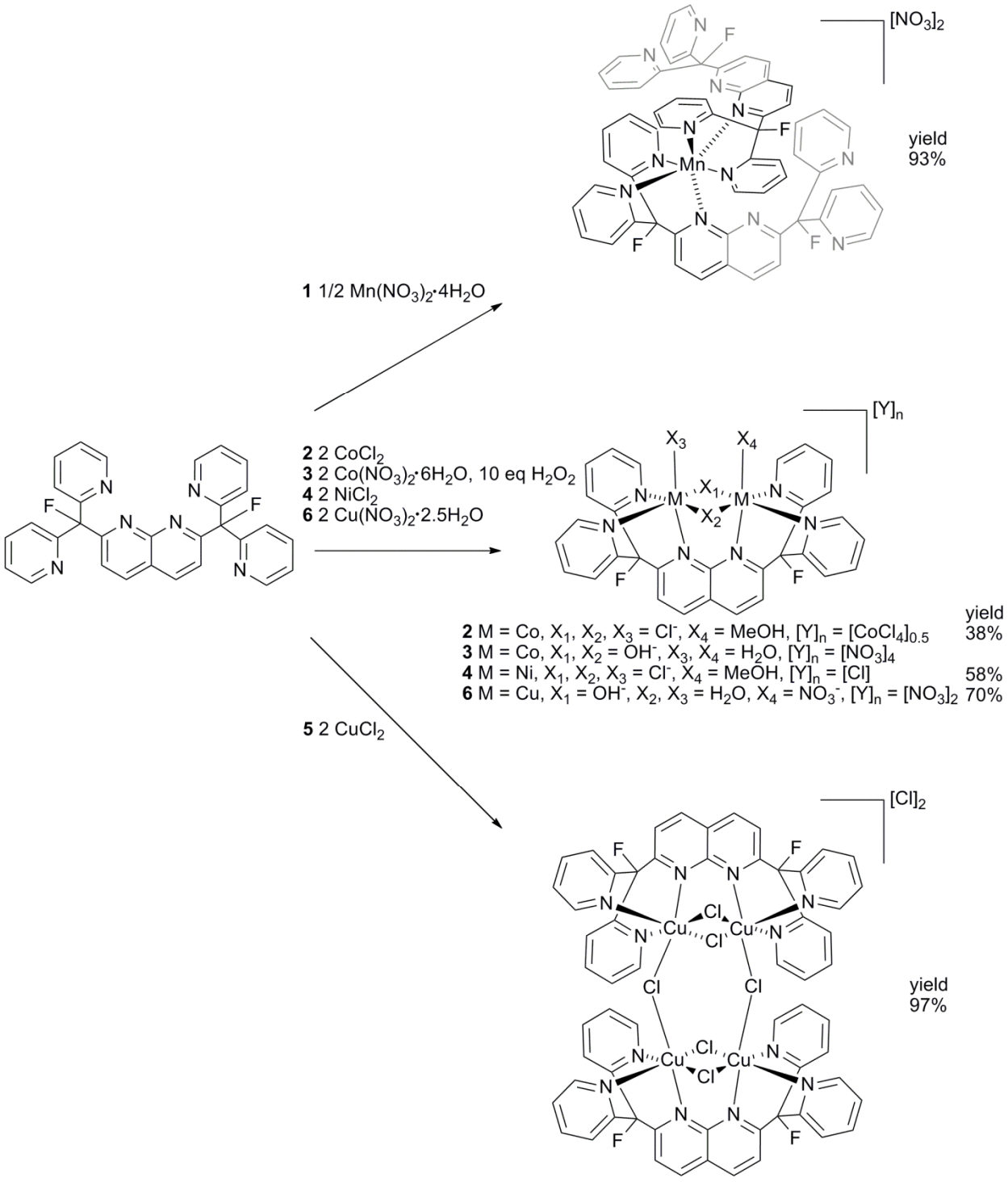

Reactions of anhydrous cobalt(II), nickel(II), and copper(II) chloride, or the corresponding hydrated nitrate salts, with DPFN resulted in the formation of dinuclear or tetranuclear metal complexes. For the metal chlorides, two equivalents were added to one equivalent of DPFN in ethanol solution, and the resulting reaction mixture was stirred for 16 h. Evaporation of solvent and crystallization by vapor diffusion of diethyl ether or tetrahydrofuran into a solution of methanol or ethanol resulted in crystallization of $[Co_2(DPFN)(\mu\text{-}Cl)_2Cl(MeOH)]_2[CoCl_4]$ (**2**), $[Ni_2(DPFN)(\mu\text{-}Cl)_2Cl(MeOH)][Cl]$ (**4**), and $Cu_2(DPFN)(\mu\text{-}Cl)_2Cl_2$ (**5**) which were isolated and dried at elevated temperatures (~50 °C) under dynamic vacuum. In the reaction of $CoCl_2$ with DPFN in ethanol, green crystals formed on concentration of the mother liquor under vacuum. These crystals could not be redissolved in ethanol, but were recrystallized by vapor diffusion of diethyl ether into a methanol solution to give **2**. This indicates that formation of the $CoCl_4^{2-}$ anion of **2** may be driven by a favorable precipitation from solution. Reactions of the cobalt and copper nitrates, $Co(NO_3)_2{\cdot}6H_2O$ and $Cu(NO_3)_2{\cdot}2.5H_2O$, with DPFN in ethanol or methanol led to formation of the hydroxo- or aqua-bridged complexes $[Co_2(DPFN)(\mu\text{-}OH)_2(OH_2)_2][NO_3]_4$ (**3**) and $[Cu_2(DPFN)(\mu\text{-}OH)(\mu\text{-}OH_2)(OH_2)(NO_3)][NO_3]_2$ (**6**). The formation of previously reported **3**,[26] unlike the related reactions of the DPFN ligand, results in oxidation of the metal centers. This oxidation occurs spontaneously under laboratory atmosphere; however, the yield of this complex is greatly increased by addition of excess (10 equiv) H_2O_2 to freshly prepared solutions of $Co(NO_3)_2{\cdot}6H_2O$ and DPFN. If the addition of H_2O_2 is delayed by more than 10 min, significant formation of the $[Co(DPFN)_2]^{2+}$ species (presumably analogous to $[Mn(DPFN)_2]^{2+}$) was observed (by ESI mass spectrometry).

Crystal structures of 1-6. Single crystals of compounds **1**-**6** were obtained by vapor diffusion of diethyl ether or tetrahydrofuran into methanol or ethanol solutions. The mononuclear manganese compound **1** is shown in Figure 2. The manganese center is bound to two DPFN ligands to give a distorted octahedral geometry, in which each DPFN ligand coordinates in a facial manner via two pyridyl and one naphthyridyl nitrogen donors. The distortion from octahedral geometry can be attributed to steric constraints imposed by the accommodation of two DPFN ligands, which results in small N–Mn–N bond angles (81(3)° on average) associated with a given DPFN ligand, and large N–Mn–N bond angles (107(4)° on average) involving separate DPFN ligands.

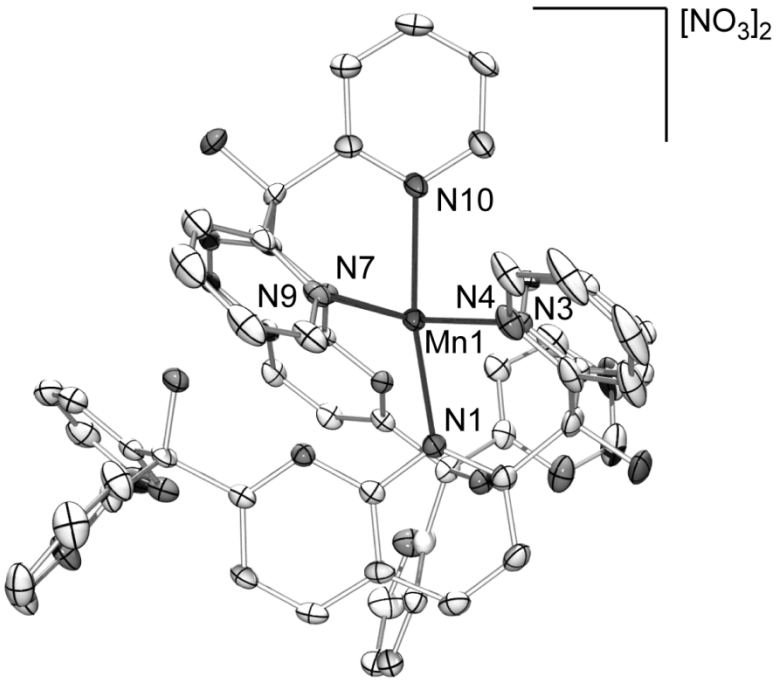

Figure 2. X-ray crystal structure of **1**. Thermal ellipsoids are shown at 50% probability; hydrogen atoms, solvate molecules, and counterions are omitted for clarity. Selected bond lengths [Å] and angles [°]: Mn1–N1 2.216(2), Mn1–N3 2.234(2), Mn1–N4 2.349(2), Mn1–N7 2.222(2), Mn1–N9 2.249(2), Mn1–N10 2.322(2), N1–Mn1–N10 168.31(7), N4–Mn1–N7 168.73(7), N3–Mn1–N9 165.17(7).

Crystal structures of the dinuclear and tetranuclear metal complexes **2**-**6** are shown in Figure 3 and distance and angle measurements are given in Table 1. All of the metal centers in **2**-**6** are six-coordinate in the solid state with approximate octahedral geometries. For each metal center, three of the coordination sites are occupied by the DPFN ligand in a *facial* coordination manner. The two coordination sites *trans* to the coordinated DPFN pyridyl nitrogens are occupied by the bridging chloro, hydroxo, or aqua ligands, such that the two coordination octahedra for the metal centers share an edge. With the exception of **5,** the coordination site *trans* to the coordinated naphthyridine nitrogen is occupied by terminal chloro, aqua, methanol, or nitrato ligands. In the tetranuclear complex **5**, the chloro ligands *trans* to the coordinated naphthyridine nitrogens form a bridge between two facing $Cu_2(\mu\text{-}Cl)_2$(DPFN) moieties. The $M_2(\mu\text{-}X)_2$ metal-metal distances in **2**-**6** range from 2.7826(5) to 3.2410(11) Å, and correlate well to the oxidation state of the metal and the metal-bridging ligand bond lengths. Thus, the higher 3+ oxidation state of cobalt, and thus smaller ionic radius, in **5** compared to the other complexes all containing M(II) centers results in the shortest metal-metal distance of 2.7826(5) Å. Also, the shorter bond lengths to the hydroxo and aqua bridging ligands of 1.917(5) Å and 2.087(4) Å, respectively, in the copper complex **6**, results in a metal-metal distance of 2.9534(3) Å while the chloro-bridged copper complex **5**, with an average M–(μ-Cl) bond length of 2.294(2), has a metal-metal distance of 3.2410(11).

Table 1. Selected structural parameters for complexes **2**-**6**

	2	**3**	**4**	**5**	**6**
distance (Å) / angle (°)	$Co_2(\mu\text{-}Cl)_2$	$Co_2(\mu\text{-}OH)_2$	$Ni_2(\mu\text{-}Cl)_2$	$[Cu_2(\mu\text{-}Cl)_2]_2$	$Cu_2(\mu\text{-}OH)(\mu\text{-}OH_2)$
M1–M2	3.2382(8)	2.7826(5)	3.2217(8)	3.2410(11)	2.9534(3)
M1–Cl/O1	2.3995(11)	1.8703(16)[a]	2.3504(13)	2.2927(14)	2.0905(12)
M1–Cl/O2	2.3968(12)	1.8787(17)	2.3674(13)		1.9204(11)
M2–Cl/O1	2.4326(11)		2.3672(13)	2.2961(14)	2.0842(11)
M2–Cl/O2	2.3878(11)		2.3877(12)		1.9136(11)
M1–N1	2.250(3)	1.941(2)	2.180(3)	2.609(4)	2.4056(13)
M2–N2	2.346(3)		2.233(4)		2.3767(13)
M1–N3	2.108(3)	1.918(2)	2.057(4)	2.015(4)	2.0069(13)
M1–N4	2.120(3)	1.9306(2)	2.068(4)	2.005(4)	2.0085(13)
M2–N5	2.095(3)		2.063(4)		1.9787(14)
M2–N6	2.126(3)		2.075(4)		2.0210(13)
M1–X (terminal)[b]	2.045(3)	1.908(2)	2.076(3)	2.6421(9)	2.3004(13)
M2–X (terminal)[c]	2.4132(11)		2.3893(13)		2.3747(12)
M1–Cl/O1–M2	84.15(4)	95.85(7)	86.14(4)	89.87(5)	90.05(4)
M1–Cl/O2–M2	85.19(4)		85.30(4)		100.76(5)
equatorial plane angle[d]	26.68(8)	12.14(2)	25.57(7)	36.61(5)	25.64(5)

[a]Due to C_2 symmetry, only half of the parameters for **3** and **5** are unique. The atom labels are modified as follows: M2 = M1', Cl/O2 = O1', N3 = N2, N4 = N3. [b]X = (**2**) O1, (**3**) O2, (**4**) O1, (**5**) Cl2, (**6**) O3. [c]X = (**2**) Cl3, (**4**) Cl3, (**6**) O4. [d]Defined as the angle between the least squares planes determined by (M1 N3 N4 Cl/O1 Cl/O2) and (M2 N5 N6 Cl/O1 Cl/O2).

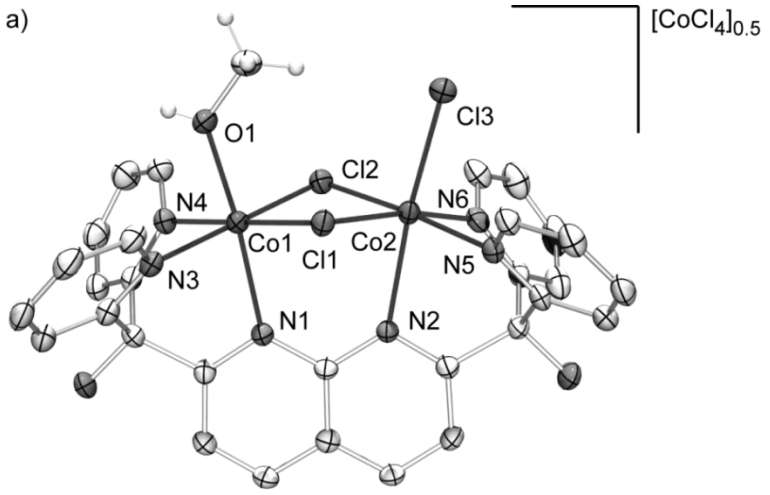

2 $[Co_2(DPFN)(\mu\text{-}Cl)_2Cl(MeOH)]_2[CoCl_4]$

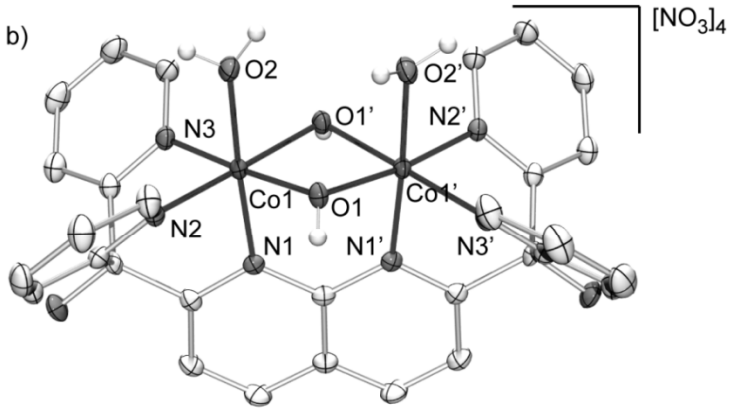

3 $[Co_2(DPFN)(\mu\text{-}OH)_2(OH_2)_2][NO_3]_4$

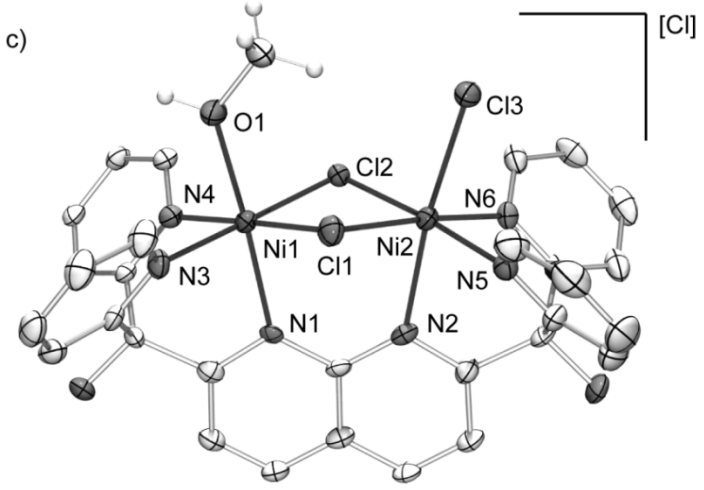

4 $[Ni_2(DPFN)(\mu\text{-}Cl)_2Cl(MeOH)][Cl]$

continued on next page

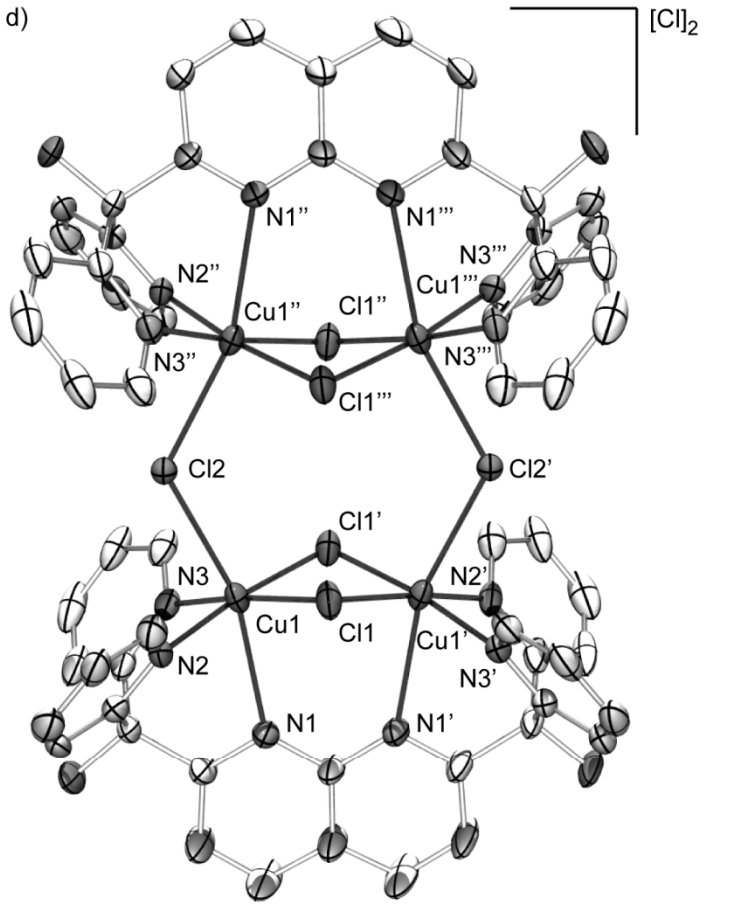

5 $[Cu_4(DPFN)_2(\mu\text{-}Cl)_6]Cl_2$

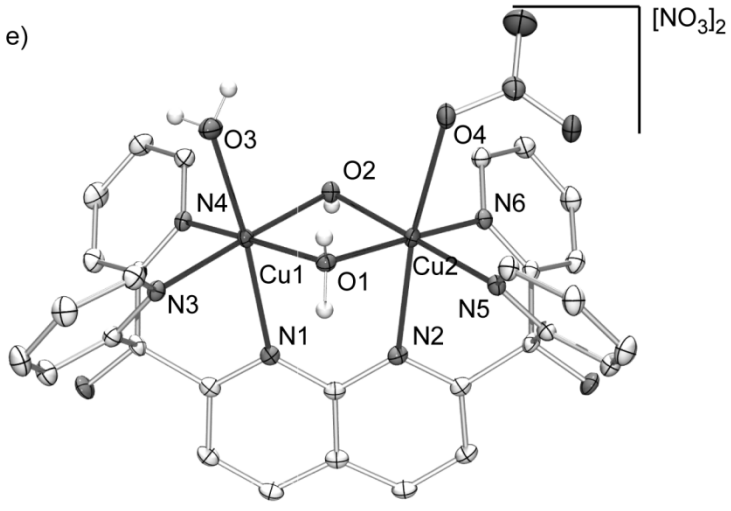

6 $[Cu_2(DPFN)(\mu\text{-}OH)(\mu\text{-}OH_2)(OH_2)(NO_3)][NO_3]_2$

Figure 3. Crystal structures of complexes **2**-**6**. Thermal ellipsoids are shown at 50% probability; hydrogen atoms of DPFN, solvate molecules, and counterions are omitted for clarity.

Jahn-Teller distortions are most evident in the M–N naphthyridine bond lengths of the d^9 copper complexes **5** (2.609(4) Å) and **6** (av 2.39(2) Å). These bond lengths are significantly longer than the average Cu–N pyridine bond lengths of 2.010(7) (for **5**) and 2.004(18) Å (for **6**). For the d^7-cobalt centers in complex **3**, the distortion is less pronounced with an average Co–N naphthyridine bond length of 2.21(4) Å and an average Co–N pyridine bond length of 2.066(8) Å.

In general for these complexes, there is no significant deviation from planarity for the equatorial planes defined by the MN_2X_2 atoms (metal, pyridyl nitrogen atoms and bridging X groups). Root-mean-square deviations for the equatorial MN_2X_2 planes range from 0.030 Å for **4** to 0.061 Å for **2**. In **2**, the largest deviation, 0.106(1) Å, occurs for Co2 which is drawn out of the equatorial MN_2X_2 plane by interaction with the terminal chloro ligand. In contrast, Co1, for which the terminal ligand is methanol, deviates from its MN_2X_2 least-squares plane by only 0.010(1) Å. Similarly, in **4** the largest deviation from the equatorial MN_2X_2 planes is associated with the terminal-chloride-bound Ni2 (0.056(1) Å) while the methanol-bound Ni1 exhibits no significant deviation (–0.001 (1) Å). Complex **5** exhibits a relatively large out-of-plane deviation of 0.091(2) Å for Cu1, which is possibly associated with the unique tetranuclear structure, while the other dinuclear structures exhibit relatively small maximum deviations of 0.0595(6) Å for **6**, 0.056(1) Å for **4**, and 0.049(2) for **3**.

Another structural parameter that varies significantly in **2**-**6** is the angle made between the $M1N_2X_2$ and $M2N_2X_2$ equatorial planes. Ideally, with pure octahedral geometries for the metal centers and an ideal fit inside the pocket of the ligand, the $M1N_2X_2$ and $M2N_2X_2$ equatorial planes would be coplanar. However, in each complex the equatorial planes are angled such that the single-atom bridging ligands are puckered away from the naphthyridine ring of the DPFN ligand. The angle made between the equatorial planes varies from 12.14(2)° for **3** to 36.61(5)° for **5**. The variation in this angle is consistent with two main factors: the identity of the bridging ligands, and Jahn-Teller distortion. Because of the short interatomic distance between the nitrogen atoms of the 1,8-naphthyridine fragment (2.298(16) Å), the optimal M–X bond length for an idealized octahedral geometry is ~1.62 Å. Since the M–Cl bonds at 2.36(5) Å are relatively long compared to the M–OH and $M–OH_2$ bonds, the chloride bridging ligands in **2** and **5** enforce greater angles between the equatorial planes, 26.68(8)° and 36.61(5)°, respectively, than for the hydroxo- or aqua-bridged analogs of the same metal – 12.14(2)° for **3** and 25.64(5)° for **6**. The other factor, Jahn-Teller distortion, results in long M–N(naphthyridine) bonds (*vide supra*), which push the metal centers out of the "pocket" of the ligand, and enforce tilted MN_2X_2 equatorial planes to maintain an octahedral geometry about the metal centers. Thus, the largest angle of 36.61(5)° occurs for the d^9-copper complex **5** having the largest Jahn-Teller distortion, followed by the moderately Jahn-Teller distorted d^7-cobalt complex **2** with an angle of 26.68(8)°, and the non-distorted d^8-nickel complex **4** with an angle of 25.57(7)°. Finally, the smallest angle of 12.14(2)° occurs for the Co(III) complex **3**, consistent with the small ionic radius of the Co(III) ion, which allows the metal centers to better fit into the ligand "pocket."

Magnetic Measurements. The magnetic moments of complexes **1**-**6** (Table 2) were measured by the Evans method.[27] With the exception of **3**, the only complex not containing M(II) metal centers, the magnetic moment of each complex is consistent with the spin state expected for high-spin M(II) metal centers. The magnetic moment of the mononuclear d^5 manganese complex **1** is 5.8(2) μ_B, consistent with a high-spin S = 5/2 Mn(II) center. The d^7 cobalt complex **2,** exhibits a magnetic moment of 4.8(2) μ_B per metal center, a deviation from the spin-only S = 3/2 value of 3.87 μ_B typical for high-spin octahedral Co(II) complexes.[28] The

magnetic moment of the d^8 nickel complex **4**, μ_{eff} = 3.04(10) μ_B per nickel center, is slightly higher than the spin-only S = 1 value (2.83 μ_B), as is usually observed for Ni(II) centers.[28] Similarly, for the d^9 copper complexes, the magnetic moments of 1.61(5) μ_B (**5**) and 1.67(5) μ_B (**6**) per copper center are lower than the spin-only value of 1.73 μ_B, and also lower than the typically observed magnetic moment for mononuclear Cu(II) centers. However, this behavior is consistent with what has been reported for multinuclear copper complexes and is presumably due to ligand-mediated magnetic exchange between the copper centers.[28] In contrast to the M(II) complexes, the Co(III) complex **3** adopts a low-spin, d^6 electronic configuration and is diamagnetic.

Table 2. Physical Properties of complexes **1-6**

		magnetic moment (μ_B)	d-d transition (nm ($M^{-1}cm^{-1}$))	
1	$[Mn(DPFN)_2]^{2+}$	5.85(16)		
2	$Co_2(\mu\text{-}Cl)_2$	4.84(16)	512 (83(5))	485 (88(5))
3	$Co_2(\mu\text{-}OH)_2$	diamagnetic	522 (300(10))	362 (sh)[a]
4	$Ni_2(\mu\text{-}Cl)_2$	3.04(10)	625 (11.6(4))	
5	$[Cu_2(\mu\text{-}Cl)_2]_2$	1.61(5)	702 (180(10))	431 (170(10))
6	$Cu_2(\mu\text{-}OH)(\mu\text{-}OH_2)$	1.67(5)	599 (52(3))	

[a] sh = shoulder

Electronic Spectra. Electronic spectra of DPFN and complexes **1-6** were recorded in acetonitrile (DPFN), methanol (**1,2,4,5**), or aqueous (**3**,**6**) solution. These spectra are shown in Figure 4 and selected absorption peaks are given in Table 2. Each complex exhibits intense electronic transitions in the UV region below ~350 nm with high molar absorptivities (ε > 10,000 $M^{-1}cm^{-1}$) composed of one absorption band in the region 308-321 nm, and additional transitions at 255-262 nm and 212-214 nm that not observed in some complexes. These transitions correspond to those observed in DPFN and are assigned to π-π^* transitions of the DPFN ligand.

Absorptions corresponding to *d-d* transitions are observed in each metal complex, with the exception of **1**. As is common for high-spin d^5 centers, the *d-d* transitions for the d^5 manganese complex **1** are too weak to be observed. The observed bright yellow color of the compound is attributed to broadening of the absorbance peak of the π-π^* transition at 321 nm, and may arise from unresolved charge transfer bands below 450 nm.

Unlike the other metal complexes, the green crystals of d^7 cobalt complex **2** change color when dissolved in methanol, to give a red solution. This color change can be attributed to reaction of the $CoCl_4^{2-}$ counterion with the water present in solution to form the $Co(H_2O)_6^{2+}$ ion. Whereas the $CoCl_4^{2-}$ ion has a complicated set of absorbance peaks in the region 593-693 nm with ε = 122-653 $M^{-1}cm^{-1}$, the $Co(H_2O)_6^{2+}$ ion has only a very weak absorption (ε = 4.8 $M^{-1}cm^{-1}$) at 513 nm which corresponds well with the observed absorption at 512 nm.[29]

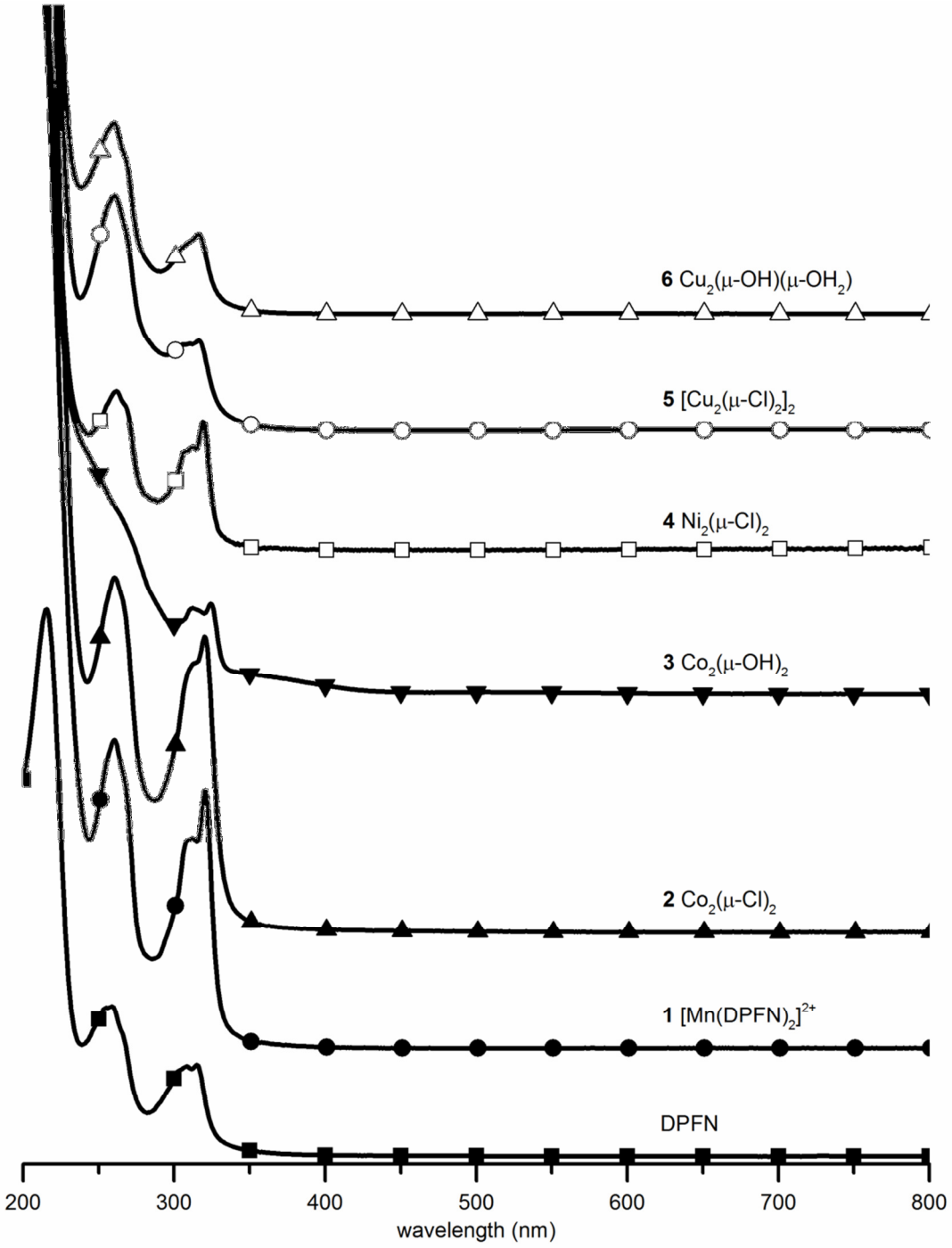

continued on next page

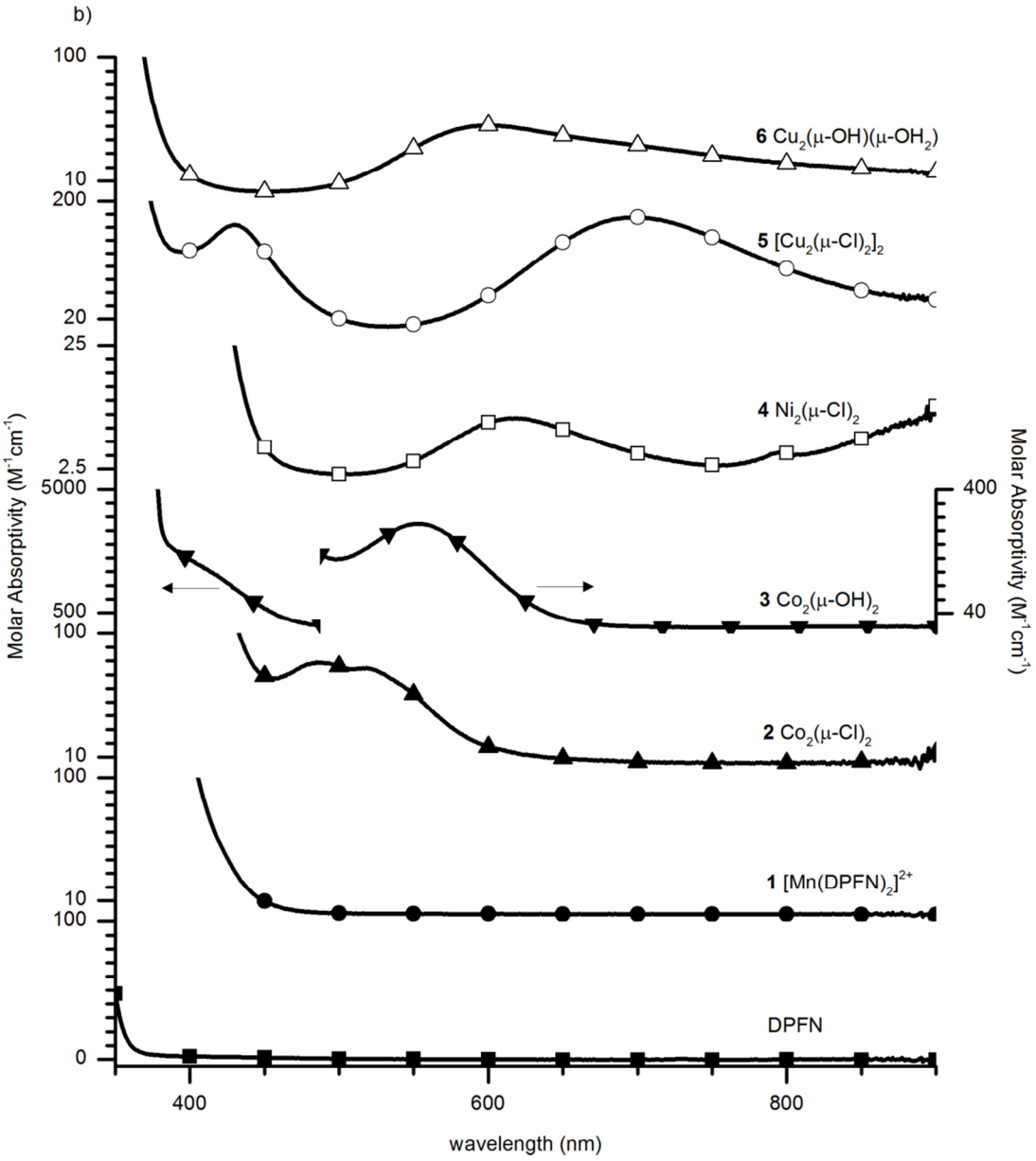

Figure 4. Electronic spectra of DPFN (■), **1** (●), **2**, (▲), **3** (▼), **4** (□), **5** (○), and **6** (△). a) Spectral region from 200–450 nm displaying molar absorptivity up to 35,000 $M^{-1}cm^{-1}$ for DPFN, and **3**-**6** and up to 75,000 $M^{-1}cm^{-1}$ for **1** and **2**. b) Spectral region from 350–900 nm displaying molar absorptivity up to 25 $M^{-1}cm^{-1}$ for **4**, up to 100 $M^{-1}cm^{-1}$ for DPFN, **1**, **2**, **5**, and **6**, 200 $M^{-1}cm^{-1}$ for **5**, and 5000 $M^{-1}cm^{-1}$ for **3**.

The d^6 cobalt complex **3** has one well-defined *d-d* transition at 522 nm, as expected for six-coordinate, pseudo-octahedral, low-spin d^6-cobalt complexes, corresponding to the $^1A_{1g} \rightarrow {}^1T_{1g}$ transition in pure O_h symmetry. The higher energy $^1A_{1g} \rightarrow {}^1T_{2g}$ transition occurs in a region partially obscured by the π-π^* transitions of the DPFN ligand in **3**; however, a shoulder at 362 nm may be assigned to this *d-d* transition. From the energies of these two transitions, an approximate average crystal field splitting parameter of Δ = 21,000 cm^{-1} can be obtained using

the Tanabe-Sugano diagram (C/B = 4.42) for d^6 ions. This splitting energy is between the value for $Co(H_2O)_6^{3+}$ (20,760 cm^{-1}) and $Co(NH_3)_6^{3+}$ (22,870 cm^{-1}), which is expected given the mixture of aqua, hydroxo, and pyridine-type ligands in **3**, and suggests that the field strength of the DPFN ligand is approximately similar to that of pyridine.[30]

The d^8 nickel complex **4** exhibits one weak (ε = 11.6(4) $M^{-1}cm^{-1}$) transition at 625 nm consistent with the intermediate energy, spin-allowed *d-d* transition for a six coordinate pseudo-octahedral complex. The other two expected transitions are not observed; however, the tail of the low energy transition absorption band is apparent at 800-900 nm at the low energy limit of the spectrum. The expected high-energy transition is obscured by the π-π^* transitions of DPFN, but a slight shoulder around 375 nm is evident.

The d^9 copper complexes **5** and **6** are subject to strong Jahn-Teller distortions which are evident in the electronic spectra of these complexes. For the $Cu_2(\mu\text{-}OH)(\mu\text{-}OH_2)$ complex **6**, the Jahn-Teller effect is manifested in the very broad character of the *d-d* transition with λ_{max} = 599 nm. In **5**, the Jahn-Teller effect is large enough to result in two strongly blue-shifted, distinct absorptions corresponding to a low energy $d_{z^2} \rightarrow d_{xy}$ transition at 702 nm and a high energy $d_{x^2-y^2}$, d_{xz}, $d_{yz} \rightarrow d_{xy}$ transition at 431 nm (axes are defined as shown in Figure 4). The absorption peak at 431 nm is unusually high in energy for a *d-d* transition in a Cu(II) complex but is too weak (ε = 170(10) $M^{-1}cm^{-1}$) to correspond to a charge transfer band.

Electrochemical Experiments. Cyclic voltammetry traces of DPFN and compounds **1**-**6** were recorded in 0.1 M $^tBu_4NPF_6$ DMF with a glassy carbon electrode using a $Ag/AgNO_3$ reference electrode in acetonitrile. The CV traces shown in Figure 5 are referenced to Fc/Fc^+ (0.076 V *vs.* Ag/NO_3 in acetonitrile). Due to insolubility of **3** in 0.1 M $^tBu_4NPF_6$ DMF solution, two equivalents of 1 M KOH aqueous solution were added to solubilize the complex.

The cyclic voltammetry of DPFN in Figure 5a shows that the compound is anodically stable in DMF and cathodically stable to −1.8 V after which DPFN is irreversibly reduced at a peak anodic current of −1970 mV, assigned to reduction of the naphthyridine moiety. Two additional, significant reduction events occur at −2665 mV and −2777 mV are assigned to reduction of the pendant pyridine rings (for pyridine $E_{1/2}$ = −2.66 V *vs.* SCE in 0.1 M Et_4NI DMF[31]). In **1**-**6**, additional oxidation and reduction events are assigned to redox events at the metal centers. In the mononuclear manganese complex **1**, irreversible reduction of the manganese center is observed at −1656 mV for Mn^{II} to Mn^{I}, followed by reduction from Mn^{I} to Mn^0 at −1759 mV. No oxidation of Mn^{II} to Mn^{III} is observed below 1.2 V.

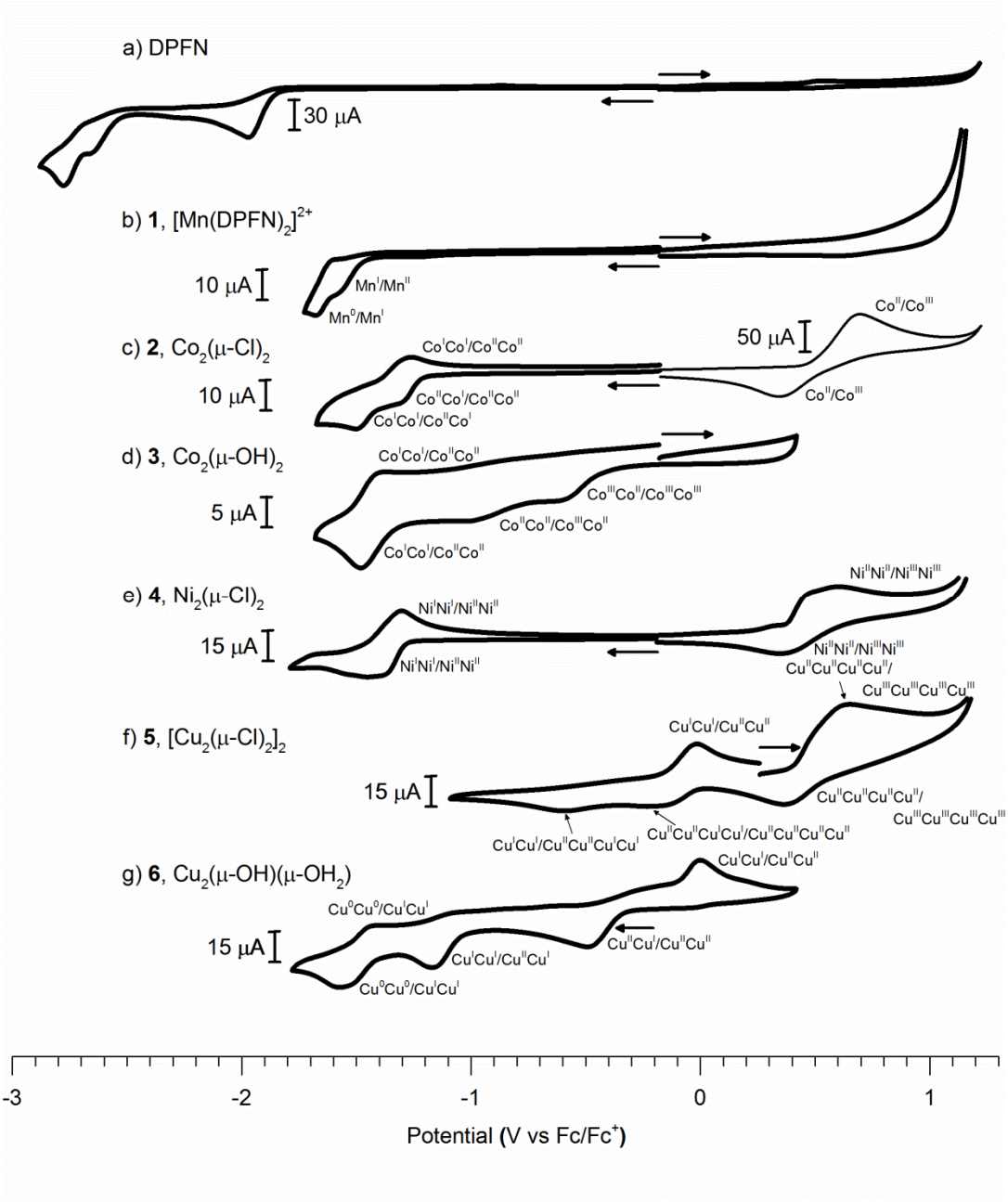

Figure 5. Cyclic voltammograms of 2 mM DMF solutions of a) DPFN, b) **1**, c) **2**, d) **3**, e) **4**, f) **5**, g) **6**. Voltammograms are shown on a common potential scale referenced to Fc/Fc^{+}. The direction of the initial scanning potential for each experiment is indicated by an arrow. For DPFN and **1**, two separate cyclic voltammograms for anodic and cathodic potentials are given. For **2**, anodic potentials are scaled to 50 μA while cathodic potentials are scaled to 10 μA.

For the series of chloride-bridged complexes **2**, **4**, and **5**, analogous oxidation and reduction events are observed. In each case the redox events are irreversible, likely due to structural changes occurring in the complex. For the dinickel complex **4**, reduction to the $Ni^{I}Ni^{I}$ species is observed as one broad reduction event with a cathodic current peak at −1449 mV, associated with a corresponding reoxidation at −1302 mV. Oxidation of **4** to the $Ni^{III}Ni^{III}$ species is observed as a broad oxidation step with an anodic peak at 599 mV, associated with re-reduction at 349 mV. Reduction of the tetranuclear copper complex **5** is similar to **4**, however due to the four copper centers, reduction occurs in two two-electron events at −235 mV, presumably to produce a $Cu^{I}Cu^{I}Cu^{II}Cu^{II}$ species, and at −592 mV, after which the species decomposes into dinuclear $Cu^{I}Cu^{I}$ units. Re-oxidation of the $Cu^{I}Cu^{I}$ to $Cu^{II}Cu^{II}$ species occur together at −15 mV. Oxidation of the complex by four electrons occurs in two unresolved irreversible steps with an anodic peak at 645 mV and a cathodic peak at 365 mV. In the cobalt complex **2,** reduction to the $Co^{I}Co^{I}$ species is observed in two irreversible steps with cathodic current peaks at −1298 mV and −1500 mV. Anodic oxidation of the $Co^{II}Co^{I}$ step is observed at −1263 mV (i_{pa}/i_{pc} = 0.3). Scanning to anodic potentials with **3** results in one high current redox event with $E_{1/2}$ = 518 mV attributed to oxidation of the $CoCl_4^{2-}$ anion. Oxidation of the $Co^{II}Co^{II}$ cation is not observed but may be obscured by the oxidation of $CoCl_4^{2-}$.

The hydroxo- and aqua-bridged complexes **3** and **6** show significantly different electrochemical properties as compared to the related chloride-bridged complexes. The hydroxide-bridged cobalt complex **3** is strongly stabilized in the $Co^{III}Co^{III}$ oxidation state, with respect to the chloride-bridged cobalt complex **2**. The $Co^{III}Co^{III}$ state is not observed for **2**, although due to the obscuring presence of $CoCl_4^{2-}$ its formation could occur above a potential as low as 524 mV. Reduction of the $Co^{III}Co^{III}$ state of **3** occurs in two separate steps to form the $Co^{III}Co^{II}$ state at −619 mV and the $Co^{II}Co^{II}$ state at −985 mV. These reduction steps are completely irreversible, probably due to major structural changes that occur on reduction to the labile Co(II) oxidation state. Further reduction of the complex to a $Co^{I}Co^{I}$ species occurs with cathodic current peaks at −1481 mV, with re-oxidation at −1375 mV. The similarity of the reduction potential for this species and that for generation of the $Co^{I}Co^{I}$ state in **2** (−1500 mV) indicates that reduction of **3** to the $Co^{II}Co^{II}$ state induces reactions that result in a complex similar to that of **2** in 0.1 M $^{t}Bu_4NPF_6$ DMF solution. Oxidation of **3** to $Co^{IV}Co^{III}$ or $Co^{IV}Co^{IV}$ species is not observed to 1.2 V.

The hydroxo- and aqua-bridged copper complex **6** exhibits significant stabilization of the $Cu^{II}Cu^{II}$ state compared to the $Cu^{II}Cu^{II}$ state in the chloride-bridged complex **5**. While the $Cu^{II}Cu^{II}$ state of **5** is oxidized to $Cu^{III}Cu^{III}$ at 738 mV, oxidation of **6** is not observed up to 1.2 V. Also, while the reduction of **5** to $Cu^{I}Cu^{I}$ occurs in two steps at −223 mV and −580 mV, the reduction of **6** to $Cu^{I}Cu^{I}$ occurs in two steps with cathodic current peaks at −491 mV and −1170 mV indicating a much more stable $Cu^{II}Cu^{I}$ mixed-valence state, as well as a stabilized $Cu^{II}Cu^{II}$ state (with respect to **5**). Re-oxidation to $Cu^{II}Cu^{II}$ occurs with an anodic current peak at −3 mV. In addition to reduction to the $Cu^{I}Cu^{I}$ state for **5**, further irreversible reduction to Cu^{0} occurs with a cathodic current peak at −1573 mV with partial re-oxidation (i_{pa}/i_{pc} = 0.2) occurring at an anodic current peak at −1406 mV.

Acid Dissociation Constants of 3 and 6. The hydroxo- and aqua-bridged complexes **3** and **6** contain terminal or bridging aqua ligands that should exhibit acidic properties. The acid dissociation constants for these complexes were determined by potentiometric titration of aqueous solutions of **3** or **6** using a 0.1 M NaOH solution (Figure 6). For the cobalt complex **3**, two terminal aqua ligands could be deprotonated, with acid dissociation constants measured from

the half-equivalence points as pK_{a1} = 4.1(1) and pK_{a2} = 5.8(1). In the copper complex **6**, the bridging aqua ligand is deprotonated with an acid dissociation constant of pK_a = 3.3(1).

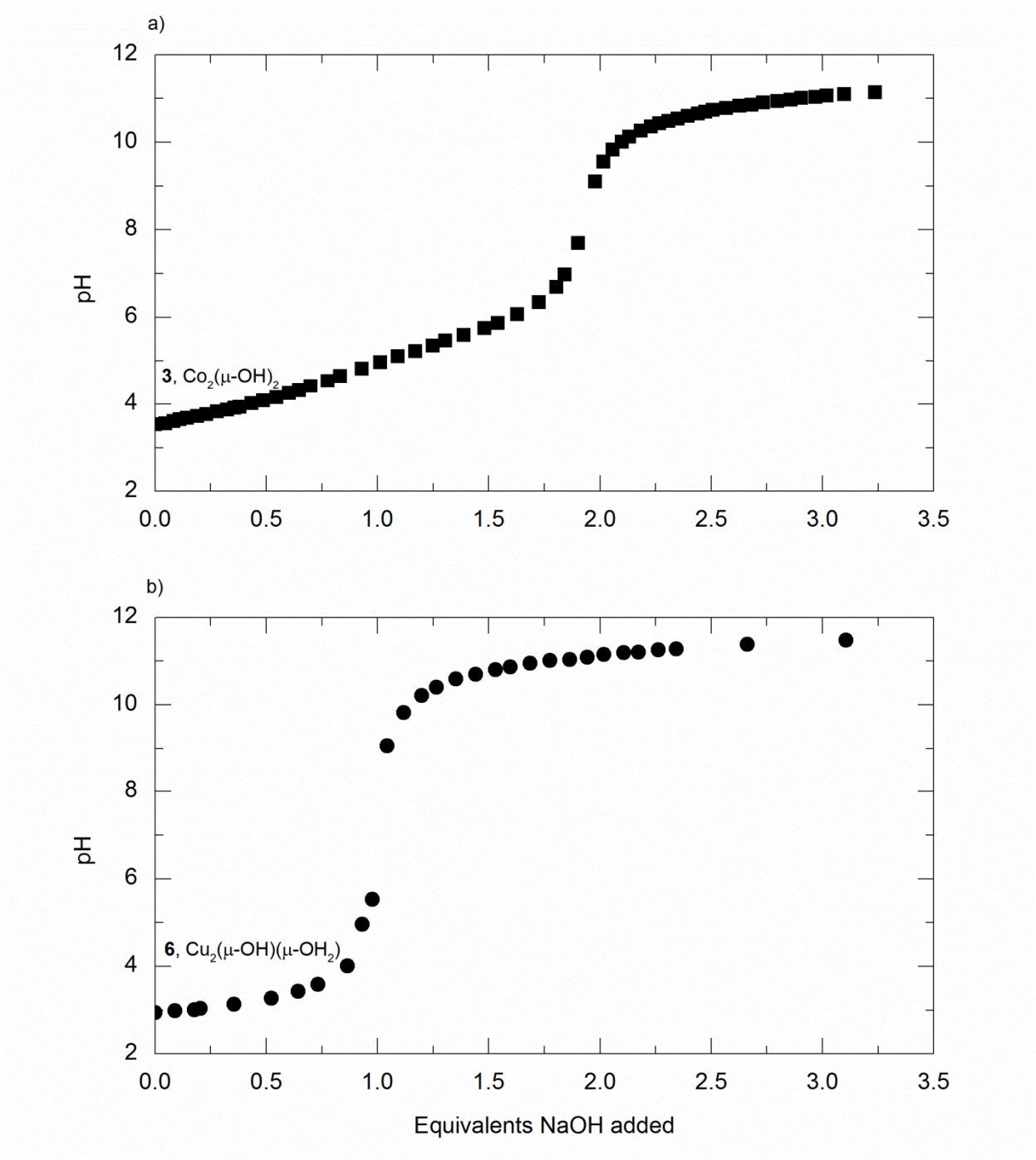

Figure 6. Potentiometric titration curves of **3** (■), and **6** (●). Base was added as aliquots of a 0.1 M NaOH solution.

Discussion

This work has produced a range of first-row transition metal dinuclear and tetranuclear complexes formed by the naphthyridine-based dinucleating ligand DPFN. Comparisons of DPFN can be made with the well-known pentadentate ligand Py5, and the analogous phthalazine-based dinucleating ligand bdptz, which have similarly been used to form a series of first-row transition metal complexes (Figure 7).[32–34] DPFN can be regarded as the dinucleating analog of Py5. Like Py5, stable complexes with DPFN tend to contain metals in the 2+ oxidation state having a high-spin electronic configuration. A comparison of chloride complexes of the DPFN and Py5 (R = OMe) ligands shows that M–N(pyridyl) distances are slightly shorter for the DPFN complexes, by an average of 0.07(6) Å. In addition, the M–N(naphthyridine) distances in DPFN complexes are on average 0.15(5) Å longer than the M–N bond distance associated with the axial pyridine of Py5 complexes. This may reflect the operation of strain, induced by the placement two metal centers in the binding pocket of DPFN. Comparison of the electrochemical properties of DPFN and Py5 complexes shows that DPFN complexes tend to exhibit irreversible oxidation or reduction events, while Py5 complexes often display reversible redox events. This is likely due to the greater flexibility of the ligand pocket of DPFN versus Py5, allowing for significant structural

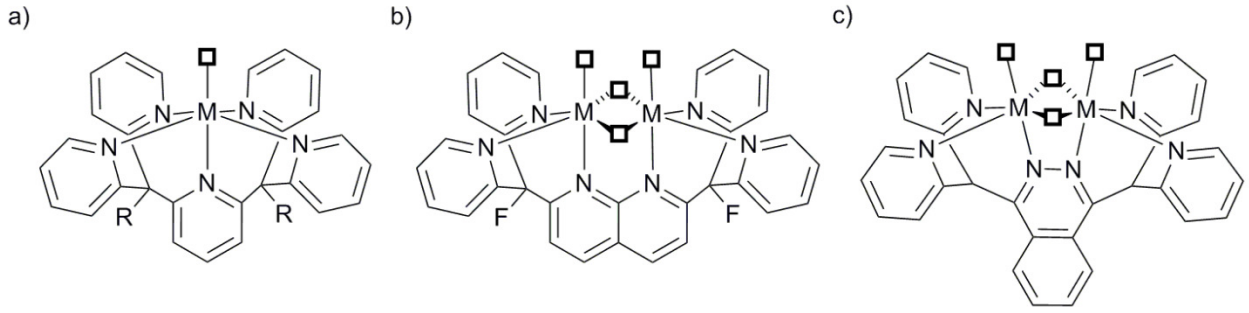

Figure 7. Comparison of the coordination modes of a) Py5, b) DPFN, and c) bdptz.

changes during redox events. Also, this may be indicative of greater instability of DPFN complexes due to tridentate binding to each metal center instead of pentadentate binding as exhibited by Py5.

The electrochemical properties of the nickel chloride complexes of DPFN and Py5 are the most directly comparable due to the presence of multiple, analogous redox events. In the [(Py5)NiCl][Cl] complex, oxidation to Ni^{III} occurs at $E_{1/2}$ = 0.39 V (*vs.* Fc/Fc^{+}) while reduction to Ni^{I} occurs as $E_{1/2}$ = −1.91 V. In the dinickel complex **4**, oxidation to the $Ni^{III}Ni^{III}$ state is observed at $E_{1/2}$ = 0.47 V and reduction to the $Ni^{I}Ni^{I}$ state occurs at $E_{1/2}$ = −1.38 V. The shift of the oxidation and reduction events to more positive potentials in **4** is likely due to the presence of three chloride ligands and only three nitrogen donors for each metal center instead of a single chloride and five nitrogen donors in [(Py5)NiCl][Cl]. However, at only slightly more positive oxidative potentials, **4** is oxidized by two rather than one electron, demonstrating the ability of dinuclear DPFN complexes to store multiple redox equivalents at a lower required potential.

Comparisons can also be made to the similar dinucleating ligand bdptz.[33,34] The ligand bdptz forms related chloride- and hydroxide-bridged complexes, and due to the coordination geometry of the phthalazine nitrogen atoms, the range of M–M distances supported in complexes

with bdptz have a greater range of values (3.754 – 3.121 Å) compared to complexes of DPFN (2.7826(5) – 3.2410(11) Å). This ability to support long metal-metal distances may explain why bdptz easily forms chloro-bridged dimanganese(II) complexes with an M–M distance of 3.549(2) Å, while DPFN appears to be more resistant toward formation of complexes with higher ionic radii.

Conclusion

This work illustrates the dinucleating ability of the naphthyridine-based dinucleating ligand DPFN. Dinuclear and tetranuclear metal complexes were formed with late first-row transition metals in which the two metal centers are held at separations of 2.7826(5) – 3.2410(11) Å. The structural properties of DPFN are conducive to formation of pseudo-octahedral metal centers with two one-atom bridging ligands to give "diamond-shaped" dinuclear complexes.

Experimental

General Considerations. Spectroscopic grade solvents were purchased from Aldrich and distilled water was employed. Deuterated solvents were purchased from Cambridge Isotope Laboratories and used as received. The ligand DPFN was prepared as described previously.[26] NMR spectra were recorded on a Bruker AV-600 spectrometer at 20 °C. ^{1}H NMR spectra were referenced to residual protio solvent peaks (δ 4.80 for d_2-water, δ 4.78 for d_4-methanol). Solution magnetic susceptibilities were determined by the Evans' method.[27] Solution UV-Vis spectra were collected using a Cary 300 Bio spectrophotometer with a 1-cm quartz cell at 1 nm resolution. Infrared spectra were recorded on powders with a Thermo Scientific Nicolet iS10 using the Smart iTR ATR sampling accessory. Potentiometric titrations were performed using a Thermo Fisher Orion 3-Star pH meter with a Ag/AgCl combination pH electrode. Measurement of acid dissociation constants were not corrected for ionic strength. Elemental analyses were carried out by the College of Chemistry Microanalytical Laboratory at the University of California, Berkeley.

Electrochemical Measurements. Electrochemical experiments were recorded with a BASi Epsilon potentiostat using a 3 mm diameter glassy carbon working electrode, a Pt wire counter electrode and a Ag/$AgNO_3$ reference electrode (0.1 M [^{t}Bu$_4$N][PF_6], 1 mM $AgNO_3$ in ACN, 0.076 V *vs.* Fc/Fc$^+$). The glassy carbon working electrode was polished between runs with 0.05 μm alumina slurry, rinsed with water and dried. Cyclic voltammograms were recorded in 0.1 M DMF [^{t}Bu$_4$N][PF_6] solutions. Solutions were purged with nitrogen before analysis.

Synthesis of [Mn(DPFN)$_2$][NO$_3$]$_2$·5CH$_3$OH (1). DPFN (0.2 g, 0.4 mmol) was dissolved in 25 mL of MeOH and then $Mn(NO_3)_2{\cdot}4H_2O$ (0.05 g, 0.2 mmol) was added. The resulting yellow solution was stirred for 16 h. The volume of the solution was reduced to ~5 mL and the product was crystallized from solution by vapor diffusion of THF to afford yellow X-ray quality crystals (0.25 g, 0.18 mmol, 93%). **Magnetic Moment** (Evans'): μ_{eff} = 5.9(2)μ_B. **UV-Vis** (MeOH, λ [nm] (ε [$M^{-1}{\cdot}cm^{-1}{\cdot}10^{-3}$])): 260 (40(3)), 321 (33(2)), 312 (27(2)). **IR** (ATR, $\bar{\nu}$ [cm^{-1}]): 1598(m), 1504(w), 1469(m), 1434(m), 1338(s), 1301(w), 1214(w), 1136(m), 1101(w), 1084(w), 1055(w), 1015(m), 995(w), 933(w), 901(w), 859(m), 830(w), 775(s), 749(m), 714(w), 700(w), 689(s), 641(w), 617(w), 593(w), 559(w), 543(w). **EA** Anal. Calcd (%) for $C_{65}H_{60}F_4MnN_{14}O_{11}$ (1344.21 g/mol): C, 58.08; H, 4.50; N, 14.59. Found: C, 58.07; H, 4.12; N, 14.97.

Synthesis of $[Co_2(\mu\text{-}Cl)_2Cl(CH_3OH)(DPFN)]_2[CoCl_4]\cdot 8H_2O$ (2). Under a flow of nitrogen, DPFN (0.1 g, 0.2 mmol) was dissolved with heating in 75 mL of EtOH and then a solution of anhydrous $CoCl_2$ (0.05 g, 0.4 mmol) in 10 mL of EtOH was added. The resulting pale orange solution was stirred for 16 h slowly turning brown in color. The volume of the solution was reduced to ~5 mL, and this solution was allowed to stand at room temperature for 10 min, after which green crystals of the product formed. The product was recrystallized by vapor diffusion of Et_2O into a MeOH solution to form green X-ray quality crystals (0.06 g, 0.03 mmol, 38%). **Magnetic Moment** (Evans'): $\mu_{eff} = 11.1(5)\mu_B$. **UV-Vis** (MeOH, λ [nm] (ε [$M^{-1}\cdot cm^{-1}\cdot 10^{-3}$])): 212 (160(10)), 261 (47(3)), 320 (38(2)), 485 (0.088(5)), 512 (0.083(5)). **IR** (ATR, $\bar{\nu}$ [cm^{-1}]): 1618(w), 1600(m), 1537(w), 1511(w), 1472(m), 1438(m), 1391(w), 1296(w), 1195)w), 1160(w), 1486(w), 1104(w), 1083(m), 1060(w), 1024(m), 929(w), 856(m), 808(w), 774(s), 713(w), 702(w), 687(m), 642(w), 614(w), 577(w). **EA** Anal. Calcd (%) for $C_{62}H_{64}Cl_{10}Co_5F_4N_{12}O_{10}$ (1862.45 g/mol): C, 39.76; H, 3.20; N, 9.02. Found: C, 39.98; H, 3.46; N, 9.02.

Synthesis of $[Ni_2(\mu\text{-}Cl)_2Cl(CH_3OH)(DPFN)][Cl]\cdot 4H_2O$ (4). Under a flow of nitrogen, DPFN (0.1 g, 0.2 mmol) was dissolved with heating in 75 mL of EtOH and then a solution of anhydrous $NiCl_2$ (0.05 g, 0.4 mmol) in 10 mL of EtOH was added. The resulting green solution was stirred for 16 h. The solvent was removed by rotovap to give the product as a green precipitate. The product was crystallized by vapor diffusion of Et_2O into a MeOH solution to form green X-ray quality crystals (0.10 g, 0.12 mmol, 58). **Magnetic Moment** (Evans'): $\mu_{eff} = 4.3(2)\mu_B$. **UV-Vis** (MeOH, λ [nm] (ε [$M^{-1}\cdot cm^{-1}\cdot 10^{-3}$])): 262 (20.0(8)), 313 (14.1(5)), 320 (16.7(6)), 625 (0.0116(4)). **IR** (ATR, $\bar{\nu}$ [cm^{-1}]): 1602(m), 1578(w), 1541(w), 1512(w), 1471(m), 1441(m), 1395(w), 1296(w), 1239(w), 1196(w), 1161(w), 1142(w), 1086(m), 1061(w), 1026(m), 931(w), 853(m), 772(s), 714(w), 702(w), 686(s), 643(w), 615(w), 576(w), 551(w). **EA** Anal. Calcd (%) for $C_{31}H_{32}Cl_4F_2N_6Ni_2O_5$ (865.86 g/mol): C, 42.88; H, 3.46; N, 9.84. Found: C, 43.00; H, 3.73; N, 9.71.

Synthesis of $[Cu_4(\mu\text{-}Cl)_6(DPFN)_2]Cl_2\cdot 6H_2O$ (5). Under a flow of nitrogen, DPFN (0.1 g, 0.2 mmol) was dissolved with heating in 75 mL of EtOH, and to this solution was added a solution of anhydrous $CuCl_2$ (0.05 g, 0.4 mmol) in 10 mL of EtOH. The resulting bright green solution was stirred for 16 h. The volume of the solution was reduced to ~5 mL, filtered, and crystallized by vapor diffusion of Et_2O into a EtOH solution to form green X-ray quality crystals (0.16 g, 0.19 mmol, 97%). **Magnetic Moment** (Evans'): $\mu_{eff} = 2.27(7)\mu_B$. **UV-Vis** (MeOH, λ [nm] (ε [$M^{-1}\cdot cm^{-1}\cdot 10^{-3}$])): 212 (150(11)), 261 (60(4)), 305 (23(2)), 310 (23(2)), 316 (23(2)), 431 (0.17(1)), 702 (0.18(1)). **IR** (ATR, $\bar{\nu}$[cm^{-1}]): 1603(m), 1578(w), 1544(w), 1502(w), 1471(m), 1436(m), 1296(w), 1246(w), 1196(w), 1162(w), 1140(w), 1083(m), 1064(w), 1026(m), 862(m), 811(w), 778(s), 712(w), 699(w), 686(m), 650(w), 618(w), 570(w). **EA** Anal. Calcd (%) for $C_{60}H_{52}Cl_8Cu_4F_4N_{12}O_6$ (1650.94 g/mol): C, 43.74; H, 3.00; N, 10.13. Found: C, 43.65; H, 3.17; N, 10.18.

Synthesis of $[Cu_2(\mu\text{-}OH)_2(NO_3)(OH_2)(DPFN)]\cdot 2H_2O$ (6). DPFN (0.2 g, 0.4 mmol) was dissolved with heating in 20 mL of MeOH to which was added a solution of $Cu(NO_3)_2\cdot 2.5H_2O$ (0.19 g, 0.8 mmol) in 10 mL of MeOH and 2 mL of H_2O. The resulting blue solution was stirred for 30 min. The solvent was removed by rotovap to give the product as a blue precipitate. The product was dissolved in ~3 mL of hot water and crystallized by slow evaporation to give blue X-ray quality crystals (0.25 g, 0.28 mmol, 70%). **Magnetic Moment** (Evans'): $\mu_{eff} = 2.38(8)\mu_B$. **UV-Vis** (water, λ [nm] (ε [$M^{-1}\cdot cm^{-1}\cdot 10^{-3}$])): 260 (25(1)), 316 (10.4(5)), 599 (0.052(3)). **IR** (ATR, $\bar{\nu}$ [cm^{-1}]): 1606(m), 1578(w), 1474(w), 1444(w), 1401(s), 1321(s), 1299(s), 1194(w), 1163(w), 1132(w), 1086(m), 1030(m), 1002(w), 930(w), 868(m), 827(w), 811(w), 775(s), 713(w), 699(w),

688(m), 655(w), 620(w), 572(w), 557(w), 539(w). **EA** Anal. Calcd (%) for $C_{30}H_{29}Cu_2F_2N_9O_{14}$ (904.70 g/mol): C, 39.94; H, 3.19; N, 13.81. Found: C, 39.83; H, 3.23; N, 13.93.

Crystallographic Analyses. X-ray diffraction data were collected for compounds **1**-**5** using Bruker AXS three-circle diffractometers coupled to a CCD detector with graphite or QUAZAR multilayer mirror monochromated Mo Kα (λ = 0.71073 Å) radiation cooled under a stream of N_2 to 100 K. Raw data were integrated and corrected for Lorentz and polarization effects using Bruker APEX2 v. 2009.1. Absorption corrections were applied using SADABS. The structures were solved by direct methods using SHELXS and refined against F^2 on all data by full-matrix least squares with SHELXL-97. Refinement details for each compounds are detailed below:

$[Mn(DPFN)_2][NO_3]_2 \cdot 0.5CH_3OH \cdot 1.5THF$ (**1**)

All non-hydrogen atoms were refined anisotropically; hydrogen atoms were included into the model at their geometrically calculated positions and refined using a riding model. Disorder of one tetrahydrofuran solvate molecule was modeled over two sites with the use of free variables. Solvent disorder of a second solvate site consisting of 50:50 tetrahydrofuran:methanol was extensive and was treated as a diffuse contribution to the overall scattering without specific atom positions by SQUEEZE/PLATON.

$[Co_2(\mu\text{-}Cl)_2Cl(CH_3OH)(DPFN)]_2[CoCl_4] \cdot 3.75CH_3OH \cdot 0.5THF$ (**2**)

All non-hydrogen atoms were refined anisotropically except for a $CoCl_4^{2-}$ chloride atom and the atoms of a methanol molecule that had very low structural occupancy factors; hydrogen atoms were included into the model at their geometrically calculated positions and refined using a riding model except the OH hydrogen atoms of the coordinated methanol ligands which were located from the electron difference map and the OH bond lengths were restrained to chemically appropriate values. Disorder of the $CoCl_4^{2-}$ was modeled as partial occupancies over three sites. Methanol and the diethyl ether solvate molecules were modeled with partial occupancies appropriate to the electron density. Due to disorder of the diethyl ether solvate molecule bond and angle restraints at chemically appropriate values were applied and isotrotrpic restraints were applied to atoms with severe anisotropy.

$[Ni_2(\mu\text{-}Cl)_2Cl(CH_3OH)(DPFN)][Cl] \cdot 3.25CH_3OH$ (**4**)

All non-hydrogen atoms were refined anisotropically; hydrogen atoms were included into the model at their geometrically calculated positions and refined using a riding model except the OH hydrogen atom of one coordinated methanol ligand which was located from the electron difference map and the OH bond length restrained to a chemically appropriate value. Significant disorder in the other coordinated methanol ligand prevented location of the OH hydrogen atom and the carbon atom was treated with a tight isotropic restraint. One chloride anion was disordered and modeled over two sites with the use of free variables. Extensive disorder of the methanol solvate molecules consisting of 13 methanol molecules could not be and was treated as a diffuse contribution to the overall scattering without specific atom positions by SQUEEZE/PLATON.

$[Cu_4(\mu\text{-}Cl)_6(DPFN)_2][Cl]_2 \cdot 2CH_3OH \cdot 2THF$ (**5**)

All non-hydrogen atoms were refined anisotropically; hydrogen atoms were included into the model at their geometrically calculated positions and refined using a riding model. The methanol solvate molecule sites were modeled as partially occupied and treated with isotropic restraints.

The tetrahydrofuran molecule site was centered on a two-fold axis and one atom site was modeled as a 50:50 mixture of oxygen and carbon.

$[Cu_2(\mu\text{-}OH)_2(NO_3)(OH_2)(DPFN)]\cdot 2H_2O$ (**6**)
All non-hydrogen atoms were refined anisotropically; hydrogen atoms were included into the model at their geometrically calculated positions and refined using a riding model except for hydrogen atoms of solvate water molecules and coordinated aquo or hydroxo ligands which were located from the electron difference map.

Table 3.Experimental details for the X-ray crystal structures of **1**, **2**, **4**, **5**, **6**.

	1	**2**	**4**	**5**	**6**
Chemical formula	$C_{66.5}H_{54}F_4MnN_{14}O_8$	$C_{33.875}H_{34}Cl_5Co_{2.5}F_2N_6O_{3.125}$	$C_{34.25}H_{37}Cl_4F_2N_6Ni_2O_{4.25}$	$C_{70}H_{64}Cl_8Cu_4F_4N_{12}O_4$	$C_{30}H_{29}Cu_2F_2N_9O_{14}$
Formula Mass	1308.17	937.75	897.89	1751.15	904.70
Crystal system	Monoclinic	Triclinic	Triclinic	Orthorhombic	Monoclinic
a/Å	13.4808(5)	13.6956(16)	11.8504(5)	15.1594(6)	21.1143(19)
b/Å	25.9908(10)	15.6624(18)	13.3500(6)	21.5153(8)	14.7530(13)
c/Å	17.5035(7)	21.613(3)	23.8878(10)	43.7045(17)	23.299(2)
α/°	90	82.380(1)	97.747(2)	90	90
β/°	104.029(2)	73.241(1)	93.565(2)	90	106.1750(10)
γ/°	90	64.529(1)	102.721(2)	90	90
Unit cell volume/Å^3	5949.9(4)	4007.5(8)	3636.2(3)	14254.6(10)	6970.2(11)
Temperature/K	100(2)	100(2)	100(2)	100(2)	100(2)
Space group	$P2_1/c$	$P\bar{1}$	$P\bar{1}$	*Fddd*	*C2/c*
No. of formula units per unit cell, *Z*	4	4	4	8	8
No. of independent reflections	10866	14648	13562	3262	6390
R_{int}	0.0536	0.0446	0.0399	0.0429	0.0205
Final R_1 values ($I > 2\sigma(I)$)	0.0466	0.0502	0.0598	0.0488	0.0206
Final $wR(F^2)$ values ($I > 2\sigma(I)$)	0.1163	0.1378	0.1405	0.1318	0.0549
Final R_1 values (all data)	0.0661	0.0692	0.0927	0.0754	0.0222
Final $wR(F^2)$ values (all data)	0.1248	0.1529	0.1515	0.1526	0.0558
Goodness of fit on F^2	1.116	1.057	1.097	1.066	1.053

References

(1) Gavrilova, A. L.; Bosnich, B. *Chem. Rev.* **2004**, *104*, 349–384.
(2) Stenkamp, R. E. *Chem. Rev.* **1994**, *94*, 715–726.
(3) Rosenzweig, A. C.; Frederick, C. A.; Lippard, S. J.; Nordlund, P. *Nature* **1993**, *366*, 537–543.
(4) Nordlund, P.; Sjöberg, B.-M.; Eklund, H. *Nature* **1990**, *345*, 593–598.
(5) Jabri, E.; Carr, M. B.; Hausinger, R. P.; Karplus, P. A. *Science* **1995**, *268*, 998–1004.
(6) Strater, N.; Klabunde, T.; Tucker, P.; Witzel, H.; Krebs, B. *Science* **1995**, *268*, 1489–1492.
(7) Gerdemann, C.; Eicken, C.; Krebs, B. *Acc. Chem. Res.* **2002**, *35*, 183–191.
(8) Kanyo, Z. F.; Scolnick, L. R.; Ash, D. E.; Christianson, D. W. *Nature* **1996**, *383*, 554–557.
(9) Siegbahn, P. E. M. *Acc. Chem. Res.* **2009**, *42*, 1871–1880.
(10) Gilbert, J. A.; Eggleston, D. S.; Murphy, W. R.; Geselowitz, D. A.; Gersten, S. W.; Hodgson, D. J.; Meyer, T. J. *J. Am. Chem. Soc.* **1985**, *107*, 3855–3864.
(11) Gersten, S. W.; Samuels, G. J.; Meyer, T. J. *J. Am. Chem. Soc.* **1982**, *104*, 4029–4030.
(12) Liu, F.; Concepcion, J. J.; Jurss, J. W.; Cardolaccia, T.; Templeton, J. L.; Meyer, T. J. *Inorg. Chem.* **2008**, *47*, 1727–1752.
(13) Deng, Z.; Tseng, H.-W.; Zong, R.; Wang, D.; Thummel, R. *Inorg. Chem.* **2008**, *47*, 1835–1848.
(14) Steinhagen, H.; Helmchen, G. *Angew. Chem. Int. Ed.* **1996**, *35*, 2339–2342.
(15) Klingele, J.; Dechert, S.; Meyer, F. *Coord. Chem. Rev.* **2009**, *253*, 2698–2741.
(16) Steel, P. J. *Coord. Chem. Rev.* **1990**, *106*, 227–265.
(17) Bosnich, B. *Inorg. Chem.* **1999**, *38*, 2554–2562.
(18) He, C.; Lippard, S. J. *Tetrahedron* **2000**, *56*, 8245–8252.
(19) He, C.; Lippard, S. J. *Inorg. Chem.* **2000**, *39*, 5225–5231.
(20) He, C.; Barrios, A. M.; Lee, D.; Kuzelka, J.; Davydov, R. M.; Lippard, S. J. *J. Am. Chem. Soc.* **2000**, *122*, 12683–12690.
(21) He, C.; DuBois, J. L.; Hedman, B.; Hodgson, K. O.; Lippard, S. J. *Angew. Chem. Int. Ed.* **2001**, *40*, 1484–1487.
(22) Davenport, T. C.; Tilley, T. D. *Angew. Chem. Int. Ed.* **2011**, *50*, 12205–12208.
(23) Ng, G. K.-Y.; Ziller, J. W.; Borovik, A. S. *Chem. Commun.* **2012**, *48*, 2546.
(24) Evans, O. R.; Bell, A. T.; Tilley, T. D. *J. Catal.* **2004**, *226*, 292–300.
(25) Hoppe, E.; Limberg, C.; Ziemer, B. *Inorg. Chem.* **2006**, *45*, 8308–8317.
(26) see Chapter 1.
(27) Evans, D. F. *J. Chem. Soc.* **1959**, 2003–2005.
(28) Figgis, B. N.; Lewis, J. In *Progress in Inorganic Chemistry*; Cotton, F. A., Ed.; John Wiley & Sons, Inc., 2007; pp. 37–239.
(29) Gill, N. S.; Nyholm, R. S. *J. Chem. Soc.* **1959**, 3997–4007.
(30) Lever, A. B. P. *Inorganic Electronic Spectroscopy*; 2nd ed.; Elsevier: New York, 1984.
(31) Meites, L.; Zuman, P. *CRC Handbook Series in Organic Electrochemistry*; CRC Press, 1977; Vol. 1.
(32) Klein Gebbink, R. J. M.; Jonas, R. T.; Goldsmith, C. R.; Stack, T. D. P. *Inorg. Chem.* **2002**, *41*, 4633–4641.
(33) Barrios, A. M.; Lippard, S. J. *Inorg. Chem.* **2001**, *40*, 1060–1064.
(34) Roggan, S.; Limberg, C.; Knispel, C.; Tilley, T. D. *Dalton Trans.* **2011**, *40*, 4315.

Chapter 3

Dinucleating Naphthyridine-Based Ligand for Assembly of Bridged Dicopper(I) Centers: Three-Center Two-Electron Bonding Involving an Acetonitrile Donor

Introduction

The three-center two-electron (3c-2e) bond is a well-known type of "electron-deficient" interaction that typically involves electron-poor, main-group elements such as aluminum or boron, in combination with strong σ-donor ligands such as hydride or alkyls.[1] However, 3c-2e bonds have also been observed for transition metals, for example in copper(I) aryl complexes in which the electron-deficient bond is supported by an unusually close Cu(I)–Cu(I) contact (2.37 – 2.45 Å) indicative of a cuprophilic interaction.[2] This attractive interaction between copper centers is reminiscent of the M–M interactions observed in 3c-2e bonds of main-group metals.[1] Over the past decade, similar cuprophilic interactions have been observed to result from 3c-2e bonds supported by unconventional L-type donor interactions[3] involving, for example, phosphole ligands.[4-8] The latter complexes represent rare examples of a PR_3 ligand coordinated in the μ-η^1:η^1 bridging mode.[9-13] Herein we report the formation of a dicopper complex bridged by acetonitrile in this unusual μ-η^1:η^1 mode,[14-20] whereby the bridging ligand formally contributes both electrons to the 3c-2e interaction.

The work discussed here derives from an interest in dinuclear metal complexes for cooperative substrate activations in catalytic reactions. In particular, the use of dinucleating ligands with rigid frameworks may provide well-defined pockets that promote electronic communication between the metal centers and create selective binding sites for substrates, emulating the role of the protein scaffold in enzymes.[21] For this purpose we developed a ligand system based on 1,8-naphthyridine, 2,7-bis(1,1-dipyridylethyl)-1,8-naphthyridine (DPEN). Ligands based on 1,8-napthyridine have been shown to support a variety of dinuclear metal complexes with metal- metal distances ranging from 2.5 to 4.0 Å.[22-25] The incorporation of 2,2'-dipyridylethyl groups into the 2,7-positions of 1,8-naphthyridine results in the six-donor DPEN ligand that should bind to each metal center in a tripodal manner. This binding mode leaves open coordination sites on both metals that are oriented toward one another, in a manner suitable for cooperative activation of a small molecule.

Results and Discussion

The synthesis of DPEN proceeds by lithiation of 2,2'-dipyridylethane followed by reaction with 2,7-dichloro-1,8-naphthyridine (eq. 1). Reaction of DPEN with 2 equivalents of $[Cu(CH_3CN)_4][PF_6]$ in THF produced an orange precipitate of $[(DPEN)Cu_2(\mu\text{-}NCMe)][PF_6]_2$ (**1**, eq. 2).

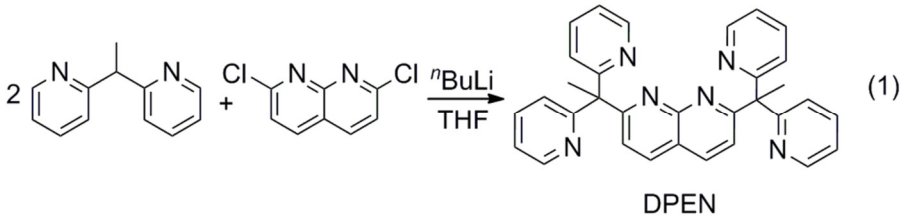

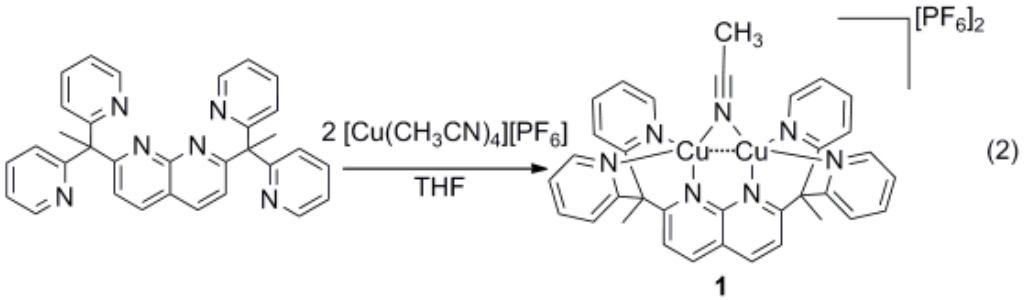

(2)

1

Compound **1** was crystallized by diffusion of THF into an acetonitrile solution of **1** to give crystals suitable for single-crystal X-ray diffraction (Figure 1). In the solid state structure of **1** each copper center is ligated by four nitrogen donors, one of which is an acetonitrile bridge. The coordination geometry for both Cu centers is strongly distorted from a tetrahedral environment by the rigid nature of DPEN, which enforces approximately 90° N–Cu–N angles involving the N donors of DPEN. This results in a coordination geometry for Cu that resembles a tripodal L_3M fragment of an octahedral complex capped by the bridging acetonitrile ligand.[26] This ligand is bound in a nearly symmetrical bridging position between the copper centers, with Cu–N bond lengths of 2.004(3) and 1.979(3) Å. These bond lengths are similar to distances found for terminally bound Cu^I-acetonitrile complexes.[27] The ligand leans slightly toward the Cu center associated with the longer Cu–NCMe bond, resulting in somewhat inequivalent Cu–N–C angles of 138.2(2) and 146.0(2)°. This suggests the possibility of a weak interaction with the nitrile π-system.[28] The infrared spectrum of complex **1** exhibits an acetonitrile stretch at ν(CN) = 2280 cm^{-1}. This value is higher than that for free acetonitrile, ν(CN) = 2255 cm^{-1} and similar to values for terminally-bound complexes of acetonitrile, ν(CN) = 2270-2300 cm^{-1}.[29] This is consistent with the presence of a short C–N bond in **1** (1.111(4) Å, compared to 1.157(9) Å in free acetonitrile[30]). Based on these observations we suggest that the acetonitrile is best described as a 2-electron donor that participates in a three-center, two-electron bond (Figure 2). This formal description is supported by the acute Cu–N–Cu angle (75.77(9)°) and a short Cu–Cu contact (2.4457(4) Å) that is characteristic of 3c-2e interactions.[1]

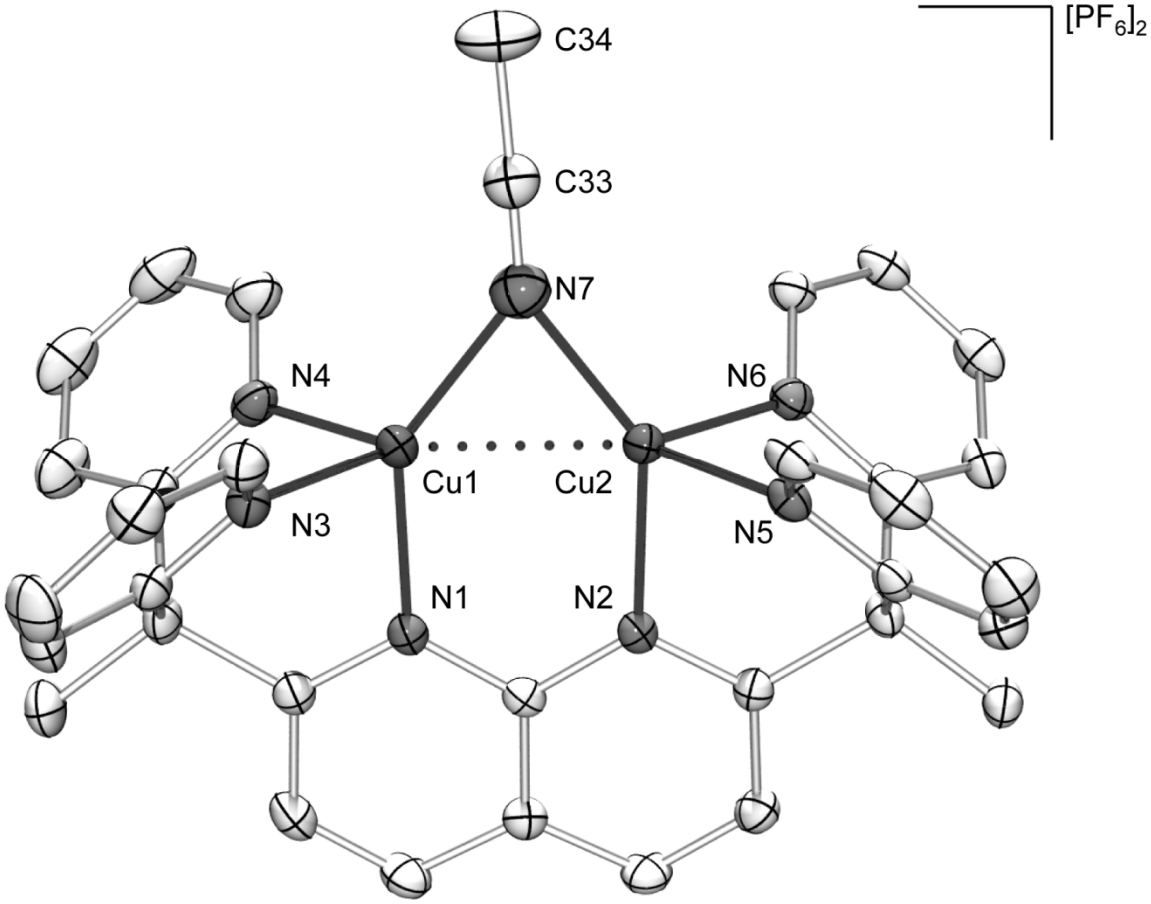

Figure 1. X-ray crystal structure of **1**. Hydrogen atoms and the PF_6^- counterions have been omitted for clarity. Selected bond lengths [Å] and angles [°]: Cu1–Cu2 2.4457(4), Cu1–N7 2.004(3), Cu2–N7 1.979(3), Cu1–N1 2.012(2), Cu1–N3 2.043(2), Cu1–N4 2.035(2), Cu2–N2 2.019(2), Cu2–N5 2.040(2), Cu2–N6 2.043(2), N7–C33 1.111(4), N7–C33–C34 178.8(3), Cu1–N7–C33 138.2(2), Cu2–N7–C33 146.0(2), Cu1–N7–Cu2 75.77(9), N1–Cu1–Cu2 88.28(6), N1–Cu1–N3 90.43(8), N1–Cu1–N4 91.37(8), N4–Cu1–N3 89.76(9).

A number of investigations have addressed the nature of short Cu(I)–Cu(I) contacts (< 2.5 Å) of the type exhibited by **1**, and considerable discussion has been devoted to whether such Cu(I)–Cu(I) contacts reflect the presence of a formal bond between the two metal centers[31-33] or simply results from steric constraints of the bridging ligands.[34-35] DFT calculations on **1** indicate that no formal bond exists between the two copper centers, as the *d*-type bonding and anti-bonding Cu–Cu interactions are all filled as shown in the filled molecular orbital that have significant *d*-orbital character in Figure 3. Further analysis of the Cu–Cu interaction using the Quantum Theory of Atoms in Molecules[36] determined the presence of a bond critical point between the two copper atoms. Maps of the electron density and the Laplacian of the electron density with indicated critical points is shown in Figure 4 and 5, respectively. Characteristics of bond critical points are given in Table 1. The characteristics of the bond critical point between the two copper atoms ($\rho = 0.038$, $\nabla^2\rho = +0.091$) are consistent with a closed-shell interaction.[36]

This is expected for a cuprophilic interaction, but would not be considered a formal single bond. Additionally, optimization of the geometry of the dicopper complex in the absence of a bridging ligand by DFT methods resulted in an increase in the Cu–Cu distance by 0.197 Å as shown in Figure 6. This indicates that the presence of the acetonitrile ligand is essential for maintaining the close Cu–Cu contact. Thus, the Cu-Cu interaction is characterized as a cuprophilic interaction and is represented in bonding diagrams by a dotted line between the two copper atoms.

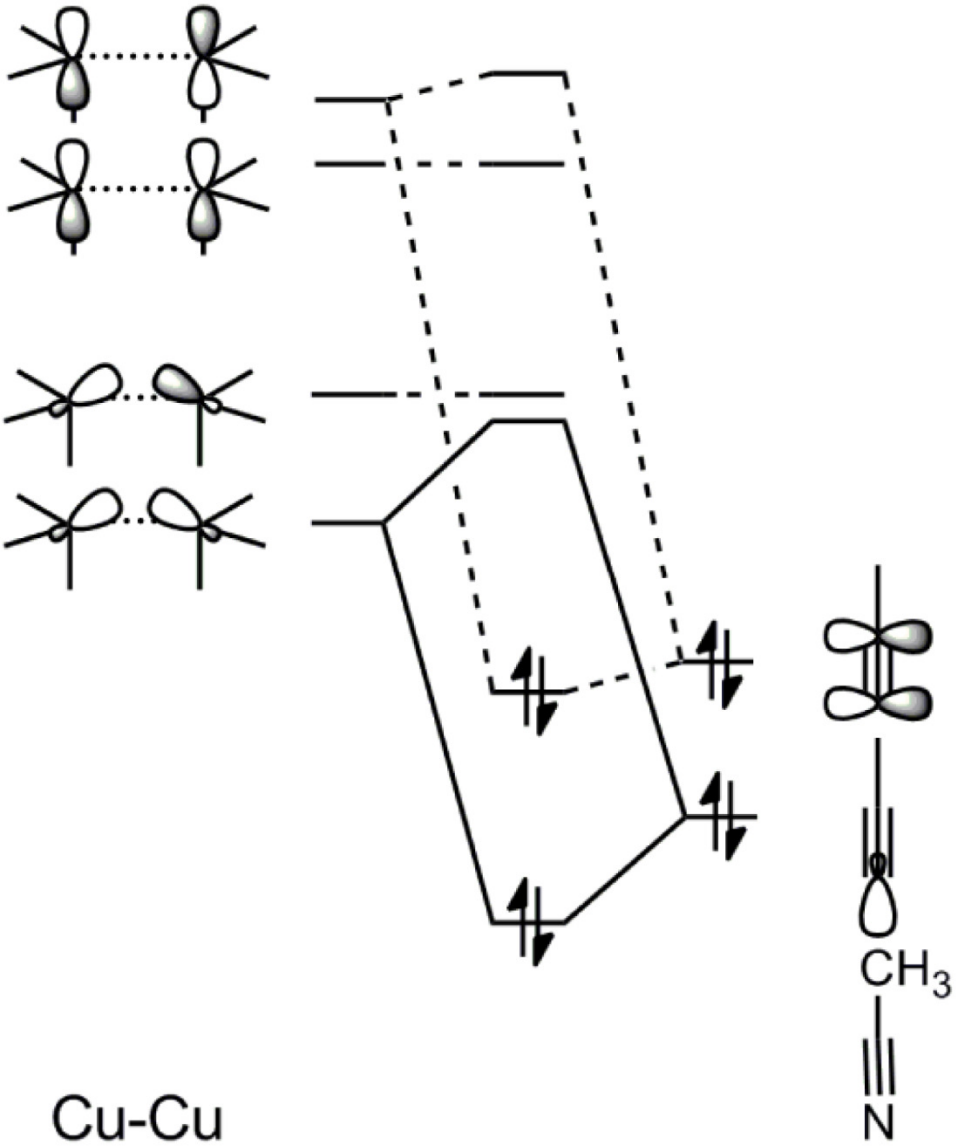

Figure 2. Qualitative molecular orbital diagram for the acetonitrile ligand of complex **1**. The Cu–Cu orbitals are constructed from the lowest energy combination of the empty Cu 4s and 4p orbitals. The N orbital on acetonitrile is from the nitrogen lone pair.

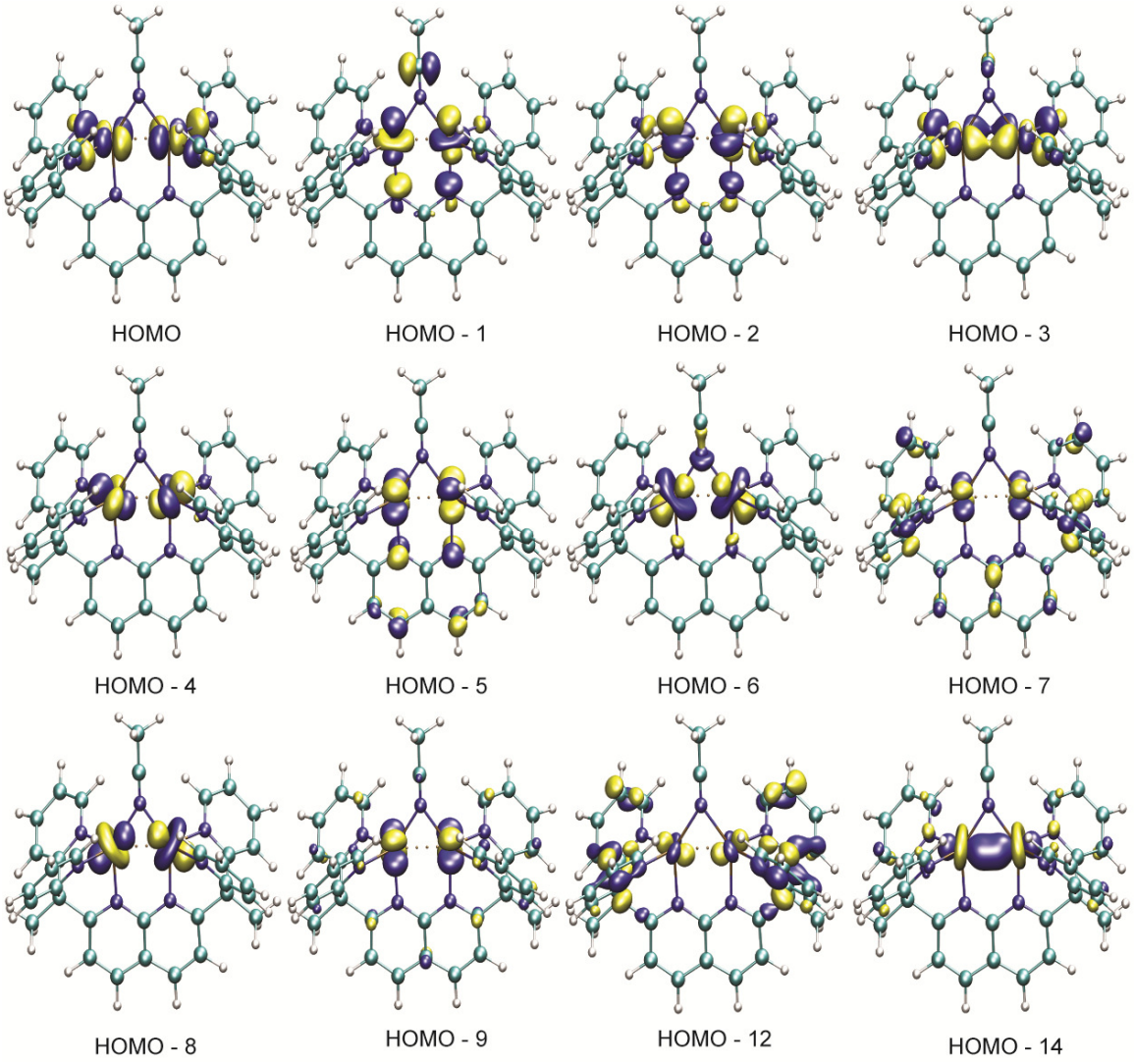

Figure 3. Molecular orbital diagrams of **1**. Only those orbitals containing significant contribution from Cu 3d orbitals are shown. Molecular orbital surfaces are shown at an isovalue of 0.05 e^{-} A^{-3}.

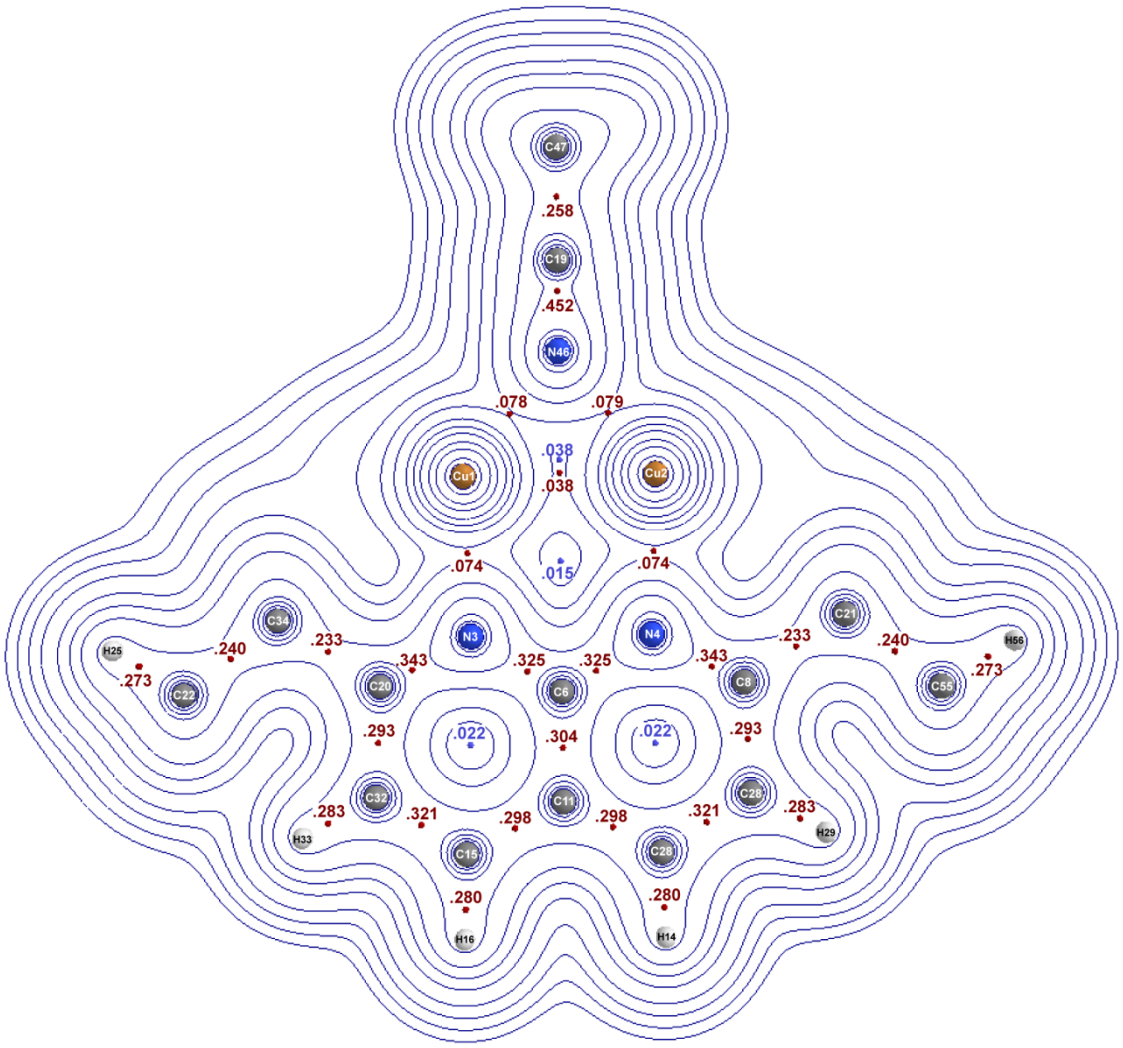

Figure 4. Contour plot of the electron density ρ of **1** in the Cu1-N46-Cu2 plane. Values listed on the diagram are the values of the electron density ρ (e^- $bohr^{-3}$) for the corresponding bond critical point (red) or ring critical point (blue). For clarity, only atoms in the plane are shown. Contour lines are drawn at 0.001, 0.002, 0.004, 0.008, 0.02, 0.04, 0.08, 0.2, 0.4, 0.8, 2.0, 4.0, 8.0, 20, 40, 80 e^- $bohr^{-3}$.

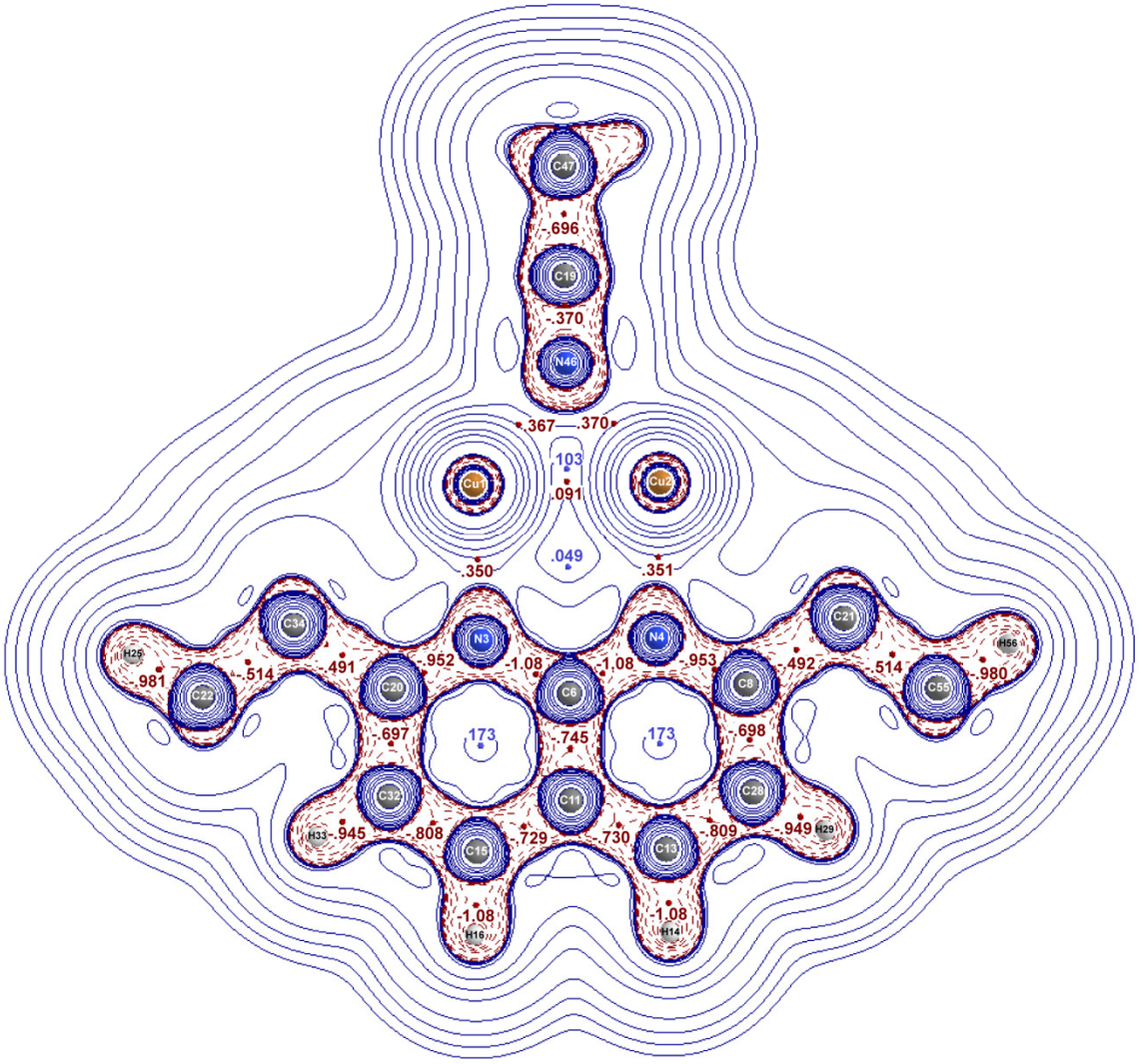

Figure 5. Contour plot of $\nabla^2\rho$ of **1** in the Cu1-N46-Cu2 plane. Values listed on the diagram are the values of $\nabla^2\rho$ (e^- $bohr^{-5}$) for the corresponding bond critical point (red) or ring critical point (blue). For clarity, only atoms in the plane are shown. Contour lines are drawn at 0, ±0.001, ±0.002, ±0.004, ±0.008, ±0.02, ±0.04, ±0.08, ±0.2, ±0.4, ±0.8, ±2.0, ±4.0, ±8.0, ±20, ±40, ±80 e^- $bohr^{-5}$. Positive contour lines are indicated by a solid blue line. Negative contour lines are indicated by a dashed red line.

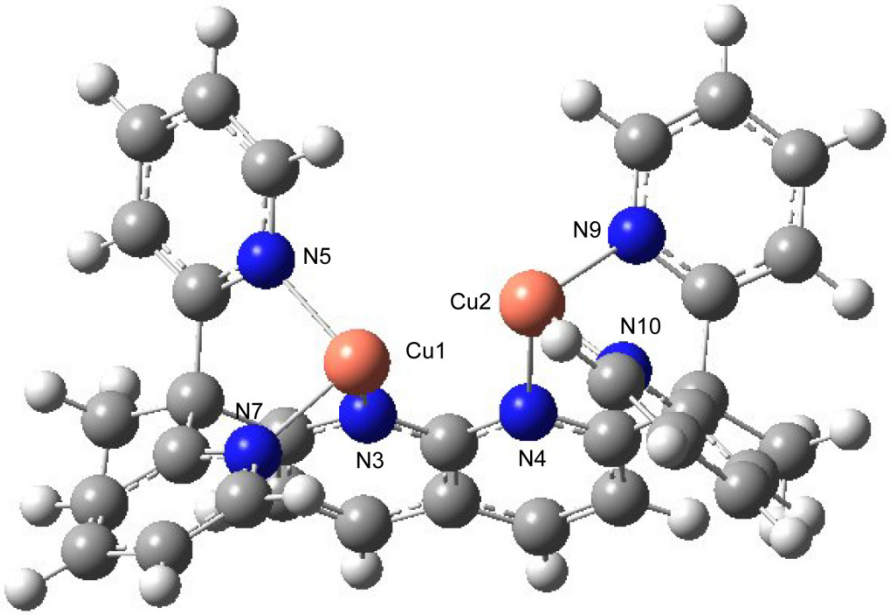

Figure 6. Optimized atomic coordinates of **1** without acetonitrile. Selected bond lengths [Å] and angles [°]: Cu1–Cu2 2.6835, Cu1–N3 2.0322, Cu1–N7 2.0380, Cu1–N5 2.0284, Cu2–N4 2.0349, Cu2–N10 2.0297, Cu2–N9 2.0380.

Table 1 Properties of selected bond critical points.

	ρ	$\nabla^2\rho$	ε
Cu1 – Cu2	0.0382	0.0910	0.7696
Cu1 – N3	0.0739	0.3497	0.0179
Cu2 – N4	0.0741	0.3509	0.0178
Cu2 – N10	0.0744	0.3516	0.0183
Cu1 – N5	0.0745	0.3523	0.0183
Cu2 – N46	0.0785	0.3701	0.0339
Cu1 – N7	0.0747	0.3532	0.0181
Cu2 – N9	0.0746	0.3523	0.0182
Cu1 – N46	0.0778	0.3668	0.0345

Scheme 1. Reaction of **1** with xylyl isocyanide and CO to form **2** and **3**.

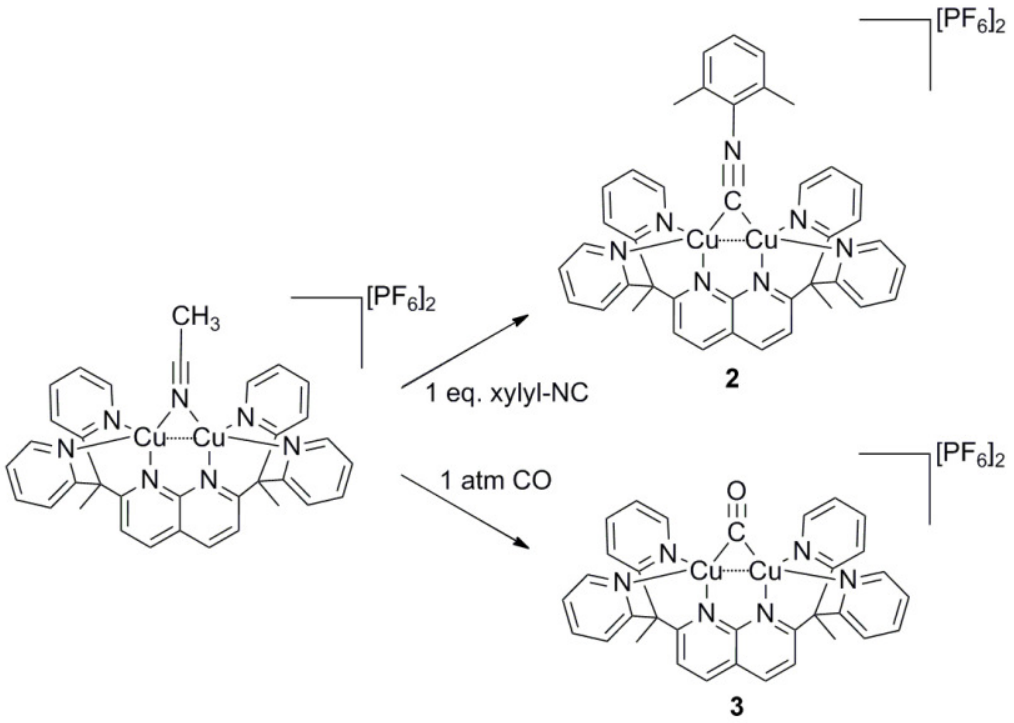

Because acetonitrile is commonly employed as a leaving group in ligand exchange reactions, it was of interest to determine the potential for complex **1** to serve as a precursor to other bridged dicopper complexes (Scheme 1). The yellow xylyl isocyanide-bridged complex $[(DPEN)Cu_2(\mu\text{-}CNXyl)][PF_6]_2$ (**2**) results from reaction of **1** with one equivalent of xylyl isocyanide in acetonitrile. X-ray quality crystals were grown by vapor diffusion of diethyl ether into a nitromethane solution of **2** (Figure 7). Also, the green carbonyl-bridged complex $[(DPEN)Cu_2(\mu\text{-}CO)][PF_6]_2$ (**3**) was formed by stirring a solution of **1** in nitromethane under an atmosphere of CO, and crystals were obtained by vapor diffusion of diethyl ether into an acetonitrile solution of **3** (Figure 8). The solid state structures of **2** and **3** reveal that the coordination geometry observed for **1** is retained after these simple ligand substitutions of acetonitrile. The Cu–C bond lengths in **2** and **3** are significantly shorter (1.907(2) and 1.910(2) Å for **2**; 1.889(3) and 1.898(3) Å for **3**) than the Cu–NCMe distance in **1**, which is consistent with stronger coordinating abilities for xylyl isocyanide and CO relative to acetonitrile. The xylyl isocyanide ligand in **2** adopts a somewhat unsymmetrical bridging geometry, as indicated by the bent nature of this ligand (∠ C–N–C = 161.8(2)°). Involvement of the π system of the isonitrile group of **2** in bonding xylyl isocyanide). A significant π-backbonding interaction is also reflected in a relatively low CO stretching frequency for **3** (1974 cm^{-1}; $\nu(CO_{gas})$ = 2143 cm^{-1}). This is similar to corresponding values reported for Cu^I complexes of bridging carbonyl ligands.[37-39] These observations for **2** and **3** are consistent with the expected greater π-acidity of these ligands relative to acetonitrile. However, it should be noted that Cu^I is associated with poor π-basicity, as indicated by the significantly high ν(CO) value relative to typical ν(CO) frequencies reported for bridging carbonyl ligands in other transition metal complexes (1700 – 1860 cm^{-1}).[40]

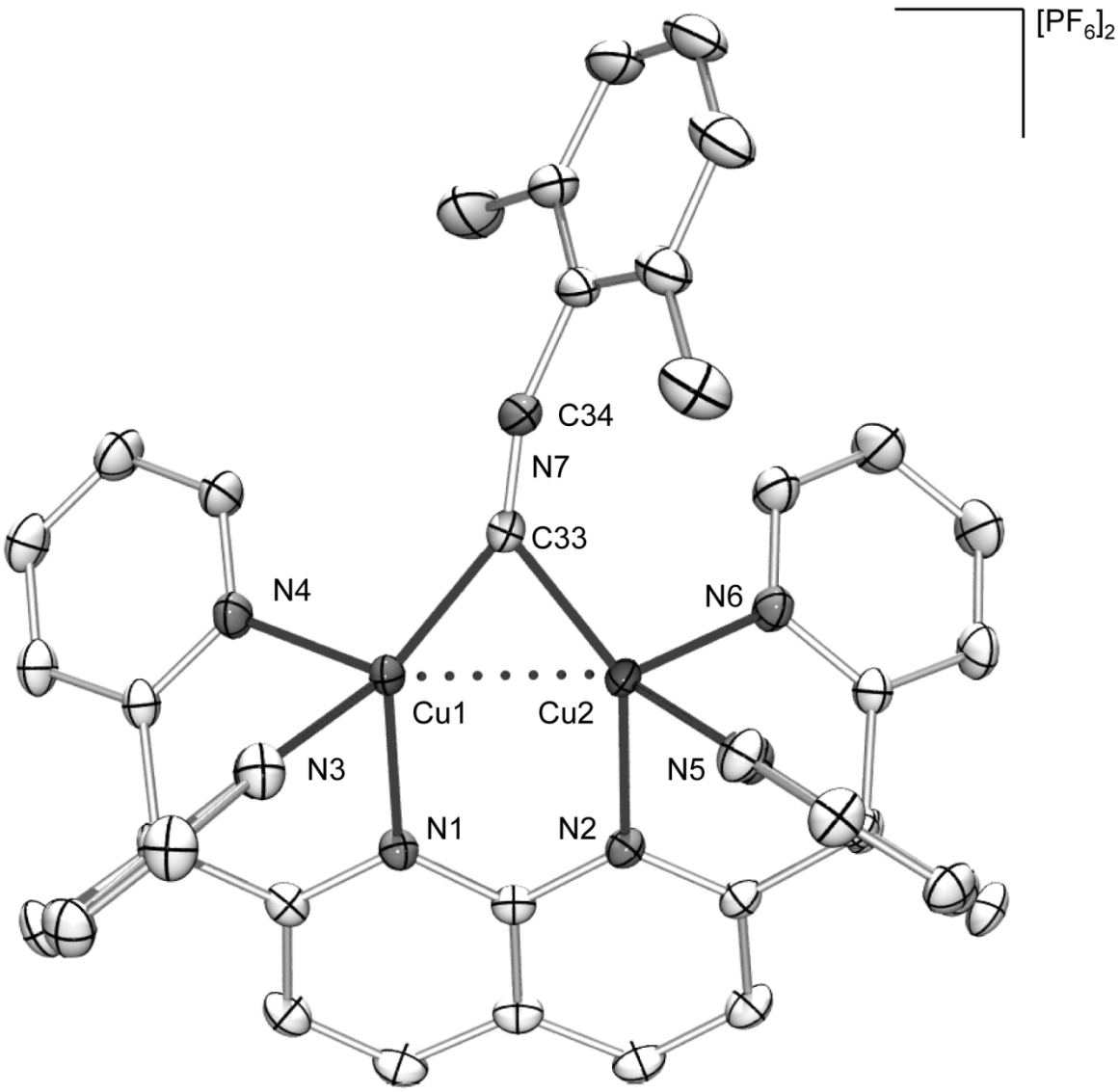

Figure 7. X-ray crystal structure of **2**. Hydrogren atoms and the PF_6^- counterions have been omitted for clarity. Selected bond lengths [Å] and angles [°]: Cu1–Cu2 2.3661(4), Cu1–C33 1.907(2), Cu2–C33 1.910(2), Cu1–N1 2.065(2), Cu1–N3 2.060(2), Cu1–N4 2.012(2), Cu2–N2 2.012(2), Cu2–N5 2.024(2), Cu2–N6 2.028(2), C33–N7 1.179(3), C33–N7–C34 161.8(2), Cu1–C33–N7 147.6(2), Cu2–C33–N7 134.8(2), Cu1–C33–Cu2 76.62(8), N1–Cu1–Cu2 87.24(5), N1–Cu1–N3 86.81(8), N1–Cu1–N4 92.11(9), N4–Cu1–N3 88.78(8).

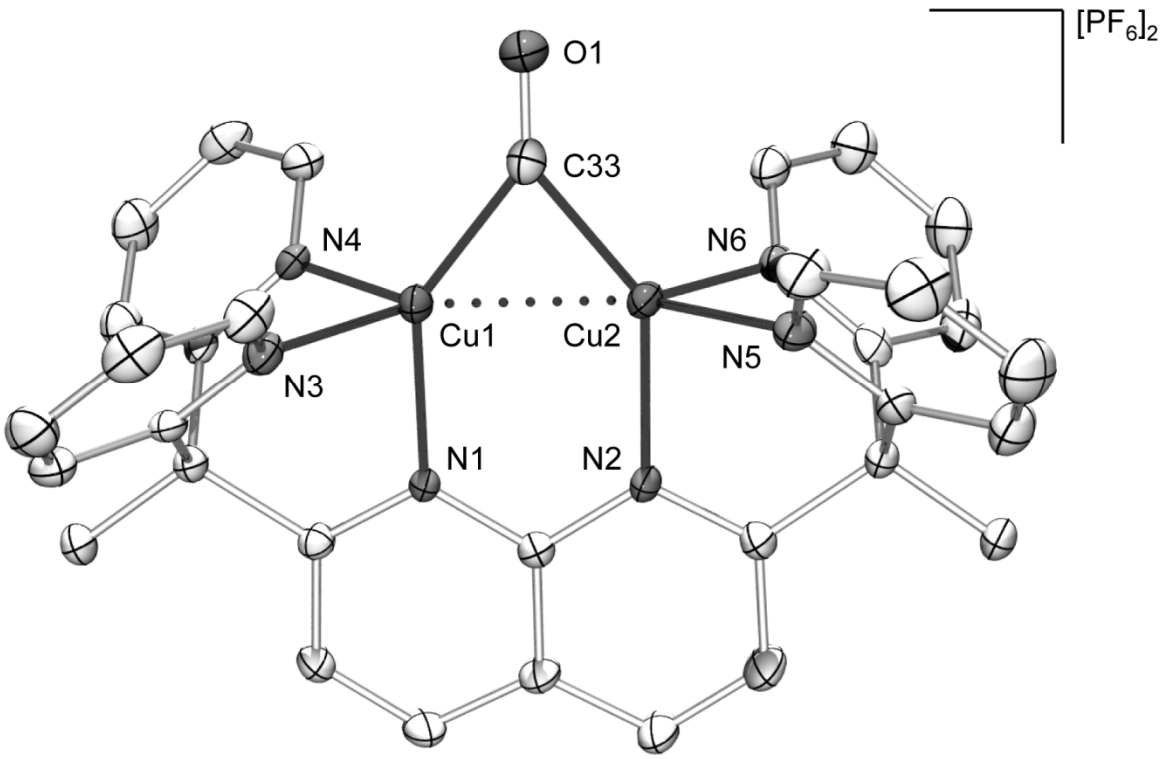

Figure 8. X-ray crystal structure of **3**. Hydrogen atoms and the PF_6^- counterions have been omitted for clarity. Selected bond lengths [Å] and angles [°]: Cu1–Cu2 2.3600(5), Cu1–C33 1.889(3), Cu2–C33 1.898(3), Cu1–N1 2.011(2), Cu1–N3 2.027(3), Cu1–N4 2.027(3), Cu2–N2 2.010(2), Cu2–N5 2.022(3), Cu2–N6 2.039(3), C33–O1 1.135(4), Cu1–C33–Cu2 77.1(1), Cu1–C33–O1 141.5(3), Cu2–C33–O1 141.3(3), N1–Cu1–Cu2 89.24(7), N1–Cu1–N3 89.6(1), N1–Cu1–N4 90.6(1), N4–Cu1–N3 90.9(1).

Conclusion

An unusual μ-η^1:η^1 acetonitrile-bridged dicopper complex was discovered that exhibits a 3-center, 2-electron bonding interaction involving acetonitrile supported by a cuprophilic interaction between the metal centers. Furthermore, this complex serves as a starting material for the synthesis of other bridging complexes by substitution of the acetonitrile ligand, providing a versatile platform for studying the interaction of small molecules with dinuclear copper centers.

Experimental

General Considerations. All manipulations were carried out using Schlenk techniques[41-42] under a purified N_2 atmosphere or in a Vacuum Atmospheres drybox. Solvents were purchased from Aldrich at spectroscopic grade. Dry THF was prepared by passage through a VAC drying column. Nitromethane was dried with $CaCl_2$, followed by $CaSO_4$, and then fractionally distilled under N_2. Acetonitrile was dried with CaH_2, and then fractionally distilled from CaH_2 under N_2. Acetonitrile used for crystallization was vacuum transferred from P_2O_5. Dry solvents were stored under N_2 in Straus flasks. $[Cu(CH_3CN)_4][PF_6]$, xylyl isocyanide, and *n*-bultylithium were purchased from Aldrich and used as received. CO was purchased from Praxair (99.998%) and

used as received. The reagents 1,1-di-(2-pyridyl)ethane and 2,7-dichloro-1,8-naphthyridine were prepared according to literature procedures.[2] NMR spectra were recorded on Bruker AV-600, AVQ-400 and AV-300 spectrometers at room temperature. ^{1}H NMR spectra were referenced to residual protio solvent peaks (δ 2.05 for $(CD_3)_2CO$, δ 4.33 for CD_3NO_2). $^{13}C\{^{1}H\}$ NMR spectra were referenced to solvent resonances (δ 54.00 for CD_2Cl_2, δ 29.92 for $(CD_3)_2CO$). Elemental analyses were carried out by the College of Chemistry Microanalytical Laboratory at the University of California, Berkeley. Infrared spectra were recorded on a Nicolet Nexus 6700 FTIR spectrometer with a liquid-nitrogen-cooled MCT-B detector. Measurements were made at 4.0 cm^{-1} resolution. UV-vis spectra were obtained on a Cary 300 Bio spectrophotometer in 1-cm air-free quartz cells.

Synthesis of 2,7-bis(1,1-di-(2-pyridyl)ethyl)-1,8-naphthyridine (DPEN).

n-Butyllithium (1.6 M in hexanes, 27 mL, 43 mmol) was added dropwise to a stirred solution of freshly distilled 1,1-di-(2-pyridyl)ethane (8.0 g, 43 mmol) in 200 mL of THF at 0° C. The red solution was stirred for 30 min. after which 2,7-dichloro-1,8-naphthyridine (3.8 g, 19 mmol) was added. The purple solution was stirred for 16 h as the vessel warmed to room temperature. After addition of 10 mL water, the mixture was filtered. The precipitate was dissolved in a 1:1 CH_2Cl_2/H_2O mixture and filtered to remove residual 2,7-dichloro-1,8-naphthyridine. The aqueous fraction was extracted with CH_2Cl_2 (2 x 30 mL) and the combined organic fractions were dried over $MgSO_4$ and evaporated to dryness. The crude material was recrystallized from hot acetonitrile to give white crystals of 2,7-bis(1,1-di-(2-pyridyl)ethyl)-1,8-naphthyridine (DPEN). Additional material can be obtained by evaporation of the mother liquor to dryness followed by extraction and recrystallization (recrystallized yield: 5.9 g, 12 mmol, 62%). **^{1}H NMR** (CD_2Cl_2, 400.13 MHz): δ 8.52 (d, J_{HH} = 4.0 Hz, of q, J_{HH} = 0.9 Hz, 4H), 7.98 (d, J_{HH} = 8.0 Hz, 2H), 7.61 (t, J_{HH} = 8.0 Hz, of d, J_{HH} = 2.8 Hz, 4H), 7.36 (d, J_{HH} = 8.0 Hz, 2H), 7.22 (d, J_{HH} = 8.0 Hz, of t, J_{HH} = 0.9 Hz, 4H), 7.15 (d, J_{HH} = 8.0 Hz, of d, J_{HH} = 4.0 Hz, of d, J_{HH} = 1.2 Hz, 4H), 2.37 (s, 6H). **$^{13}C\{^{1}H\}$ NMR** (CD_2Cl_2, 100.62 MHz): δ 168.9, 165.7, 154.3, 148.6, 136.0, 135.3, 123.8, 123.2, 121.3, 119.4, 61.0 (*C*(Me)), 27.1 (C(*C*H$_3$)). **EA** Anal. Calcd (%) for $C_{32}H_{26}N_6$ (494.28): C, 77.70, H, 5.31, N, 16.99. Found: C, 77.24, H, 5.33, N, 16.74. **HRMS** (ESI): Calcd. for $C_{32}H_{27}N_6$ $[M+H]^+$: 495.2292; Found: 495.2300.

Synthesis of $[Cu_2(\mu\text{-}NCCH_3)(DPEN)][PF_6]_2$ (1). DPEN (1.2 g, 2.4 mmol) was dissolved in 100 mL of THF. The light yellow solution was transferred to a mixture of $Cu(CH_3CN)_4(PF_6)$ (1.8 g, 4.9 mmol) in 100 mL of THF. The resulting dark red solution was stirred for 12 hrs. during which time an orange precipitate formed. The solution was filtered to give the orange solid $[Cu_2(\mu\text{-}NCCH_3)(DPEN)](PF_6)_2$ (**1**) analytically pure (2.13 g, 2.2 mmol, 93%). The orange solid was recrystallized by vapor diffusion of THF into an acetonitrile solution to give X-ray quality crystals. **^{1}H NMR** (CD_3CN, 300.13 MHz): δ 8.50 (br, 4H), 8.27 (d, J_{HH} = 8.4 Hz, 2H), 7.87 (br, 4H), 7.72 (br, 4H), 7.33 (br, 6H), 2.40 (s, 6H), 1.96 (s, 3H). **$^{13}C\{^{1}H\}$ NMR** (CD_3CN, 150.92 MHz): δ 169.1, 161.4, 154.6, 150.4, 139.3, 138.9, 124.6, 124.3, 123.9, 121.4, 59.4 (*C*(Me)), 27.1 (C(*C*H$_3$)). **EA** Anal. Calcd (%) for $Cu_2C_{34}H_{29}N_7P_2F_{12}$ (952.68): C, 42.87, H, 3.07, N, 10.29. Found: C, 43.16, H, 3.45, N, 10.61. **IR** (KBr, $\overline{\nu}$ (cm^{-1})): 2273 (w, $\nu_{C\equiv N}$).

Synthesis of $[Cu_2(\mu\text{-}CNXyl)(DPEN)][PF_6]_2$ (2). Xylyl isocyanide (0.015 g, 0.11 mmol was dissolved in 5 mL of acetonitrile and the resulting solution was transferred to a solution of **1** (0.11 g, 0.12 mmol) in 5 mL acetonitrile. The resulting yellow solution was stirred for 30 min. after which it was concentrated under vacuum and the product was precipitated with 20 mL of THF. The precipitate was washed with THF (3 × 10 mL) and subsequently dried under dynamic vacuum (0.083 g, 0.080 mmol, 72%). The yellow solid was recrystallized by vapor diffusion of

diethyl ether into a nitromethane solution to give X-ray quality crystals. **^{1}H NMR** ($(CD_3)_2CO$, 300.13 MHz): δ 9.45 (d, J_{HH} = 3.9 Hz, 4H), 9.00 (d, J_{HH} = 8.7 Hz, 2H), 8.66 (d, J_{HH} = 8.7 Hz, 2H), 8.39 (d, J_{HH} = 8.4 Hz, 4H), 8.20 (t, J_{HH} = 7.5 Hz, 4H), 7.68 (t, J_{HH} = 6.2 Hz, 4H), 7.45 (t, J_{HH} = 7.5 Hz, 1H), 7.33 (d, J_{HH} = 7.5 Hz, 2H), 3.17 (s, 6H), 2.43 (s, 6H). **^{13}C{^{1}H} NMR** ($(CD_3)_2CO$, 150.92 MHz): δ 163.5, 156.3, 151.6, 151.0, 149.6 (N*C*) 142.6, 141.3, 136.1, 131.0, 129.5, 129.2, 125.3, 125.0, 124.1, 122.7, 53.9, 23.8, 19.6. **EA** Anal. Calcd (%) for $Cu_2C_{41}H_{35}N_7P_2F_{12}$ (1042.80): C, 47.22, H, 3.38, N, 9.40. Found: C, 47.47, H, 3.50, N, 9.27. **IR** (KBr, $\overline{\nu}$ (cm^{-1})): 2036 (s, $\nu_{C\equiv N}$).

Synthesis of [Cu$_2$(μ-CO)(DPEN)][PF$_6$]$_2$ (3). 1 (0.10 g, 0.10 mmol) was dissolved in 5 mL of nitromethane. CO (1 atm) was added to the reaction vessel and the solution quickly changed color from red to green. The reaction mixture was stirred for 30 min. after which the solution was concentrated under vacuum and the product was precipitated with 20 mL of THF. The precipitate was washed with THF (3 × 10 mL) and subsequently dried under dynamic vacuum (0.072 g, 0.077 mmol, 77%). The green solid was recrystallized by vapor diffusion of diethyl ether into an acetonitrile solution to give X-ray quality crystals. **^{1}H NMR** ($(CD_3)_2CO$, 300.13 MHz): δ 9.32 (d, J_{HH} = 4.2 Hz, 4H), 9.07 (d, J_{HH} = 8.7 Hz, 2H), 8.70 (d, J_{HH} = 8.7 Hz, 2H), 8.41 (d, J_{HH} = 8.4 Hz, 4H), 8.25 (t, J_{HH} = 7.4 Hz, 4H), 7.75 (t, J_{HH} = 6.3 Hz, 4H), 3.16 (s, 6H). **^{13}C{^{1}H} NMR** ($(CD_3)_2CO$, 150.92 MHz): δ 210.1 (*C*O) 163.4, 155.8, 151.7, 151.7, 143.4, 141.9, 125.7, 125.4, 124.4, 122.98, 53.9, 23.6. **EA** Anal. Calcd (%) for $Cu_2C_{33}H_{26}N_6OP_2F_{12}$ (939.62): C, 42.18, H, 2.79, N, 8.94. Found: C, 41.92, H, 2.97, N, 8.86. **IR** (KBr, $\overline{\nu}$ (cm^{-1})): 1971 (s, $\nu_{C\equiv O}$).

X-ray Crystallography. X-ray diffraction data were collected using Bruker AXS three-circle diffractometers coupled to a CCD detector with either QUAZAR multilayer mirror- or graphite-monochromated Mo Kα radiation (λ = 0.71073 Å). The structures were solved by direct methods using SHELXS and refined against F^2 on all data by full-matrix least squares with SHELXL-97. All non-hydrogen atoms were refined anisotropically; hydrogen atoms were included into the model at their geometrically calculated positions and refined using a riding model excepting hydrogen atoms of water molecules, which were located from the electron difference map. Due to disorder in the solvent molecules in the structures of **1**, and **3,** the solvent molecules were treated as a diffuse contribution to the overall scattering without specific atom positions by SQUEEZE/PLATON. Experimental details of the crystal structures for DPEN, **1**, **2**, and **3** are given in Table 2. An ORTEP diagram of DPEN is given in Figure 9.

Table 2 Experimental details for the X-ray crystal structures of **DPEN**, **1**, **2**, and **3**.

	DPEN	**1**	**2**	**3**
Chemical formula	$C_{32}H_{26}N_6 \bullet H_2O$	$Cu_2(CH_3CN)(C_{32}H_{26}N_6)(PF_6)_2 \bullet 2.5(C_4H_8O)$	$2(Cu_2(C_9H_9N)(C_{32}H_{26}N_6)(PF_6)_2) \bullet 5.6(CH_3NO_2) \bullet C_4H_{10}O$	$Cu_2(CO)(C_{32}H_{26}N_6)(PF_6)_2$
Formula Mass	512.61	1132.92	2501.53	939.62
Crystal system	Monoclinic	Triclinic	Monoclinic	Triclinic
a/Å	8.7330(13)	12.5667(7)	16.8461(10)	12.1315(5)
b/Å	26.926(4)	12.6412(7)	13.9649(8)	12.5831(5)
c/Å	11.7460(17)	14.9476(9)	22.7690(13)	17.3389(7)
α/°	90.00	93.162(3)	90.00	95.135(2)
β/°	105.264(2)	102.705(3)	106.553(3)	109.192(2)
γ/°	90.00	100.697(3)	90.00	112.841(2)
Unit cell volume/Å^3	2664.6(7)	2264.7(2)	5134.5(5)	2230.87(16)
Temperature/K	138(2)	100(2)	100(2)	100(2)
Space group	$P2_1$	$P\bar{1}$	$P2_1/n$	$P\bar{1}$
No. of formula units per unit cell, *Z*	4	2	2	2
No. of independent reflections	4993	9596	17858	8075
R_{int}	0.0869	0.0440	0.0393	0.0380
Final R_1 values ($I > 2\sigma(I)$)	0.0424	0.0400	0.0523	0.0423
Final $wR(F^2)$ values (*all data*)	0.1022	0.1042	0.1399	0.1087

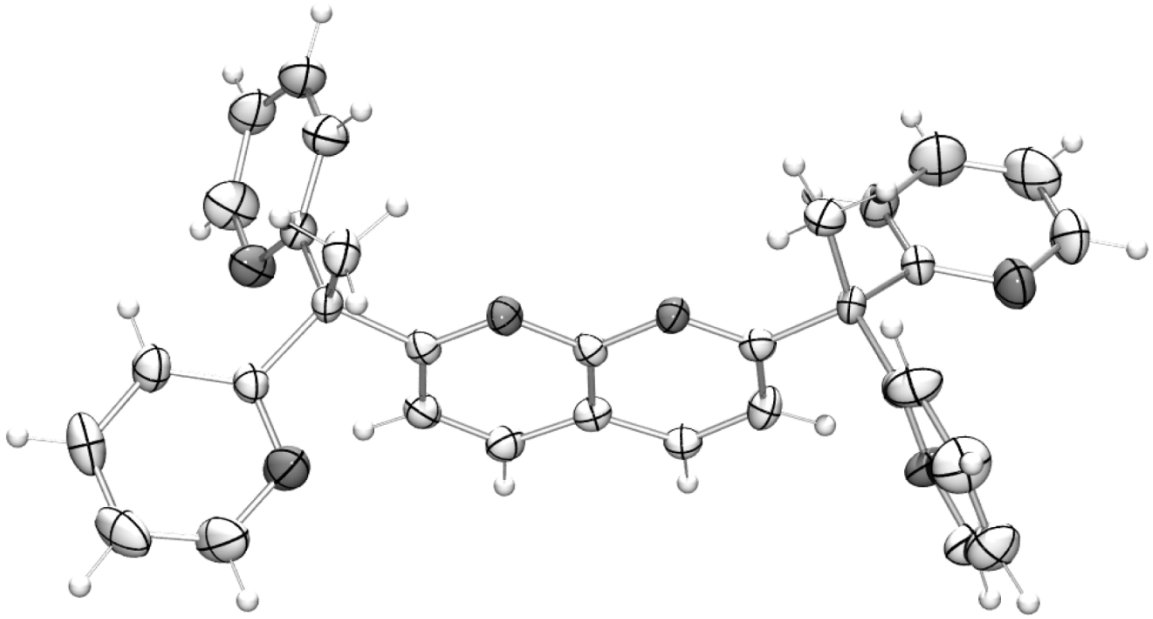

Figure 9. Crystal structure of DPEN.

Computational Experiments. DFT calculations were performed at the Molecular Graphics and Computation Facility of the University of California, Berkeley using the Gaussian 09 suite of *ab initio* programs.[45] Atoms were modeled using the long-range corrected hybrid functional ωB97xD,[46] and all-electron cc-PVDZ basis sets (H, C, and N)[47], and the cc-PVTZ basis set (Cu).[48] The DFT structures were optimized as a gas phase structure. The optimized geometry determined for **1** is given in Figure 10 and the atomic coordinates are given in Table 3. The calculated metal complex has a full-size DPEN ligand without simplification. The ground state was confirmed as a singlet through comparison with the optimized triplet analog. Calculating the harmonic frequencies for the optimized structure confirmed there were no imaginary frequencies. The 3D molecular structure figures displayed were drawn using the Gaussview and Adobe Illustrator visualization and manipulation programs. Molecular orbital surfaces were exported from Gaussview as cubefiles, visualized in VMD[49] and rendered with the Pov-Ray raytracer program. Contour plots of the electron density ρ and $\nabla^2\rho$ were created using AIMAll.[50]

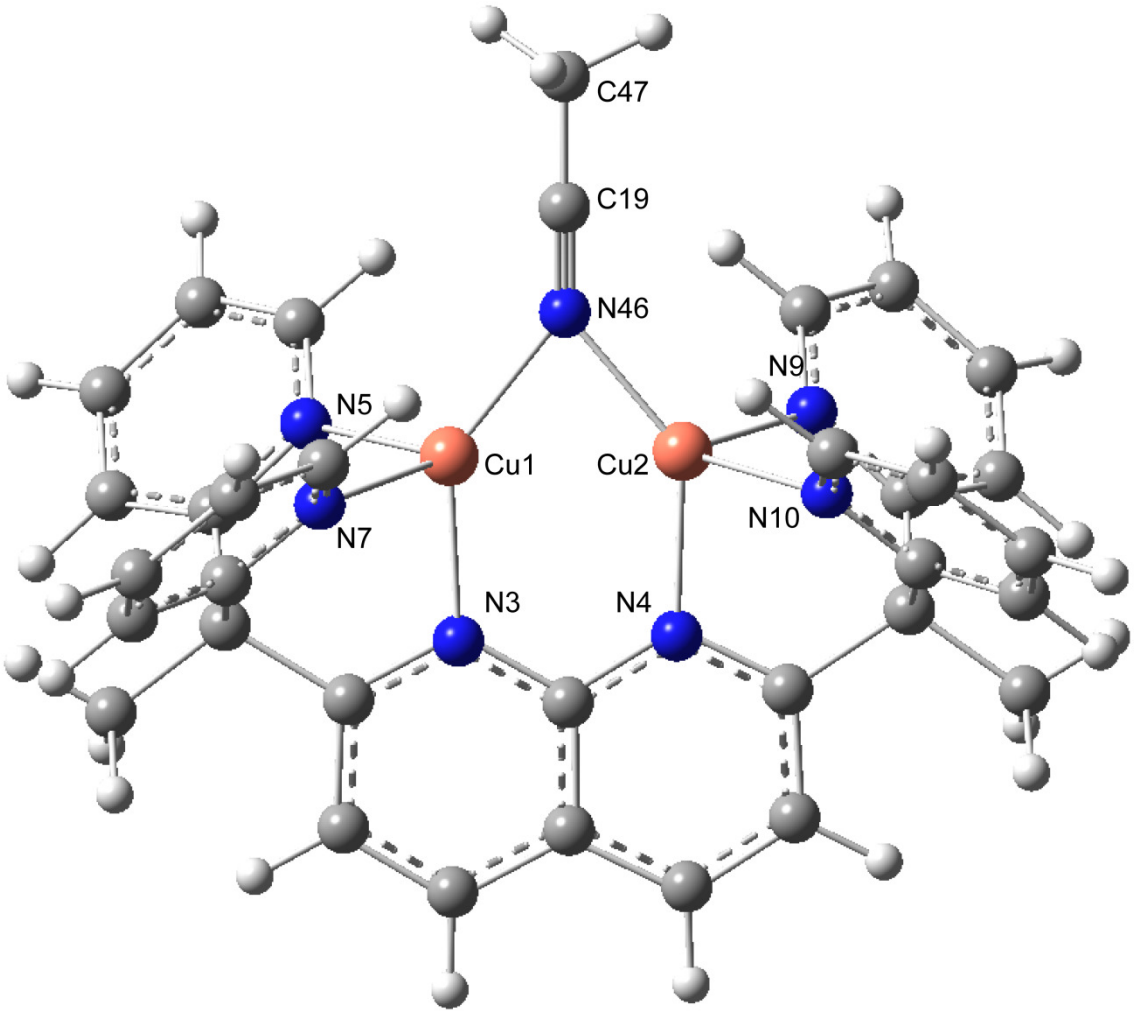

Figure 10. Optimized atomic coordinates of **1**. Selected bond lengths [Å] and angles [^{o}]: Cu1–Cu2 2.4865, Cu1–N46 2.0088, Cu2–N46 2.0085, Cu1–N3 2.0695, Cu1–N7 2.0802, Cu1–N5 2.0788, Cu2–N4 2.0663, Cu2–N10 2.0793, Cu2–N9 2.0807, N46–C19 1.1687, N46–C19–C47 179.88, Cu1–N46–Cu2 76.48.

Table 3 Cartesian coordinates of the optimized geometry of **1**.

	X (Å)	Y (Å)	Z (Å)
Cu1	0	0	0
Cu2	0.8086	1.9956	1.2053
N3	-1.8217	0.9570	-0.2096
N4	-1.0559	2.8384	0.9112
N5	-0.9843	-1.7276	0.5731
C6	-2.0763	2.2100	0.2620
N7	-0.0872	-0.5795	-1.9835
C8	-1.2262	4.0595	1.4017
N9	0.7755	2.6303	3.1744
N10	1.6914	3.7746	0.6216
C11	-3.3316	2.8248	0.0874
C12	-1.2619	-1.0865	-2.3965
C13	-3.5085	4.1237	0.6133
H14	-4.4686	4.6296	0.4984
C15	-4.3306	2.1010	-0.6004
H16	-5.3145	2.5472	-0.7557
C17	0.9424	-0.5029	-2.8366
H18	1.8628	-0.0755	-2.4331
C19	2.8610	-0.2005	0.9479
C20	-2.7642	0.2794	-0.8523
C21	-0.0334	4.7459	2.1348
C22	-3.6735	-1.7376	-2.0676
H23	-3.9753	-1.1233	-2.9247
H24	-4.5250	-1.7990	-1.3792
H25	-3.4737	-2.7493	-2.4397
C26	0.7233	3.6353	5.7516
H27	0.6982	4.0475	6.7611
C28	-2.4699	4.7340	1.2628
H29	-2.6144	5.7310	1.6653
C30	-0.6226	-2.4902	1.6130
H31	0.2493	-2.1470	2.1738
C32	-4.0515	0.8443	-1.0649
H33	-4.8252	0.2960	-1.5921
C34	-2.4339	-1.1537	-1.3709
C35	1.1344	1.8705	4.2172
H36	1.4385	0.8489	3.9794
C37	-2.3985	-4.0156	1.2174
H38	-2.9654	-4.9159	1.4578
C39	0.3463	4.4268	4.6703
H40	0.0334	5.4492	4.8607
C41	0.8710	-0.9296	-4.1540
H42	1.7359	-0.8477	-4.8114
C43	-1.4086	-1.5376	-3.7112
H44	-2.3449	-1.9542	-4.0707
C45	-2.0496	-2.0717	-0.1711
N46	1.8244	0.3066	0.8008
C47	4.1559	-0.8328	1.1344
H48	4.7727	-0.6820	0.2379
H49	4.0203	-1.9101	1.3038
H50	4.6626	-0.3882	2.0026
C51	0.3793	3.8990	3.3766
C52	2.7248	3.8596	-0.2257
H53	3.0922	2.9118	-0.6252
C54	1.1713	4.8929	1.1565
C55	-0.4656	6.1438	2.6060
H56	0.3567	6.6528	3.1228
H57	-1.3103	6.0866	3.3032

H58	-0.7668	6.7742	1.7605
C59	-1.2964	-3.6460	1.9778
H60	-0.9649	-4.2348	2.8325
C61	1.1262	2.3250	5.5275
H62	1.4266	1.6686	6.3434
C63	-2.7785	-3.2238	0.1373
H64	-3.6427	-3.5264	-0.4466
C65	2.7865	6.2261	-0.0442
H66	3.2092	7.2000	-0.2943
C67	-0.3351	-1.4600	-4.5943
H68	-0.4486	-1.8140	-5.6197
C69	1.7098	6.1419	0.8342
H70	1.3100	7.0602	1.2540
C71	3.3102	5.0620	-0.5921
H72	4.1494	5.0811	-1.2866

References

(1) Oliver, J. P. in *Advances in Organometallic Chemistry*, Vol. 15 (Eds: F. G. A. Stone, R. West) Academic Press, New York, **1977**, p. 235–271.
(2) van Koten, G. *J. Organomet. Chem.,* **1990**, *400*, 283–301.
(3) Green, M. L. H. *Comments Inorg. Chem.*, **2010**, *31*, 90–94.
(4) Sauthier, M.; Le Guennic, B.; Deborde, V.; Toupet, L.; Halet, J.-F.; Réau, R. *Angew. Chem. Int. Ed.*, **2001**, *40*, 228–231.
(5) Sauthier, M.; Leca, F.; Toupet, L.; Réau, R. *Organometallics*, **2002**, *21*, 1591–1602.
(6) Leca, F.; Sauthier, M.; Deborde, V.; Toupet, L.; Réau, R.; *Chem. Eur. J.*, **2003**, *9*, 3785–3795.
(7) Leca, F.; Lescop, C.; Rodriguez, E.; Costuas, K.; Halet, J.-F.; Réau, R. *Angew. Chem. Int. Ed.*, **2005**, *44*, 4362–4365.
(8) Nohra, B.; Rodriguez-Sanz, E.; Lescop, C.; Réau, R. *Chem. Eur. J.*, **2008**, *14*, 3391–3403.
(9) Pechmann, T.; Brandt, C. D.; Werner, H. *Angew. Chem. Int. Ed.*, **2000**, *39*, 3909.
(10) Pechmann, T.; Brandt, C. D.; Röger, C.; Werner, H. *Angew. Chem. Int. Ed.*, **2002**, *41*, 2301–2303.
(11) Pechmann, T.; Brandt, C. D.; Werner, H. *Chem. Commun.*, **2003,** 1136–1137.
(12) Pechmann, T.; Brandt, C. D.; Werner, H. *Chem. Eur. J.*, **2004**, *10*, 728–736.
(13) Pechmann, T.; Brandt, C. D.; Werner, H. *Dalton Trans.*, **2004**, 959–966.
(14) Evans, W. J.; Greci, M. A.; Ziller, J. W. *Chem. Commun.*, **1998**, 2367–2368.
(15) Cotton, F. A.; Daniels, L. M.; Murillo, C. A.; Wang, X. *Polyhedron* **1998**, *17*, 2781–2793.
(16) Beckwith, J. D.; Tschinkl, M.; Picot, A.; Tsunoda, M.; Bachman, R.; Gabbaï, F. P. *Organometallics*, **2001**, *20*, 3169–3174.
(17) Lin, P.; Clegg, W.; Harrington, R. W.; Henderson, R. A. *Dalton Trans.*, **2005**, 2349–2351.
(18) Al-Mandhary, M. R. A.; Fitchett, C. M.; Steel, P. J. *Aust. J. Chem.*, **2006**, *59*, 307–314.
(19) Lorber, C.; Choukroun, R.; Vendier, L. *Organometallics*, **2008**, *27*, 5017–5024.
(20) Li, X.-L.; Meng, X.-G.; Xu, S.-P. *Chin. J. Struct. Chem.*, **2009**, *28*, 1619–1624. The dicopper(I) μ-η1:η1 acetonitrile complex reported in ref 7 differs significantly from **1**. In particular, the Cu-Cu distance (3.168(9) Å) and Cu-N_{bridge} bond lengths (2.289(5) Å and 2.323(5) Å) are significantly longer (by 0.72 Å and 0.3 Å, respectively) than corresponding values for **1**. Thus, the bonding description outlined above for **1** likely does not apply to the complex in ref 7.

(21) Gavrilova, A.L.; Bosnich, B. *Chem. Rev.*, *2004*, *104*, 349–383.
(22) He, C.; Lippard, S. J. *Inorg. Chem.*, **2000**, *39*, 5225–5231.
(23) He, C.; Lippard, S. J *Tetrahedron*, **2000**, *56*, 8245–8252.
(24) He, C.; Barrios, A. M.; Lee, D.; Kuzelka, J.; Daavydov, R. M.; Lippard, S. J. *J. Am. Chem. Soc.*, **2000**, *122*, 12683–12690.
(25) He, C.; Dubois, J. L.; Hedman, B.; Hodgson, K. O.; Lippard, S. J. *Angew. Chem. Int. Ed.*, **2001**, *40*, 1484–1487.
(26) Albright, T. A.; Burdett, J. K.; Whangbo, M.-H. *Orbital Interactions in Chemistry*, John Wiley & Sons, New York, **1985**, p. 381.
(27) Black, J. R.; Levason, W.; Webster, M. *Acta Cryst.*, **1995**, *C51*, 623–625.
(28) Germain, M. E.; Temprado, M.; Castonguay, A.; Kryatova, O. P.; Rybak-Akimova, E. V.; Curley, J. J.; Mendiratta, A.; Tsai, Y.-C.; Cummins, C. C.; Prabhakar, R.; McDonough, J. E.; Hoff, C. D. *J. Am. Chem. Soc.*, **2009**, *131*, 15412–15423.
(29) Endres, H. in *Comprehensive Coordination Chemistry*, Vol. 2 (Eds: G. Wilkinson, R. D. Gillard, J. A. McCleverty) Pergamon Books Ltd., Oxford, **1987**, p. 261.
(30) Demaison, J.; Dubrulle, A.; Boucher, D.; Burie, J. *J. Mol. Spectrosc.*, **1979**, *76*, 1–16.
(31) Merz, Jr., K. M.; Hoffmann, R. *Inorg. Chem.*, **1998**, *27*, 2120–2127.
(32) Kölmel, C.; Ahlrichs, R. *J. Phys. Chem.*, **1990**, *94*, 5536–5542.
(33) Mealli, C.; Godinho, S. S. M. C.; Calhorda, M. J. *Organometallics*, **2001**, *20*, 1734–1742.
(34) Cotton, F. A.; Feng, X.; Timmons, D. J. *Inorg. Chem.*, **1998**, *37*, 4066.
(35) Clérac, R.; Cotton, F. A.; Daniels, L. M.; Gu, J.; Murillo, C. A.; Zhou, H.-C. *Inorg. Chem.*, **2000**, *39*, 4488.
(36) Bader, R. F. W. *Atoms in Molecules: A Quantum Theory*, Oxford University Press, Oxford, **1990**.
(37) Pasqualli, M.; Floriani, C.; Gaetani-Manfredotti, A.; Guastini, C. *J. Am. Chem. Soc.*, **1981**, *103*, 185–186.
(38) Pasqualli, M.; Floriani, C.; Venturi, G.; Gaetani-Manfredotti, A.; Villa, A. C. *J. Am. Chem. Soc.*, **1982**, *104*, 4092–4099.
(39) Doyle, G.; Eriksen, K. A.; Modrick, M.; Ansell, G. *Organometallics*, **1982**, *1*, 1613–1618.
(40) Miessler, G. L.; Tarr, D. A. *Inorganic Chemistry*, 3rd Ed., Pearson Prentice Hall, Upper Saddle River, NJ, **2004**, p. 470.
(41) Shriver, D. F.; Drezdon, M. A. *The Manipulation of Air-Sensitive Compounds*. 2nd Ed., John Wiley & Sons, New York, **1986**.
(42) Burger, B. J.; Bercaw, J. E. in *Experimental Organometallic Chemistry*, (Eds: A. L. Wayda, M. Y. Darensbourg) American Chemical Society, Washington, DC, **1987**, pp 79–98.
(43) Newkome, G. R.; Garbis, S. J.; Majestic, V. K.; Franczek, F. R.; Chiari, G. *J. Org. Chem.*, **1981**, *46*, 833–839.
(44) Bechlars, B.; D'Alessandro, D. M.; Jenkins, D. M.; Iavarone, A. T.; Glover, S. D.; Kubiak, C. P.; Long, J. R. *Nature Chem.*, **2010**, *2*, 362–368.
(45) Gaussian 09, Revision **A.1**, Frisch, M. J.; Trucks, G. W.; Schlegel, H. B.; Scuseria, G. E.; Robb, M. A.; Cheeseman, J. R.; Scalmani, G.; Barone, V.; Mennucci, B.; Petersson, G. A.; Nakatsuji, H.; Caricato, M.; Li, X.; Hratchian, H. P.; Izmaylov, A. F.; Bloino, J.; Zheng, G.; Sonnenberg, J. L.; Hada, M.; Ehara, M.; Toyota, K.; Fukuda, R.; Hasegawa, J.; Ishida, M.; Nakajima, T.; Honda, Y.; Kitao, O.; Nakai, H.; Vreven, T.; Montgomery, Jr., J. A.; Peralta, J. E.; Ogliaro, F.; Bearpark, M.; Heyd, J. J.; Brothers, E.; Kudin, K. N.; Staroverov,

V. N.; Kobayashi, R.; Normand, J.; Raghavachari, K.; Rendell, A.; Burant, J. C.; Iyengar, S. S.; Tomasi, J.; Cossi, M.; Rega, N.; Millam, J. M.; Klene, M.; Knox, J. E.; Cross, J. B.; Bakken, V.; Adamo, C.; Jaramillo, J.; Gomperts, R.; Stratmann, R. E.; Yazyev, O.; Austin, A. J.; Cammi, R.; Pomelli, C.; Ochterski, J. W.; Martin, R. L.; Morokuma, K.; Zakrzewski, V. G.; Voth, G. A.; Salvador, P; Dannenberg, J. J.; Dapprich, S.; Daniels, A. D.; Farkas, Ö.; Foresman, J. B.; Ortiz, J. V.; Cioslowski, J.; Fox, D. J. Gaussian, Inc., Wallingford CT, **2009**.

(46) Chai, J.-D. and Head-Gordon, M. *Phys. Chem. Chem. Phys.*, **2008**, *10*, 6615–6620.

(47) Dunning Jr., T. H. *J. Chem. Phys.*, **1989**, *90*, 1007–1023.

(48) Balabanov, N. B.; Peterson, K. A. *J. Chem. Phys.*, **2005**, *123*, 064107.

(49) Humphrey, W.; Dalke, A.; Schulten, K. *J. Molec. Graphics*, **1996**, *14*, 33–38.

(50) AIMAll (Version 11.06.19), Todd A. Keith, TK Gristmill Software, Overland Park KS, USA, **2011**.

Chapter 4

Immobilization and Water Oxidation Catalysis of the Ruthenium Blue Dimer $[(Ru(bpy)_2(H_2O))_2(\mu\text{-}O)][ClO_4]_4$ on Mesoporous Silica

Introduction

Artificial photosynthesis is a current area of active research in the field of renewable energy. This concept targets the development of devices that convert solar energy to chemical energy, commonly *via* the splitting of water into hydrogen and oxygen gas. Currently, a significant limitation of this process is the efficiency of the half-reaction for the oxidation of water (eq 1).

$$2H_2O \longrightarrow O_2 + 4H^+ + 4e^- \quad (1)$$

This reaction requires the transport of four electrons and protons, coupled with the breaking of four oxygen-hydrogen bonds and the formation of an oxygen-oxygen bond. It is further complicated by the endothermic nature of water oxidation, a reaction requiring a half-cell potential of E^O = +1.23 V *vs.* NHE at pH 0. Thus, few water oxidation catalysts have been developed and the incorporation of these catalysts into devices for artificial photosynthesis remains a challenge.[1,2]

A number of heterogeneous catalysts have been developed for water oxidation. Several precious metal oxides have been shown to be efficient catalysts, including RuO_2, IrO_2, and PtO_2; however, these systems suffer from the high cost of these metals.[3–9] Recently, significant progress has been made with electrocatalytic cobalt oxide systems which operate at a relatively low overpotential under mild pH conditions.[10–14] However, these materials suffer from the difficulty of mechanistic analysis and device incorporation. Alternative catalysts might be based on molecular structures, which could permit efficient utilization of catalytic centers, given appropriate dispersion of the catalyst onto a high surface area support. In addition, synthetic methodologies allow systematic variation of the catalytic center to optimize performance.[2] However, molecular systems often degrade in the extreme oxidative environments required for water oxidation. To date, the most effective molecular platforms for water oxidation catalysis, in terms of catalytic activity and stability, are the ruthenium-polypyridine dimers of the type first reported by Meyer and coworkers.[15–17] Over the past 25 years, work by Meyer[18–23], Hurst[24–29], and others[30–32] has focused on studies of the structure and mechanism of water oxidation for one of the first molecular catalysts reported, the "ruthenium blue dimer" $[Ru(bpy)_2(H_2O)]_2(\mu\text{-}O)[ClO_4]_4$ (Figure 1).

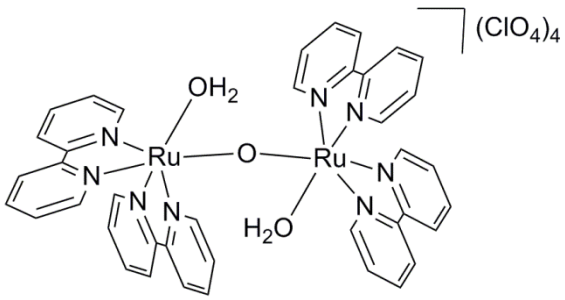

Figure 1. Structure of $[(Ru(bpy)_2(H_2O))_2(\mu\text{-}O)][ClO_4]_4$.

For use of these catalysts in a photochemical cell, it is necessary to attach the catalysts onto the surface of a photoactive material and to promote a heterogeneously catalyzed water oxidation. This problem has been addressed by the Meyer group, by attachment of ancillary phosphate groups to ruthenium polypyridyl systems followed by deposition onto titania.[33–36] In

this case, the ancillary phosphate groups bind to the surface of titania and are necessary for the deposition of the catalyst onto the surface. For the ruthenium blue dimer complex, Yagi *et al.*[37] studied water oxidation catalysis with the catalyst absorbed into a Nafion membrane. In the research described here, adsorption of the ruthenium blue dimer onto the high surface area, mesoporous silica material SBA-15 is described. The structure of the adsorbed catalyst is analyzed using a variety of spectroscopic and analytical means including DRUV-Vis, DRIFTS, and Raman spectroscopy. The performance of the immobilized catalyst in water oxidation is also described.

Results and Discussion

Synthesis of Ruthenium Complexes. In earlier work, the ruthenium blue dimer was obtained as the perchlorate salt, $[(Ru(bpy)_2(OH_2))_2(\mu\text{-}O)][ClO_4]_4\cdot 2H_2O$ (**3**).[15,18] In synthetic investigations with this compound, use of the alternative counteranions BF_4^- and PF_6^- was explored. The tetrafluoroborate salt $[(Ru(bpy)_2(OH_2))_2(\mu\text{-}O)][BF_4]_3[NO_3]\cdot 4H_2O$ (**1**) was prepared by the same method as that reported for **3**,[18] but a saturated aqueous solution of $NaBF_4$, rather than $NaClO_4$, was used to precipitate the ruthenium complex. Subsequent crystallizations utilized aqueous HBF_4 solutions. In our hands, the tetrafluoroborate salt **1** was found to be preferable for a number of reasons. First, **1** was isolated in higher yields after four recrystallizations (24%) compared to that of the corresponding similarly prepared perchlorate salt, and forms more crystalline product having a higher solubility in water. In addition, tetrafluoroborate salts avoid the potential explosive hazards associated with perchlorate. For these reasons, **1** was used throughout the experiments described below. The mixed-valent $Ru^{III}Ru^{IV}$ salt $[(Ru(bpy)_2(OH_2))_2(\mu\text{-}O)][BF_4]_4[NO_3]\cdot 3H_2O$ (**2**) could be prepared from **1**, in a manner analogous to that reported for the perchlorate salt $[(bpy)_2(H_2O)Ru^{III}(\mu\text{-}O)Ru^{IV}(OH)(bpy)_2][ClO_4]_4\cdot 3H_2O$ (**4**), by addition of one equivalent of $(NH_4)_2Ce(NO_3)_6$.

The crystal structure of **1** (Figure 2) was determined for comparison with the reported crystal structure of **3**.[1] Relevant geometrical parameters for **1** are compared to those of **3** in Table 1. The bond parameters are very similar for **1** and **3**; however, the C_2 symmetry observed for **3** is not present and the space group symmetry is reduced from C2/c to $P2_1/n$. The structure contains a pseudo-rotation axis through the O1 atom, with atomic positions deviating by 0.3 Å (ave) from C_2 symmetry for all related atoms. The crystal structure of **2** was also determined, and is shown in Figure 3. This complex can be compared to the similar crystal structure of the perchlorate salt $[(bpy)_2(H_2O)Ru^{III}(\mu\text{-}O)Ru^{IV}(OH)(bpy)_2][ClO_4]_4\cdot 3H_2O$ (**4**) previously determined (Table 1).[38] While in **4** the Ru(III) and Ru(IV) centers have slightly different ligand sets such that the Ru(III) center is bound to a terminal aqua ligand while the Ru(IV) center is bound to a terminal hydroxo ligand, the ligand sets of the Ru(III) and Ru(IV) centers in **2** are identical. This results in crystallographically indistinguishable Ru(III) and Ru(IV) centers that are, related by a C_2 axis. Ru–N and Ru–O1 bond lengths of **2** are similar to the Ru–N and Ru–O1 bond lengths of the aqua-bound ruthenium center of **4**, considering the relatively high uncertainty in the bond lengths of **4**, and the Ru–O1–Ru angles are indistinguishable. One major difference between the two structures is the O–Ru–Ru–O torsion angle between the bond vectors of the terminal aqua or hydroxo ligands. The O–Ru–Ru–O torsion angle of 117.2(7)° in **4** is significantly larger than the O–Ru–Ru–O torsion angle in **2** (96.2(3)°) indicating that the Ru–O bond vectors twist significantly away from each other once the terminal aqua ligand is deprotonated.

Curiously, crystals of **1** and **2** contain one nitrate anion that persists through multiple recrystallizations in the presence of HBF_4. This suggests that there is a preferential interaction between the nitrate anion and the complex cation. However, in the solid state this interaction is purely ionic in nature, and no short contacts involving this anion are apparent. Attempts to remove the nitrate ion by substituting $AgNO_3$ with $AgBF_4$ in the synthesis were unsuccessful.

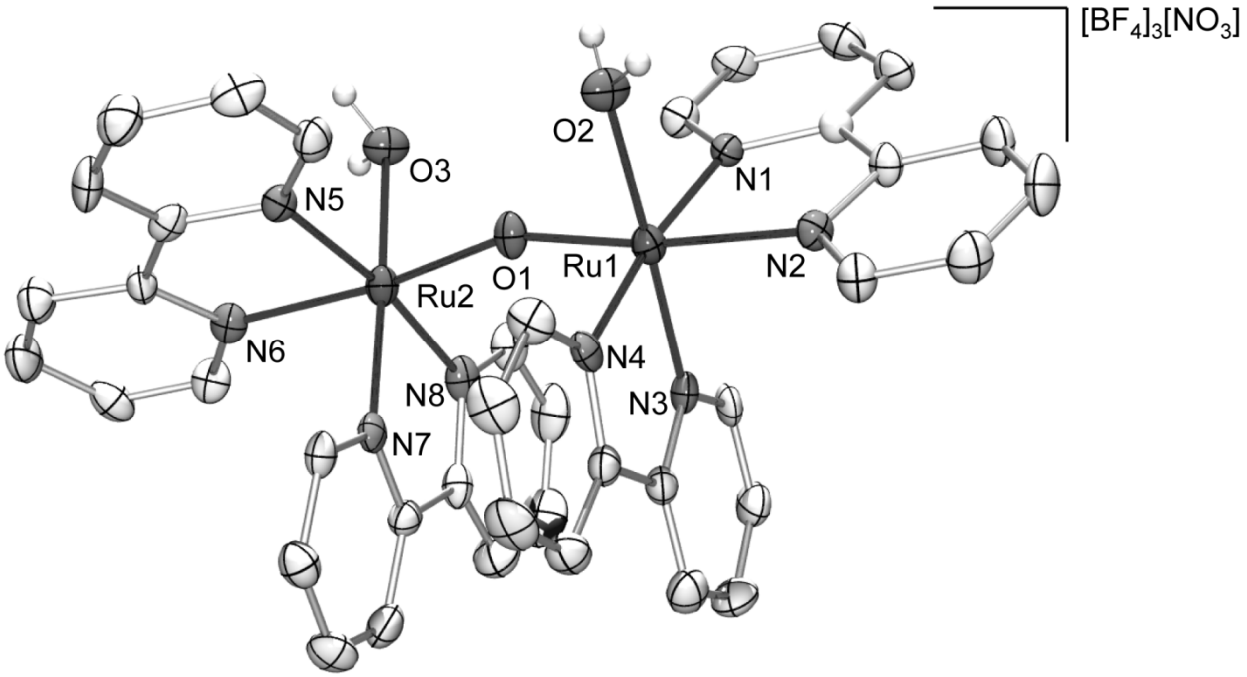

Figure 2. Molecular structure of the cation in **1**, $[(Ru(bpy)_2(H_2O))_2(\mu\text{-}O)][BF_4]_3[NO_3]\cdot 4H_2O$. Thermal ellipsoids are shown at 50% probability; anions, solvent water molecules, and bpy hydrogen atoms have been omitted for clarity.

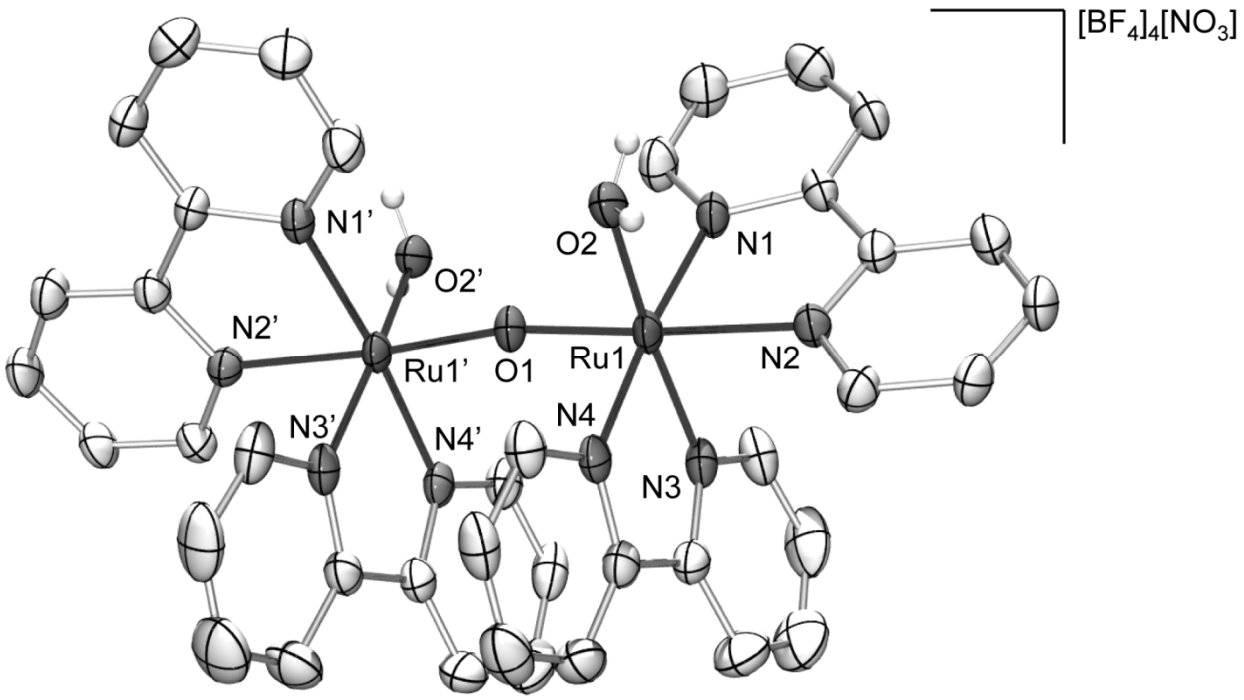

Figure 3. Molecular structure of the cation in **2**, $([Ru(bpy)_2(H_2O)]_2(\mu\text{-}O))(BF_4)_4(NO_3)\cdot 3H_2O$. Thermal ellipsoids are shown at 50% probability; anions, solvent water molecules, and bpy hydrogen atoms have been omitted for clarity.

Table 1. Comparison of Bond Parameters of **1** and **2** with **3**[2] and **4**[3].

	1	**3**	**2**	**4**
Ru-O1	1.869(4) Å[a]	1.869(1) Å	1.845(1) Å	1.847(12), 1.823(12) Å[b]
Ru-N1	2.091(5) Å[a]	2.089(4) Å	2.082(4) Å	2.072(15), 2.085(14) Å[b]
Ru-N2	2.059(6) Å[a]	2.046(5) Å	2.081(4) Å	2.053(13), 2.105(13) Å[b]
Ru-N3	2.018(6) Å[a]	2.029(5) Å	2.059(4) Å	2.019(14), 2.122(14) Å[b]
Ru-N4	2.045(6) Å[a]	2.059(4) Å	2.059(4) Å	2.100(14), 2.059(15) Å[b]
Ru-O2	2.116(4) Å[a]	2.136(4) Å	2.067(4) Å	2.148(11), 1.978(14) Å[b]
Ru-O1-Ru	157.29(17)°	165.4(3)°	169.5(3)°	170.0(7)°
O2-Ru1-Ru2-O3[c]	63.57(13)°	65.7(2)°	96.2(3)°	117.2(7)°

[a] Average of pseudo-symmetry related pairs. [b]The first distance given is for the Ru–OH_2 ruthenium center; the second is for the Ru–OH ruthenium center. [c]In **3** and **4**, O3 = O2'.

Synthesis of Ru_2O-SBA15-OH and Ru_2O-SBA15 materials. Immobilization of **1** onto SBA15 was accomplished by addition of 0.500 g of SBA15 to aqueous solutions of 5 mg and 10 mg of **1** (eq 1). The resulting mixture was stirred for 16 h to produce grafted materials **Ru_2O-SBA15-OH-1** and **Ru_2O-SBA15-OH-2**, respectively, which were collected by centrifugation and washing with 150 mL of water. These materials have a light blue color attributed to deposition of **1** onto the surface. This color does not leach from the material when it is washed with water.

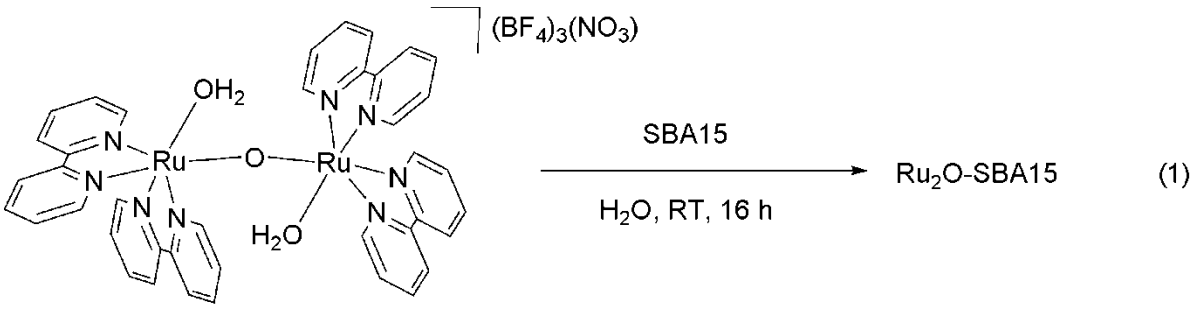

The mass percentage of ruthenium deposited onto SBA15 was measured using inductively coupled plasma mass spectrometry (ICP-MS) and compared to the maximum percentage of ruthenium expected. The results indicate that less than 40% of the complex grafts onto the surface even though a relatively small amount of **1** is being added to the reaction (Table 2). The remainder of the complex remains in solution, as determined by UV-vis spectra of the mixture supernatant. This low surface coverage prompted interest in development of alternative immobilzation strategies that increase the amount of grafted complex.

Table 2. Adsorption of **1** onto SBA15.

	1 (mg)	maximum wt% Ru	adsorbed wt% Ru	% adsorbed
Ru2O-SBA15-OH-1	5	0.16	0.058(6)	36
Ru2O-SBA15-OH-2	10	0.31	0.076(5)	25

It was hypothesized that the deposition of **1** onto SBA15 occurs by Strong Electrostatic Adsorption, so that the cation of **1** adsorbs onto SBA15 as the counterion of basic sites on the surface of SBA15 (deprotonated silanol groups).[39] Thus, it seemed that improved adsorption could be achieved by increasing the number of basic sites on SBA15 by deprotonation of the surface silanol groups. For the grafting experiments described below, SBA15 was made basic by stirring the material in concentrated aqueous NH_4OH for 10 min and then washing with 150 mL of water prior to the addition of **1**. A summary of these experiments is given in Table 3 and shown in Figure 4.

Table 3. Adsorption of **1** onto basic SBA15.

	1 (mg)	maximum wt% Ru	adsorbed wt% Ru	% adsorbed
Ru2O-SBA15-1	5	0.16	0.165(11)	>95
Ru2O-SBA15-2	10	0.31	0.31(2)	>95
Ru2O-SBA15-3	25	0.77	0.74(5)	>95
Ru2O-SBA15-4	50	1.49	1.27(9)	85
Ru2O-SBA15-5	100	2.8	1.76(12)	63

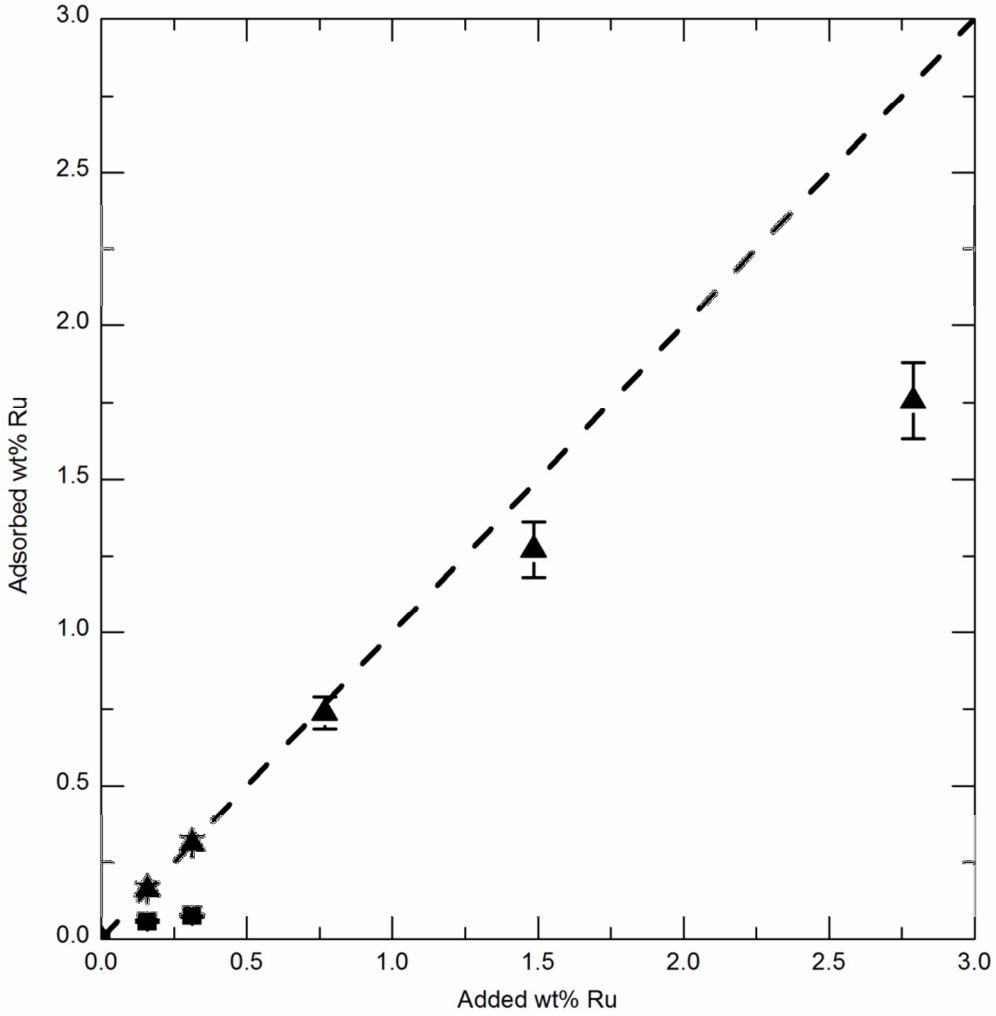

Figure 4. Observed weight percent of ruthenium on SBA15 versus the total amount of **1** added during the synthesis. (■) Samples of **Ru_2O-SBA15-OH**. (▲)Samples of **Ru_2O-SBA15**.

As expected, the use of basic SBA15 greatly increased the amount of ruthenium grafted on the surface. For the experiments with SBA15 less than 40% of the ruthenium added is deposited onto the surface, whereas with basic SBA15, all of the ruthenium is deposited onto the surface up to 0.77 wt% Ru addition.. Higher surface loadings can be realized when the amount of **1** added to the reaction is increased, resulting in a highest observed deposition of 1.76(12) wt% Ru representing 63% of the amount of **1** added.

Characterization of Ru_2O-SBA15. Analysis of the effect of the deposition of **1** on the surface characteristics of SBA15 in the **Ru_2O-SBA15** materials was conducted by nitrogen physisorption and TEM (Figure 5, 6, Table 4). The surface area of **Ru_2O-SBA15** is significantly reduced to 400 m^2/g or less from the surface area of SBA15 measured at 623(14) m^2/g. This effect is primarily attributed to the pre-treatment of SBA15 with NH_4OH which reduces the surface area to 440(40) m^2/g. The mesoporous structure of SBA15 is maintained through deposition as demonstrated by the Type IV isotherms exhibited in the nitrogen physisorption data and the presence of channels in the TEM images.[40] By comparing the surface concentration

of silanol groups in SBA15 with the surface concentration of ruthenium on the **Ru_2O-SBA15**, it can be determined that up to 54% coverage of all potential basic sites on SBA15 can be covered with the $[Ru_2O]^{4+}$ cation of **1**.

Table 4. Surface area, and silanol and ruthenium surface concentration.

	wt% Ru	S_{BET}	[-OH] (nm^{-2})	[Ru] (nm^{-2})[a]	2[Ru]/4[-OH] (%)
SBA15	-	623(14)	1.3(3)	-	-
Ru2O-SBA15-0	-	440(40)	-	-	-
Ru2O-SBA15-3	0.74(5)	400(40)	-	0.12(3)	18
Ru2O-SBA15-4	1.27(9)	390(40)	-	0.22(5)	34
Ru2O-SBA15-5	1.76(12)	330(30)	-	0.35(8)	54

[a]Adjusted for hydration level (10 wt% by TGA)

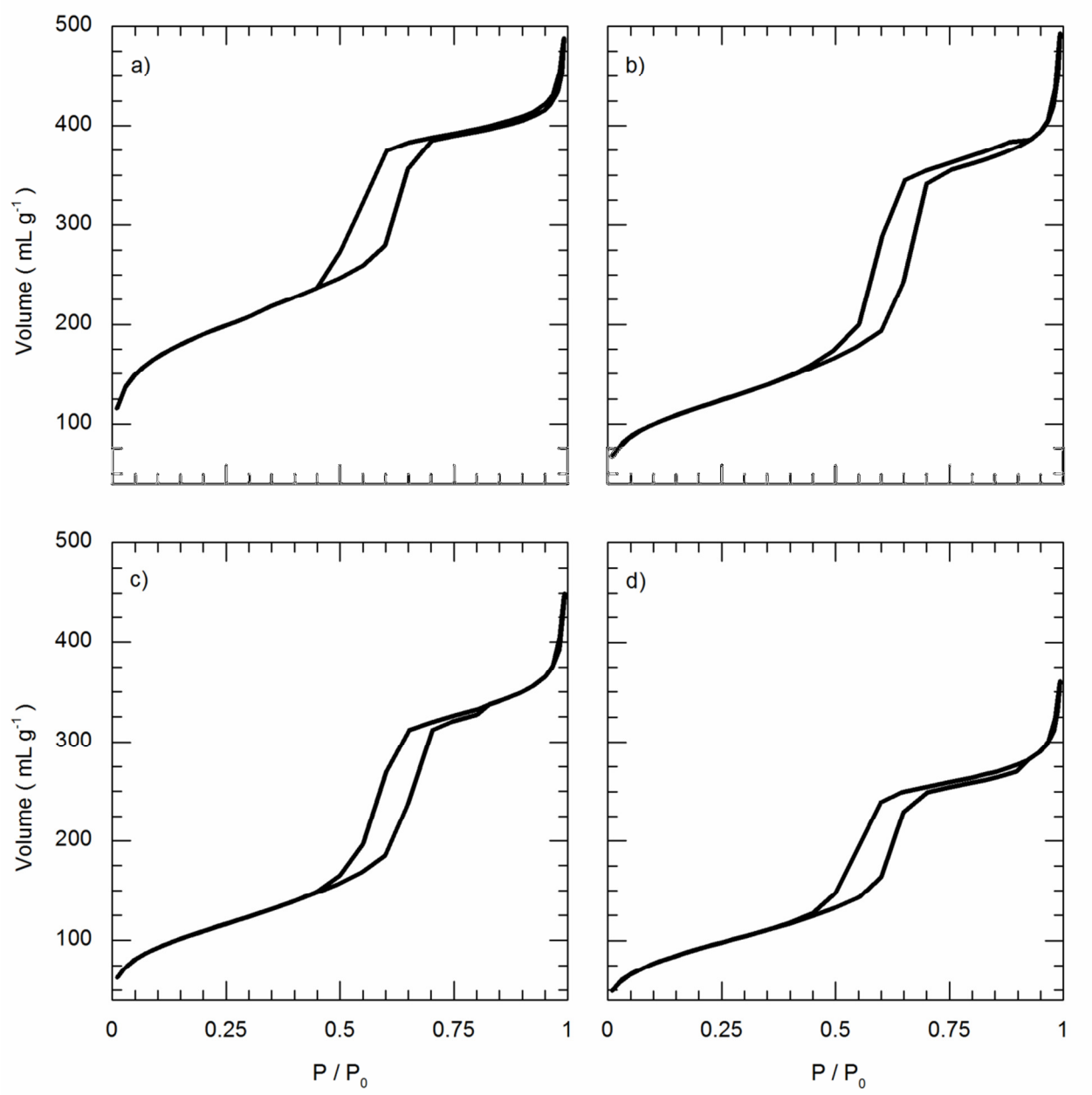

Figure 5. Nitrogen adsorption-desorption isotherms for a) SBA15, b) **Ru_2O-SBA15-3**, c) **Ru_2O-SBA15-4**, and d) **Ru_2O-SBA15-5**.

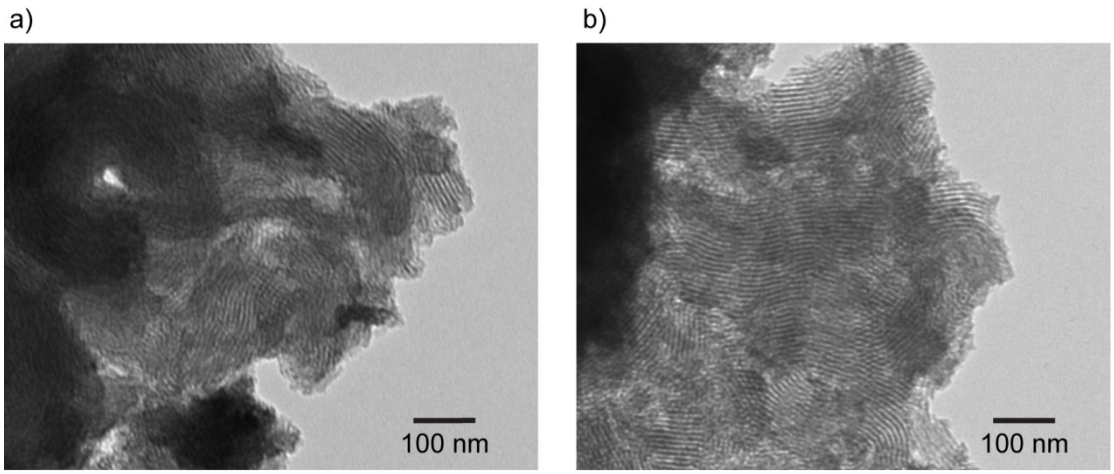

Figure 6. Representative TEM images with a) SBA15, and b) **Ru_2O-SBA15-5**.

To determine the nature of the ruthenium-containing species on **Ru_2O-SBA15**, the **Ru_2O-SBA15** materials were investigated by a number of methods: Diffuse Reflectance UV-vis Spectroscopy (DRUV-vis), Diffuse Reflectance Infrared Fourier-Transform Spectroscopy (DRIFTS), Raman Spectroscopy, and Elemental Analysis. Compound **1** has a strong absorption in the visible region attributed to an MLCT band at 637 nm. Because SBA15 does not absorb light in the UV-vis region, **Ru_2O-SBA15** was analyzed by DRUV-vis spectroscopy and observed absorptions are attributed to ruthenium-containing species on the surface. As shown in Figure 7, the DRUV-Vis spectrum exhibits absorption peaks at 653 and 476 nm. The band at 653 nm corresponds well to the MLCT band of **1**, although with a significant bathochromic shift attributed to the influence of the polarity of the silica. The absorption at 476 nm is attributed to the presence of the Ru^{III}/Ru^{IV} cation of **2** on the surface, which has an MLCT absorption at 444 nm. The presence of this absorption indicates oxidation by atmospheric oxygen of the ruthenium dimer cation during the deposition process.

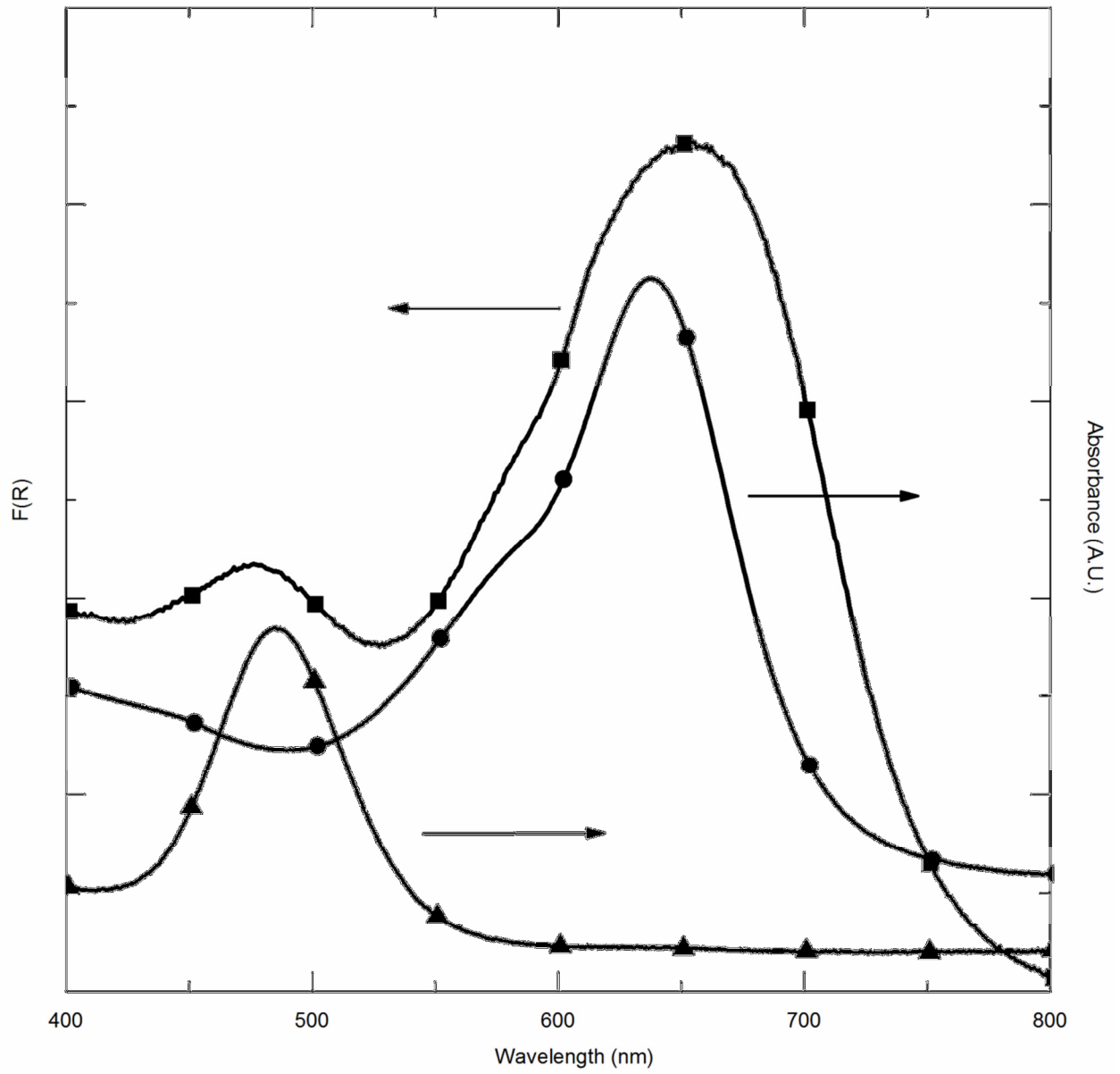

Figure 7. DRUV-Vis spectrum of **Ru_2O-SBA15** with the absorption spectra of **1** and **2** for comparison. (■) **Ru_2O-SBA15-3**, (●) **1**, (▲) **2**.

The DRIFTS spectrum of **Ru_2O-SBA15** materials is shown in Figure 8 and compared to the IR spectrum of **1**. Due to the strong absorbance peaks of silica centered around 1345, 1080, and 999 cm^{-1}, most of the absorbance peaks for **1** are obscured. However, subtracting a spectrum of pure SBA15 from the spectrum of the **Ru_2O-SBA15** with the highest concentration of ruthenium species, **Ru_2O-SBA15-5**, clearly indicates that peaks at 1605 and 1450 cm^{-1} are present. These peaks are attributable to vibrations within the bipyridine rings of **1** and are consistent with the presence of **1** on the surface. Infrared spectroscopy can also indicate whether the tetrafluoroborate and nitrate anions are present on the surface. The anions have characteristic absorptions at 1060 and 521 cm^{-1} for tetrafluoroborate, and 804 and 1388 cm^{-1} for nitrate. These

absorption peaks are absent from the DRIFTS spectrum of **Ru_2O-SBA15** materials. However, the strongest of these absorption peaks, at 1060 cm^{-1}, is obscured by the strong silica absorption at 1080 cm^{-1} while the other peaks are weak and difficult to definitively identify due to the relatively small amount of **1** present in the sample.

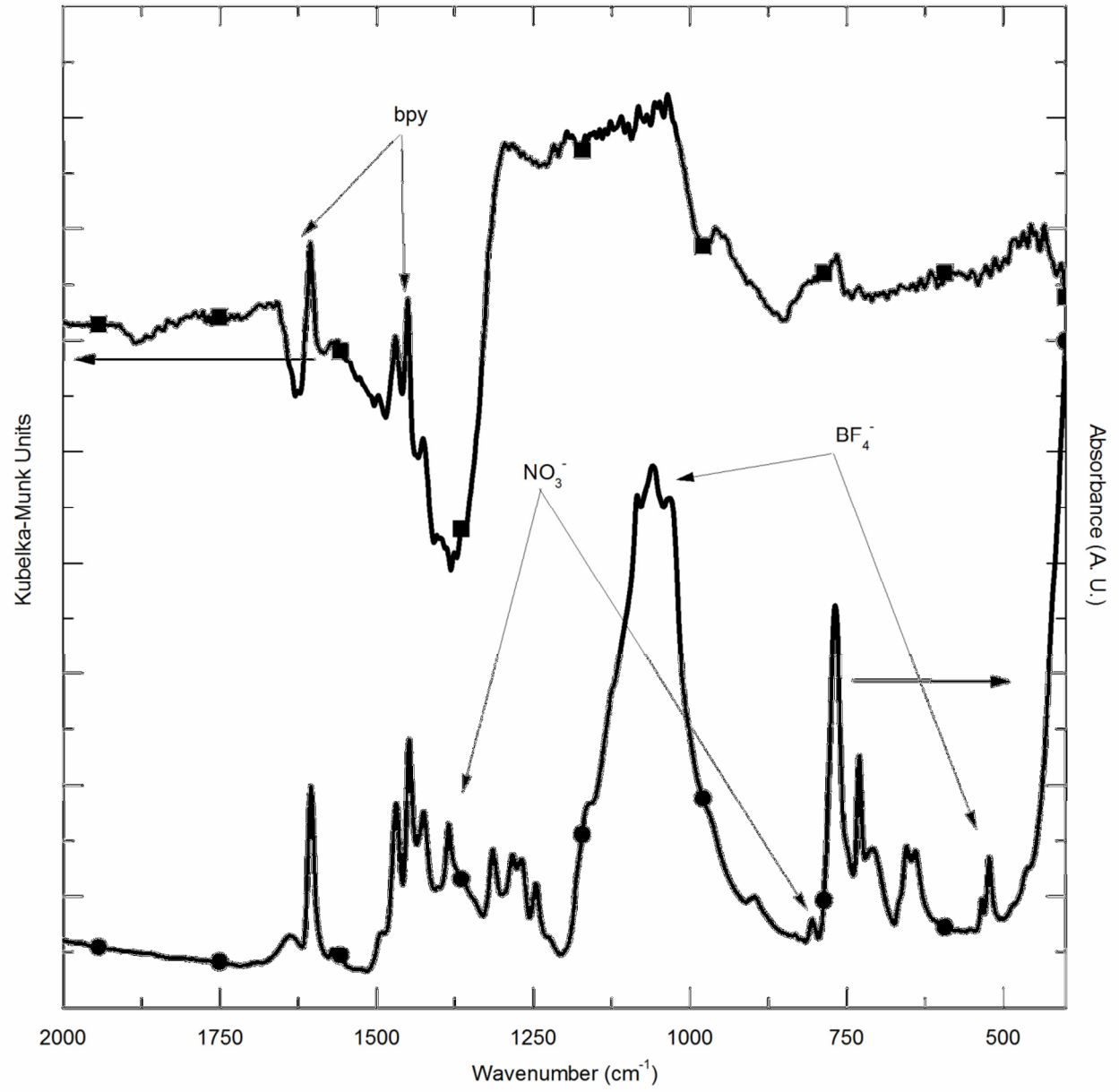

Figure 8. Comparison of the DRIFTS spectrum of **Ru_2O-SBA15** with the IR absorbance spectrum of **1**, (■) **Ru_2O-SBA15-5**, (●) **1**.

The Raman spectra of **Ru_2O-SBA15** very clearly correlate with the Raman spectrum of **1** (Figure 9). Particularly, the peak at 374 cm^{-1} is characteristic of the ν_s Ru-O-Ru stretch.[26] The only significant differences between the two spectra are the three peaks centered at 745 cm^{-1} present in **Ru_2O-SBA15**. These peaks might arise from interaction of the complex with the silica surface via a Ru-O-Si symmetric stretch from possible substitution of an aqua ligand of **1** with a surface siloxide site.[41]

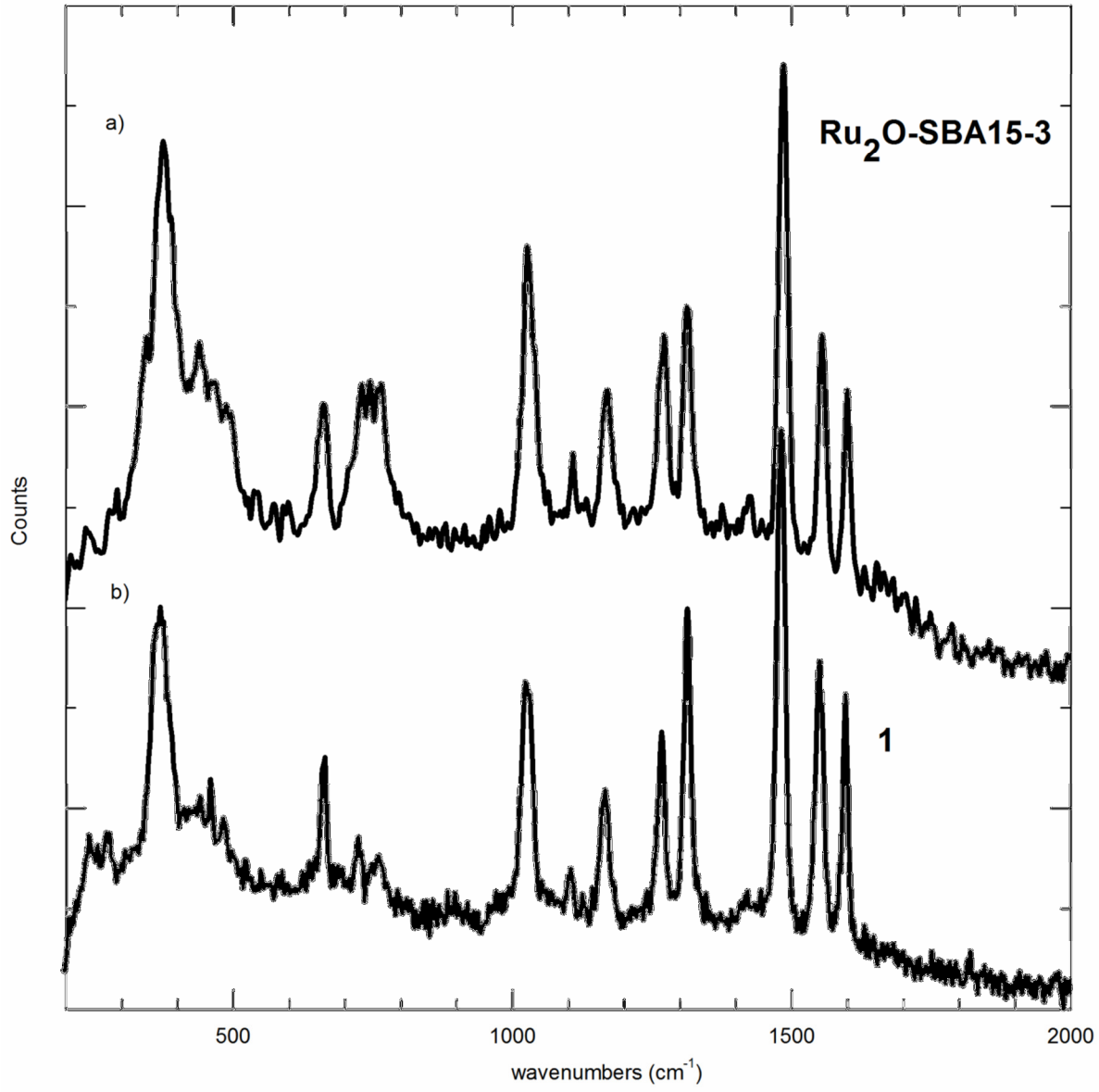

Figure 9. Comparison of the Raman spectrum of **Ru_2O-SBA15-3** with **1**. a) Ru_2O-SBA15, b) **1**.

The previous spectroscopic analyses provide strong evidence for the presence of the ruthenium dimer cation of **1** on the surface of the grafted materials **Ru_2O-SBA15** (Figure 10). This is supported by elemental analyses of carbon and nitrogen which are consistent with the amount of ruthenium found on the surface (Table 5). However, these spectroscopic techniques do not adequately prove the absence of tetrafluoroborate or nitrate ions. To this end, fluorine elemental analysis using ICP-MS determined, to a detection limit of 0.02%, that no fluorine was present. On the basis of this accumulated data, there is no indication of decomposition of the ruthenium dimer cation to any species other than the oxidized Ru^{III}/Ru^{IV} dimer cation, and only the ruthenium dimer cation deposits onto the surface, held onto the surface by Strong Electrostatic Adsorption.

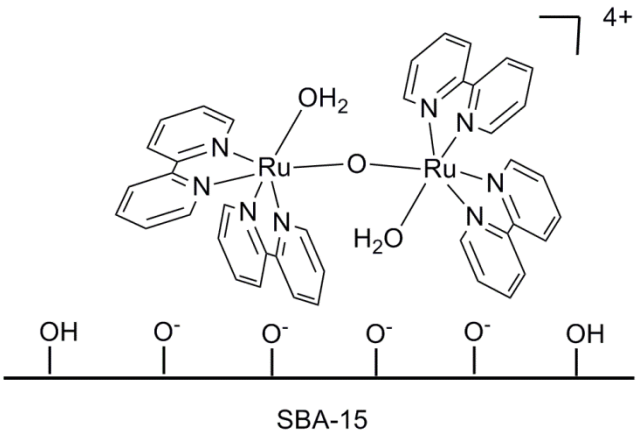

Figure 10. Adsorption of the ruthenium blue dimer cation onto SBA-15.

Table 5. Carbon and nitrogen elemental analyses compared to ruthenium analysis.

	wt% Ru	% C expected[a]	% C found	% N expected[a]	% N found
Ru2O-SBA15-3	0.74(5)	1.8	1.8(3)	0.41	0.5(3)
Ru2O-SBA15-4	1.27(9)	3.0	3.1(3)	0.70	0.9(3)
Ru2O-SBA15-5	1.76(12)	4.2	4.5(3)	0.98	1.2(3)

[a]Based on carbon and nitrogen to ruthenium ratios for the ruthenium dimer cation.

Water Oxidation Activity of Ru_2O-SBA15. Ru_2O-SBA15 was analyzed for water oxidation activity using a 0.9 M aqueous solution of $(NH_4)_2Ce(NO_3)_6$ as a sacrificial oxidant. The initial turnover frequency (TOF_i) was determined using a fluorescent oxygen probe inserted into the headspace of the reaction vessel. Oxygen evolution was measured over the course of one hour (Figure 11). The rate of oxygen evolution is linear over the first 5-15 min of the experiment, after which the rate decreases substantially. The TOF_i was measured from the linear portion of the oxygen evolution during the first 10 min of the experiment (Table 6). In comparison to water oxidation by aqueous solutions of **1**, the TOF_i is significantly reduced on deposition of the complex onto SBA15, to nearly 10% of the rate of **1**.

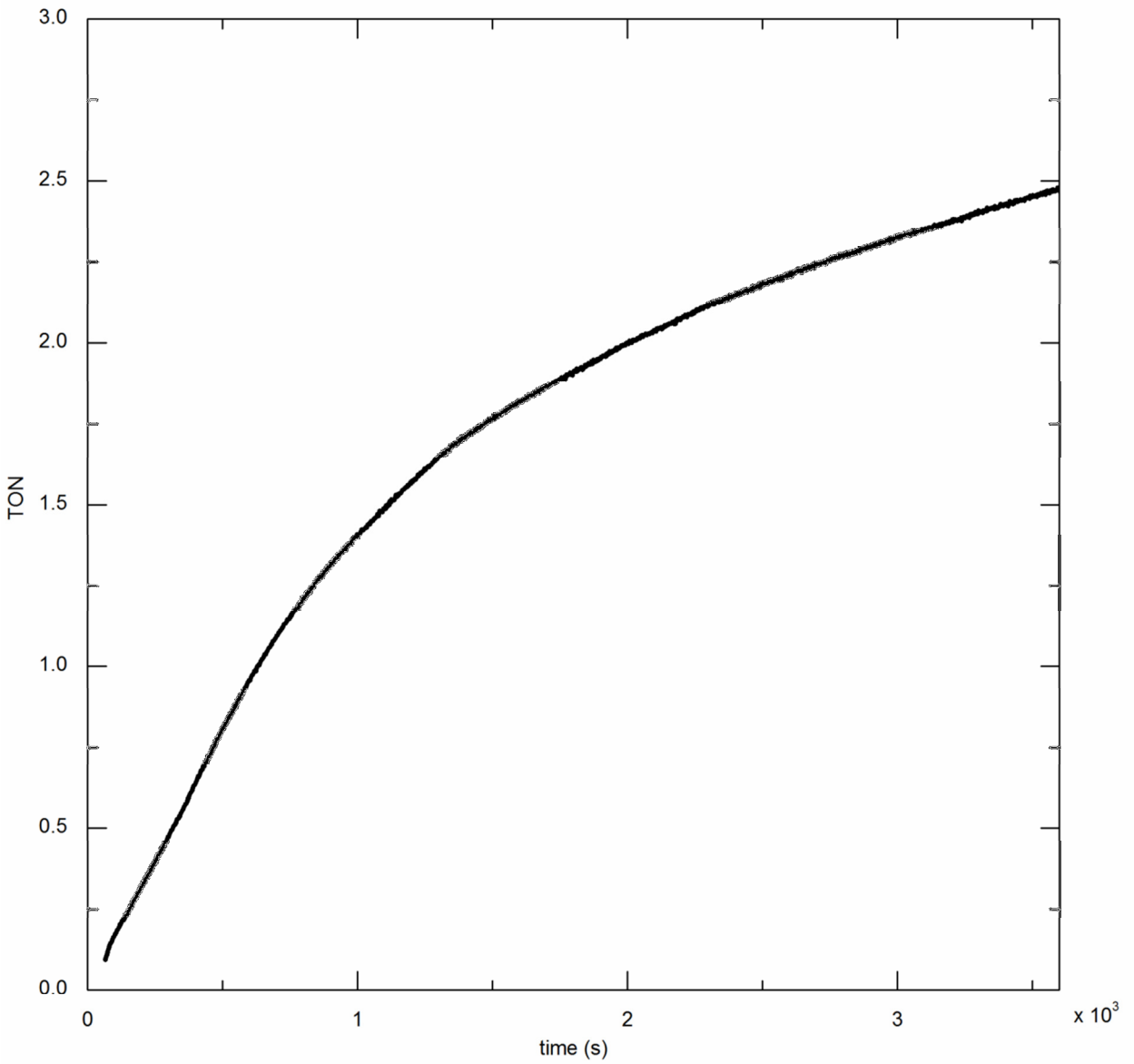

Figure 11. Representative fluorescent oxygen probe data of water oxidation with **Ru_2O-SBA15-3**.

Table 6. Summary of water oxidation experiments.

	TOF_i (hr^{-1})[a]	TON (1 day)
1	29(13)	10(1)
Ru2O-SBA15-3	4(2)	-
Ru2O-SBA15-4	3(1)	5(1)
Ru2O-SBA15-5	4(1)	6(1)

[a]Linear portion of the oxygen evolution rate in the initial 10 min.

Longer term water oxidation activity of **Ru_2O-SBA15** was measured over a period of 24 h. The total oxygen evolution over this period was measured by sampling of the headspace of a sealed reaction vessel using gas chromatography (Table 6). The amount of O_2 evolution measured after 24 h is consistent with the significant decrease in oxygen evolution rate after the initial 10 min of the experiment, as measured by the fluorescent oxygen probe. Due to the large excess of oxidant added, loss of catalysis over time is not due to the consumption of oxidant. As indicated by Meyer *et al.*, loss of catalysis may be due to substitution of available anions for the aqua ligands of **1**.[19]

Characterization of Ru_2O-SBA15 after oxidation. Oxidized samples of **Ru_2O-SBA15-3** and **Ru_2O-SBA15-5** materials were collected by filtration. These post-oxidation materials were then analyzed by DRUV-vis and Raman spectroscopy to determine the species present on the surface after water oxidation. The DRUV-vis spectrum (Figure 12) exhibits oxidation of a majority of the complex to the one-electron oxidation product. This is expected, since this species is part of the oxidation pathway of **1** and is stable under ambient conditions. The Raman spectrum of **Ru_2O-SBA15-3** (Figure 12) has only one major difference with the spectrum of Ru_2O-SBA15 before water oxidation. Instead of three peaks centered around 745 cm^{-1}, only a single peak at 764 cm^{-1} is seen. This is consistent with the hypothesis that these peaks are due to interactions of the adsorbed complex with the surface. During the catalytic cycle it is expected that the aqua site of the complex could react with the surface, which would account for the change in this region of the spectrum.

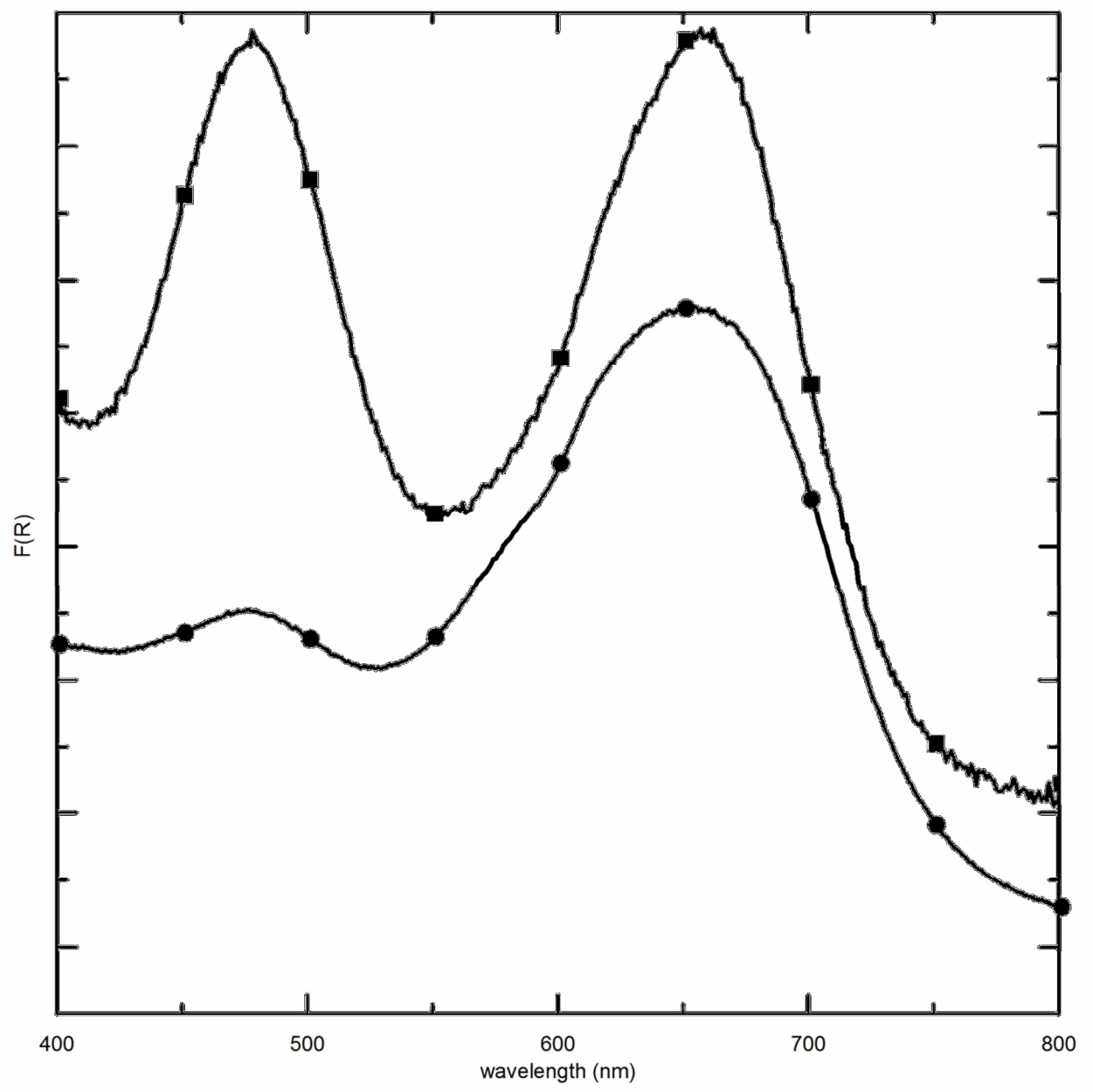

Figure 12. Comparison of DRUV-vis of **Ru_2O-SBA15-3** before (●) and after (■) water oxidation. Spectra are offset for clarity.

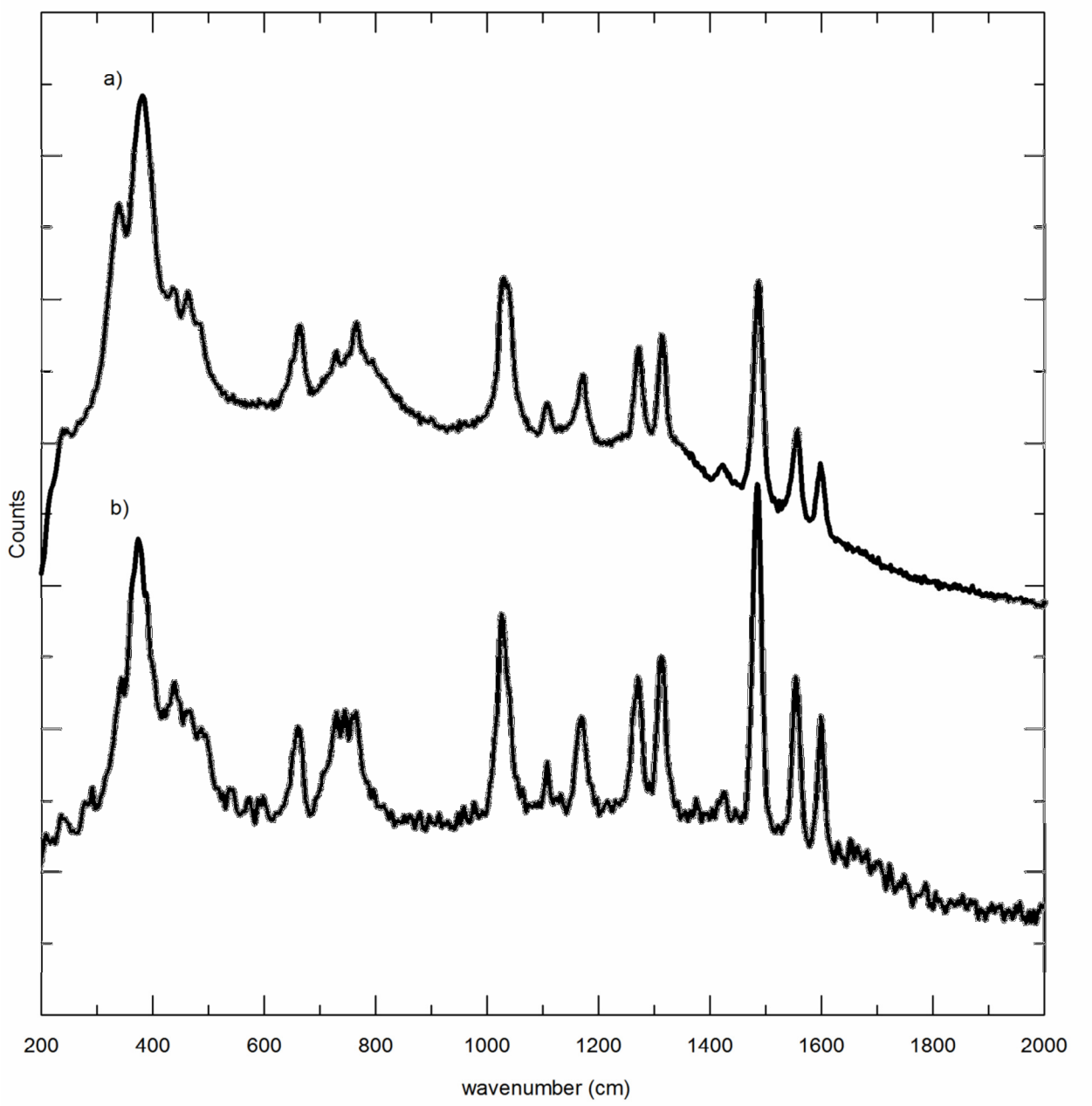

Figure 13. Comparison of the Raman spectra of **Ru_2O-SBA15-3** a) after water oxidation compared with b) before. Spectra are offset for clarity.

Ruthenium analysis of the materials after water oxidation shows that not all of the complex remains adsorbed to the surface with a measured decrease from 1.76(12) % Ru to 0.81(8) % for **Ru_2O-SBA15-5** and a decrease from 0.74(5) % Ru to 0.23(2) % for **Ru_2O-SBA15-3**. However, UV-vis analysis of the supernatant of the reaction shows that little, if any, of the complex is identifiable in solution, although this analysis is hampered by the strong absorption of $(NH_4)_2Ce(NO_3)_6$ in solution. Also, the supernatant shows no significant further

water oxidation activity when fresh $(NH_4)_2Ce(NO_3)_6$ solution is added. On the other hand, recycling of the spent catalyst induces partial recovery of catalytic activity.

Conclusion

This work demonstrates the deposition of the ruthenium blue dimer onto SBA-15 by Strong Electrostatic Adsorption. The complex was deposited onto the surface up to a level of 1.76(12) wt% Ru. The adsorbed complex could be identified on the surface by analytical methods. Catalysis of water oxidation by the ruthenium blue dimer is significantly diminished when deposited on the surface. After catalysis, characterization of the resulting oxidized material showed that the complex remained the only identifiable species on the surface, though the amount of the complex present on the surface was significantly diminished. These results demonstrate the capability of Strong Electrostatic Adsorption methods for the deposition of the water oxidation catalysts on the surface of oxide materials.

Experimental

General. Water used in analytical experiments was distilled and deionized to a resistivity of 18.2 MΩcm using a Millipore system. Nitrogen adsorption isotherms were obtained using a Quantachrome Autosorb 1, and samples were outgassed at 120 ^{o}C for at least 20 hours prior to measurement. Carbon, hydrogen, and nitrogen analyses were performed by the College of Chemistry microanalytical laboratory at the University of California, Berkeley. Ruthenium, fluorine, and cerium analyses by inductively-coupled plasma optical emission spectroscopy (ICP-OES) methods were performed by Galbraith Laboratories with an estimated error of ± 10%. Samples for transmission electron microscopy (TEM) were prepared by depositing an ethanol suspension of the material onto carbon-coated copper sample holders obtained from Ted Pella, Inc. Transmission electron microscopy was carried out on a Philips CM200 transmission electron microscope operating at 200 kV. Infrared spectra were recorded on Nicolet Nexus 6700 FT-IR and Mattson Instruments Galaxy 3000 spectrometers. Measurements were made at 4.0 cm^{-1} resolution. Transmission IR samples were prepared as KBr pellets. Diffuse Reflectance FT-IR spectroscopy (DRIFTS) samples were prepared as neat sample powders using a Pike Technologies EasyDiff diffuse reflectance accessory. UV-Vis and DRUV-Vis experiments were performed on a Varian Cary 3000 series spectrometer. Magnesium oxide and potassium bromide were used as white standards for diffuse reflectance UV-Vis and DRIFTS measurements, respectively. Raman spectra were recorded using a Kaiser Optical HoloLab series 5000 Raman spectrometer equipped with a Nd:YAG laser frequency-doubled to 532 nm and a Princeton Instruments TEA/CCD detector operated at 233 K. The laser power level was 25 mW, measured at the sample. Spectra were recorded with a resolution of 2 cm^{-1} with 30 accumulations for 1 s each. Samples were pressed into 9 mm diameter wafers at 14 MPa and placed onto a rotating sample holder located within a quartz cell. Samples were diluted with CsI before pressing except for adsorbed SBA15 samples which were pressed neat. Gas chromatography was carried out on a Hewlett-Packard 6890 Series gas chromatograph using a 10' Hayesep Q 80/100 mesh column. For oxygen analysis, the column temperature is held at 208 K for 20 min before increasing to 293 K at 10 K/min. Real-time oxygen analysis was measured with an Ocean Optics multi-frequency phase fluorimeter (MFPF) with FOXY-R and FOSPOR oxygen probes.

Synthesis of materials. The complexes *cis*-$Ru(bpy)_2Cl_2 \cdot 2H_2O$[42] and $([Ru(bpy)_2(H_2O)]_2(\mu\text{-}O))(ClO_4)_4 \cdot 2H_2O$[15,18] were synthesized as described in the literature. *WARNING: Perchlorate salts of transition metal complexes are potentially explosive.*

SBA15. SBA15 was prepared as reported previously.[43] The prepared material used in this work had a surface area of 623(14) m^2/g using the multi-point Brunauer-Emmet-Teller (BET) method,[44] and an average pore radius of 2.8(3) nm by the Barrett-Joyner-Halenda (BJH) method on adsorption data.[45] The surface OH concentration was measured to be 1.3(3) OH nm^{-2} by addition of dibenzyl magnesium and quantification of the evolved toluene by ^{1}NMR spectroscopy.[46]

$([Ru(bpy)_2(H_2O)]_2(\mu\text{-}O))(BF_4)_3(NO_3) \cdot 4H_2O$ (1). Compound **1** was prepared by a method analogous to that for the perchlorate salt.[18] *cis*-$(bpy)_2RuCl_2 \cdot 2H_2O$ (7.1 g, 14 mmol) was dissolved in 200 mL of water and the resulting solution was heated to reflux. Then, $AgNO_3$ (5.9 g, 35 mmol) was added and the solution was refluxed for 30 min. The reaction solution was filtered and the filtrate was refluxed for an additional 30 min. Saturated aqueous $NaBF_4$ (20 mL) was added and the solution volume was reduced to ~20 mL on a rotary evaporator, then cooled in an ice bath under reduced pressure until crystals formed. The crude product was collected by filtration, then recrystallized by slow cooling of a hot water solution (~5 mL) to which was added ~1 mL of aqueous HBF_4 (48%) and collected by filtration. Recrystallization was performed four times to give analytically pure, X-ray quality crystals of **1** (2.1 g, 1.6 mmol, 24%). **EA** Anal. Calcd (%) for $C_{40}H_{44}N_9B_3F_{12}O_{10}Ru_2$ (1273.39 g/mol): C, 37.73; H, 3.48; N, 9.90. Found: C 37.77; H, 3.48; N, 9.94.

$[Ru(bpy)_2(H_2O)]_2(\mu\text{-}O)(BF_4)_4(NO_3) \cdot 3H_2O$ (2). To a solution of **1** (0.50 g, 0.39 mmol) in a minimum of hot water (~2 mL) was added an aqueous solution of $(NH_4)_2Ce(NO_3)_6$ (0.22 g, 0.40 mmol, in 1 mL of water). The resulting solution was stirred for 5 min, and then the product was crystallized on cooling in an ice water bath. The crude product was collected by filtration, then recrystallized by slow cooling of a hot water solution (~1 mL) to which was added ~0.05 mL of aqueous HBF_4 (48%) and collected by filtration. Recrystallization was performed two times to give analytically pure, X-ray quality crystals of **2** (0.20 g, 0.15 mmol, 38%). **EA** Anal. Calcd (%) for $C_{40}H_{42}N_9B_4F_{16}O_9Ru_2$ (1342.19 g/mol): C, 35.80; H, 3.15; N, 9.39. Found: C 35.42; H, 2.78; N, 9.72.

Ru_2O-SBA15-OH materials. To a stirred solution of **1** (5 – 10 mg) in 20 mL of water was added SBA15 (0.50 g). The suspension was stirred at room temperature for 16 h. The prepared **Ru_2O-SBA15-OH** material was collected by filtration, washed with 150 mL water, and dried under lab atmosphere for 16 h.

Ru_2O-SBA15-OH-1: 5 mg of **1**. **EA** (%): sample 1 - Ru, 0.062; C, 0.09; N, not detected; sample 2 – Ru, 0.053; C, 0.06; N, 0.08.

Ru_2O-SBA15-OH-2: 10 mg of **1**. **EA** (%): sample 1 - Ru, 0.076; C, 0.14; N, 0.12; sample 2 – Ru, 0.076; C, 0.180; N, 0.07.

Ru_2O-SBA15 materials. SBA15 (0.50 g) was stirred in 5 mL concentrated aqueous NH_4OH solution for 10 min, then collected by filtration and washed with 150 mL of water. The material was then immediately added to a stirred solution of **1** (0 – 100 mg) in 20 mL of water was added 0.50 g of SBA15. The suspension was stirred at room temperature for 16 h. The prepared **Ru_2O-SBA15** material was collected by filtration, washed with 150 mL water, and dried under lab atmosphere for 16 h.

Ru_2O-SBA15-0: 0 mg of **1**. **EA** (%): sample 1 – C, not detected; N, not detected; sample 2 – C, not detected; N, 0.19. **Surface Area** (BET): 440(40) m^2/g.

Ru_2O-SBA15-1: 5 mg of **1**. **EA** (%): sample 1 – Ru, 0.168; C, 0.47; N, 0.25; sample 2 – Ru, 0.162; C, 0.47; N, 0.20.
Ru_2O-SBA15-2: 10 mg of **1**. **EA** (%): sample 1 – Ru, 0.32; C, 0.86; N, 0.33; sample 2 – Ru, 0.31; C, 0.90; N, 0.36.
Ru_2O-SBA15-3: 25 mg of **1**. **EA** (%): sample 1 – Ru, 0.76; C, 1.85; N, 0.56; sample 2 – Ru, 0.71; C, 1.76; N, 0.51. **Surface Area** (BET): 400(40) m^2/g. **Pore Radius** (BJH): 3.2(6) nm.
Ru_2O-SBA15-4: 50 mg of **1**. **EA** (%): sample 1 – Ru, 1.28; C, 3.30; N, 0.97; sample 2 – Ru, 1.26; C, 2.98; N, 0.85. **Surface Area** (BET): 390(40) m^2/g. **Pore Radius** (BJH): 3.0(6) nm.
Ru_2O-SBA15-5: 100 mg of **1**. **EA** (%): sample 1 – Ru, 1.84; C, 4.47; N, 1.13; sample 2 – Ru, 1.67; C, 4.55; N, 1.17. **Surface Area** (BET): 330(30) m^2/g. **Pore Radius** (BJH): 2.8(3) nm.
Water Oxidation Experiments. To a solution of catalyst in 10 mL of water was added 0.5 mL of a 0.9 M aqueous solution of $(NH_4)_2Ce(NO_3)_6$. For TOF_i experiments, oxygen was measured by the MFPF oxygen probe inserted into the headspace of the sealed reaction vessel. Into an additional port of the reaction vessel was inserted onto the headspace the temperature sensor of the MFPF system. Both solutions were sparged with N_2 prior to combination.

For 24 hr oxygen evolution experiments, both solutions were sparged with He prior to combination. The vessel was sealed and oxygen evolution was monitored by 0.5 mL injections into a GC after 24 hr. Data was corrected for trace oxygen from air based on the measured content of nitrogen.
X-ray Crystallography. Crystals of **1** suitable for single-crystal X-ray analysis were formed by slow crystallization from dilute HBF_4. The X-ray analysis was carried out at the UC Berkeley CHEXRAY crystallographic facility on a Bruker SMART CCD area detector with graphite-monochromated Mo K_α radiation. Crystals were mounted on a Kapton loop with Paratone N hydrocarbon oil and held in a low-temperature N_2 stream during data collection. Frames were collected using ω scans at 0.3° increments with exposures of 10 s. In the process of structure solution it was found that the hydrogens of the solvent water molecules led to unstable solutions. Two of these hydrogens were constrained to bond lengths and angles consistent with water and four of the hydrogens were omitted. Relevant crystallographic data are summarized in Table 1.

Table 7 Experimental details for the X-ray crystal structures of **1** and **2**.

	1	**2**
Chemical formula	$C_{40}H_{44}B_3F_{12}N_9O_{10}Ru_2$	$C_{40}H_{42}B_4F_{16}N_9O_9Ru_2$
Formula Mass	1273.41	1342.21
Crystal system	Monoclinic	Monoclinic
a/Å	11.306(7)	9.782(6)
b/Å	19.002(11)	24.934(14)
c/Å	22.903(14)	21.603(12)
α/°	90.00	90.00
β/°	93.544(8)	93.696(9)
γ/°	90.00	90.00
Unit cell volume/Å^3	4911(5)	5258(5)
Temperature/K	115(2)	154(2)
Space group	$P2_1/n$	$C2/c$
No. of formula units per unit cell, Z	4	4
No. of independent reflections	9457	4730
R_{int}	0.0890	0.0595
Final R_1 values ($I > 2\sigma(I)$)	0.0403	0.0425
Final $wR(F^2)$ values ($I > 2\sigma(I)$)	0.0676	0.0958
Final R_1 values (*all data*)	0.1049	0.0849
Final $wR(F^2)$ values (*all data)*	0.0753	0.1153

References.

(1) Lewis, N. S.; Nocera, D. G. *Proc. Natl. Acad. Sci.* 2006, *103*, 15729–15735.
(2) Hurst, J. K. *Science* 2010, *328*, 315–316.
(3) Harriman, A.; Pickering, I. J.; Thomas, J. M.; Christensen, P. A. *J. Chem. Soc., Faraday Trans. 1* 1988, *84*, 2795–2806.
(4) Kiwi, J.; Grätzel, M. *Angew. Chem. Int. Ed.* 1978, *17*, 860–861.
(5) Kiwi, J.; Grätzel, M. *Angew. Chem. Int. Ed.* 1979, *18*, 624–626.
(6) Mills, A.; McMurray, N. *J. Chem. Soc., Faraday Trans. 1* 1988, *84*, 379.
(7) Beni, G.; Schiavone, L. M.; Shay, J. L.; Dautremont-Smith, W. C.; Schneider, B. S. *Nature* 1979, *282*, 281–283.
(8) Yagi, M.; Tomita, E.; Sakita, S.; Kuwabara, T.; Nagai, K. *J. Phys. Chem. B* 2005, *109*, 21489–21491.
(9) Kuwabara, T.; Tomita, E.; Sakita, S.; Hasegawa, D.; Sone, K.; Yagi, M. *J. Phys. Chem. C* 2008, *112*, 3774–3779.
(10) Kanan, M. W.; Nocera, D. G. *Science* 2008, *321*, 1072–1075.
(11) Lutterman, D. A.; Surendranath, Y.; Nocera, D. G. *J. Am. Chem. Soc.* 2009, *131*, 3838–3839.
(12) Surendranath, Y.; Kanan, M. W.; Nocera, D. G. *J. Am. Chem. Soc.* 2010, *132*, 16501–16509.
(13) Kanan, M. W.; Surendranath, Y.; Nocera, D. G. *Chem. Soc. Rev.* 2008, *38*, 109–114.
(14) Esswein, A. J.; McMurdo, M. J.; Ross, P. N.; Bell, A. T.; Tilley, T. D. *J. Phys. Chem. C* 2009, *113*, 15068–15072.
(15) Gersten, S. W.; Samuels, G. J.; Meyer, T. J. *J. Am. Chem. Soc.* 1982, *104*, 4029–4030.
(16) Zong, R.; Thummel, R. P. *J. Am. Chem. Soc.* 2005, *127*, 12802–12803.
(17) Polyansky, D. E.; Muckerman, J. T.; Rochford, J.; Zong, R.; Thummel, R. P.; Fujita, E. *J. Am. Chem. Soc.* 2011, *133*, 14649–14665.
(18) Gilbert, J. A.; Eggleston, D. S.; Murphy, W. R.; Geselowitz, D. A.; Gersten, S. W.; Hodgson, D. J.; Meyer, T. J. *J. Am. Chem. Soc.* 1985, *107*, 3855–3864.
(19) Binstead, R. A.; Chronister, C. W.; Ni, J.; Hartshorn, C. M.; Meyer, T. J. *J. Am. Chem. Soc.* 2000, *122*, 8464–8473.
(20) Geselowitz, D.; Meyer, T. J. *Inorg. Chem.* 1990, *29*, 3894–3896.
(21) Chronister, C. W.; Binstead, R. A.; Ni, J.; Meyer, T. J. *Inorg. Chem.* 1997, *36*, 3814–3815.
(22) Concepcion, J. J.; Jurss, J. W.; Brennaman, M. K.; Hoertz, P. G.; Patrocinio, A. O. T.; Murakami Iha, N. Y.; Templeton, J. L.; Meyer, T. J. *Acc. Chem. Res.* 2009, *42*, 1954–1965.
(23) Liu, F.; Concepcion, J. J.; Jurss, J. W.; Cardolaccia, T.; Templeton, J. L.; Meyer, T. J. *Inorg. Chem.* 2008, *47*, 1727–1752.
(24) Yamada, H.; Hurst, J. K. *J. Am. Chem. Soc.* 2000, *122*, 5303–5311.
(25) Hurst, J. K. *Coord. Chem. Rev.* 2005, *249*, 313–328.
(26) Hurst, J. K.; Zhou, J.; Lei, Y. *Inorg. Chem.* 1992, *31*, 1010–1017.
(27) Lei, Y.; Hurst, J. K. *Inorg. Chem.* 1994, *33*, 4460–4467.
(28) Yamada, H.; Koike, T.; Hurst, J. K. *J. Am. Chem. Soc.* 2001, *123*, 12775–12780.
(29) Hurst, J. K.; Cape, J. L.; Clark, A. E.; Das, S.; Qin, C. *Inorg. Chem.* 2008, *47*, 1753–1764.
(30) Honda, K.; Frank, A. J. *J. Chem. Soc., Chem. Commun.* 1984, 1635–1636.
(31) Collin, J. P.; Sauvage, J. P. *Inorg. Chem.* 1986, *25*, 135–141.
(32) Petach, H. H.; Elliott, C. M. *J. Electrochem. Soc.* 1992, *139*, 2217–2221.

(33) Concepcion, J. J.; Jurss, J. W.; Hoertz, P. G.; Meyer, T. J. *Angew. Chem. Int. Ed.* 2009, *48*, 9473–9476.
(34) Chen, Z.; Concepcion, J. J.; Jurss, J. W.; Meyer, T. J. *J. Am. Chem. Soc.* 2009, *131*, 15580–15581.
(35) Chen, Z.; Concepcion, J. J.; Hull, J. F.; Hoertz, P. G.; Meyer, T. J. *Dalton Trans.* 2010, *39*, 6950.
(36) Song, W.; Chen, Z.; Brennaman, M. K.; Concepcion, J. J.; Patrocinio, A. O. T.; Murakami Iha, N. Y.; Meyer, T. J. *Pure Appl. Chem.* 2011, *83*, 749–768.
(37) Nagoshi, K.; Yamashita, S.; Yagi, M.; Kaneko, M. *J. Mol. Catal. A: Chem.* 1999, *144*, 71–76.
(38) Schoonover, J. R.; Ni, J.; Roecker, L.; White, P. S.; Meyer, T. J. *Inorg. Chem.* 1996, *35*, 5885–5892.
(39) Regalbuto, J. In *Catalyst Preparation*; Regalbuto, J., Ed.; CRC Press, 2006; pp. 297–318.
(40) Sing, K. S. W. *Pure Appl. Chem.* 1985, *57*, 603–619.
(41) Moisii, C.; Deguns, E. W.; Lita, A.; Callahan, S. D.; van de Burgt, L. J.; Magana, D.; Stiegman, A. E. *Chem. Mater.* 2006, *18*, 3965–3975.
(42) Sullivan, B. P.; Salmon, D. J.; Meyer, T. J. *Inorg. Chem.* 1978, *17*, 3334–3341.
(43) Zhao, D.; Huo, Q.; Feng, J.; Chmelka, B. F.; Stucky, G. D. *J. Am. Chem. Soc.* 1998, *120*, 6024–6036.
(44) Brunauer, S.; Emmett, P. H.; Teller, E. *J. Am. Chem. Soc.* 1938, *60*, 309–319.
(45) Barrett, E. P.; Joyner, L. G.; Halenda, P. P. *J. Am. Chem. Soc.* 1951, *73*, 373–380.
(46) Ruddy, D. A.; Jarupatrakorn, J.; Rioux, R. M.; Miller, J. T.; McMurdo, M. J.; McBee, J. L.; Tupper, K. A.; Tilley, T. D. *Chem. Mater.* 2008, *20*, 6517–6527.